Long-range Coordination of Biochemical Signals in Drosophila Embryogenesis and Zebrafish Scale Regeneration

by

Luke Hayden

Department of Cell Biology
Duke University

Date:_____

Approved:

_____
Stefano Di Talia, Supervisor

_____
Daniel J Lew

_____
Joshua E Socolar

_____
Terry Lechler

Dissertation submitted in partial fulfillment of
the requirements for the degree of Doctor
of Philosophy in the Department of
Cell Biology in the Graduate School
of Duke University

2022

ABSTRACT

Long-range Coordination of Biochemical Signals in Drosophila Embryogenesis and Zebrafish Scale Regeneration

by

Luke Hayden

Department of Cell Biology
Duke University

Date:_____

Approved:

_____
Stefano Di Talia, Supervisor

_____
Daniel J Lew

_____
Joshua E Socolar

_____
Terry Lechler

An abstract of a dissertation submitted in partial fulfillment of the requirements for the degree of Doctor of Philosophy in the Department of Cell Biology in the Graduate School of Duke University

2022

Abstract

Coordination of biochemical signals across long distances is a ubiquitous feature of biological systems; however, the molecular and mechanical mechanisms which allow such signaling are still largely unknown. I discuss general classes of long-range signaling mechanisms as well as the regulatory pathways involved in creating and maintaining cellular coordination in different size scales. In particular, I present a thorough mathematical analysis of a reaction-diffusion model of Erk activity waves which control osteoblast regeneration in the zebrafish scale and use live and fixed imaging of *Drosophila melanogaster* embryos to elucidate the mechanisms of synchronized cell cycle control. In the regenerating zebrafish scale, I show that a simple three-component model consisting of Erk, an Erk activator, and an Erk inhibitor is sufficient to generate Erk activity waves which propagate across the millimeter sized region. The properties of these waves agree with chemical wave theory and are structured to enable proper timing of hypertrophy to enable precise regulation of size and shape of the regenerated tissue. In the early *Drosophila* embryo, I show that the ubiquitin ligase Cullin-5 acts to regulate the actin cytoskeleton. Using novel mutants, I show that mutations in the *cullin-5* gene leads to a disruption in signaling across the embryo and an eventual mistiming of the mid-blastula transition. Furthermore, I show that the cell cycle is not controlled globally across the embryo or very locally but rather is coordinated across distances of ~100μm. This work highlights the different

mechanisms and regulation which exists in different contexts to transmit signals across a domain and control the proper development and regeneration of large tissues.

Contents

List of Tables

List of Figures

1. Introduction: Signal propagation in biology

1.1 Biological signaling requirements

Biological systems are extremely varied in their sizes. From the smallest movements of atoms and molecules to the population-wide dynamics across the planet, a fundamental component of life is the ability to transmit information from one location to another. This signal propagation problem is twofold: namely, understanding the vast and diverse mechanisms to propagate such a signal and realizing the consequences once a signal has been conveyed. While the latter continues to be widely studied in contexts such as development, tissue patterning, neurology, the spread of disease and genetic material, and many others, the work I present in this dissertation largely focuses on the former problem of how signals are mechanistically transmitted across time and space. By examining the contexts in which signals must propagate, it becomes clear that a single mechanism is unsatisfactory to explain the diverse phenomena that have been observed. Rather, general mechanistic categories have been described which I seek to highlight here in this introduction.

1.2 Communication over short distances: diffusion

One principal mechanism which underlies all movement of molecules is diffusion. Thermal energy causes particles to move with very high speeds, but the high density of particles leads to frequent collisions and rapidly changing directions. This behavior results means that the time, t, required for a typical signaling molecule like a

protein to travel a given distance, x, using only this "Brownian" motion[1] is proportional to the square of x. A protein of average size requires only ~200ms to travel across the length of an *E. coli* cell (2μm) but would require ~3.5h to travel across a large cell like the *Drosophila melanogaster* embryo (500μm).

Because diffusion is so effective at transmitting signals over very short distances, many small cells are assumed to be well-mixed. That is, the concentrations of these typical proteins are assumed to be homogenous over the longer biological time scales like cell growth and division. Interestingly, the remodeling and activation of cytoskeletal elements including molecular motor activity increases agitation of the cytoplasm and leads to thermal diffusion-like behavior which increases the apparent speed of transport and/or mixing (see Chapter 2 for further discussion of cytoplasmic flows).[2-5]

When coupled to synthesis and degradation, diffusion of an instructional molecule will lead to a concentration gradient where activity and thus signaling strength is reduced as the proteins diffuse. A classic example of this process is the patterning morphogen bicoid in *Drosophila* embryos.[6,7] Transcription of new protein from maternally deposited mRNA coupled with diffusion and degradation generates a stable gradient across the anterior-posterior (AP) axis. The activity of this gradient leads to pattern formation required for the proper development of the larval head and thorax.[7] Multiple overlapping and interacting profiles of diffusing morphogens span the large

embryo which allows proper signaling and coordination of cell fates across a space scale too large for a single diffusive species.

1.2.1 Diffusion constants across varying biological systems

In large cells or tissues, it becomes unclear whether diffusion could act as a mechanism to transmit information in a biologically relevant timescale. Diffusion constants are varied in magnitude and depend on many biophysical properties of the molecule and system. Typical diffusion constants for moderately sized, monomeric proteins are on the order of $10 \mu m^2/s$ in cytoplasm; however, these values can fluctuate over ~3 orders of magnitude.[8] While small, neutral molecules may move quite quickly through the cytoplasm or extracellular space, larger or more reactive proteins may be greatly hindered by other molecules in the system. Moreover, the sheer number of molecules can create a crowding effect which reduce movements. See

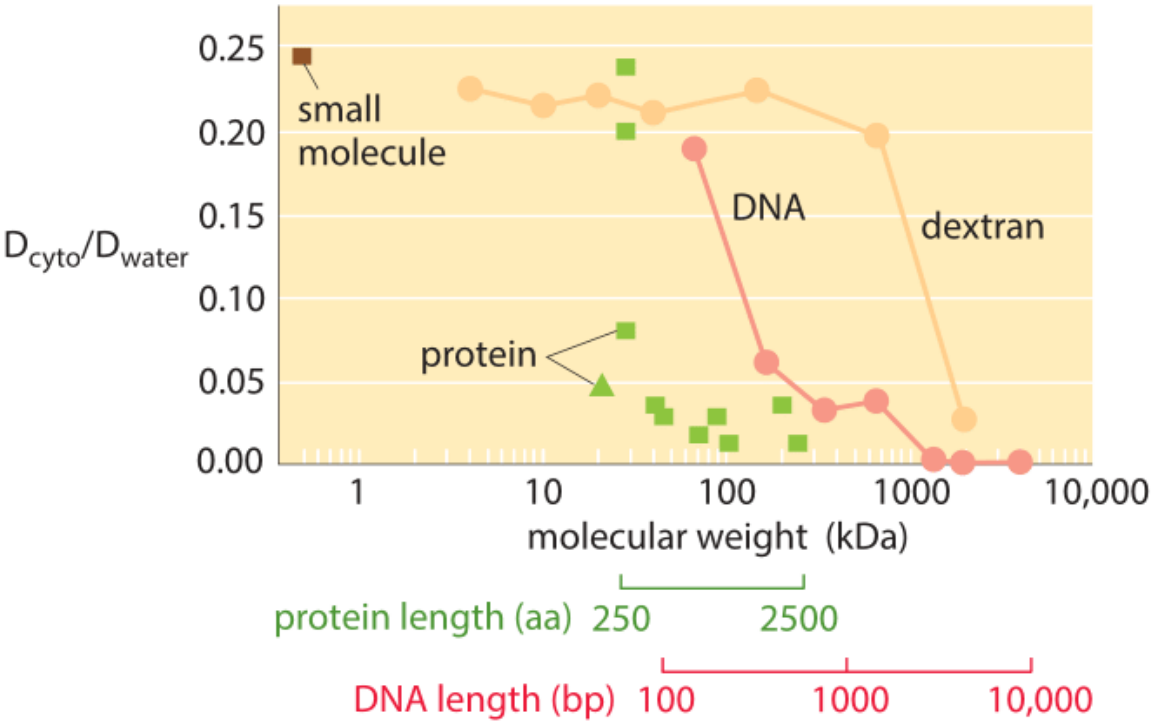

Figure 1: Diffusion constants in cytoplasm. Diffusion constants for various molecules in cytoplasm relative to water. Larger and more reactive species are slowed more in cytoplasm due to collisions and reactions with other intracellular components. Adapted from[9].

One important mechanism which affects how quickly things diffuse in a system is binding interactions. Akin to cars stopping at traffic lights, the speed at which a signaling protein travels across a tissue can be highly regulated through the binding and unbinding to the extracellular matrix. Chapter 2 highlights this effect in the context of diffusive fibroblast growth factors (Fgfs) which control osteoblast hypertrophy during zebrafish scale regeneration.[10,11] Fgf molecules have been shown to bind to heparin sulfate proteoglycans present in the extracellular matrix, leading to an effectively slower

diffusion constant.[12] This slowing has important consequences on the continued activation of growth factor receptors as well as potentially controlling the morphology of the regenerating scale.[10,12]

1.3 Communication over large distances: chemical waves

These previous examples have illustrated two major limitations of diffusive signaling: slow speed and signal dampening. Thus, simple diffusion is incompatible with many observed biological phenomena which require rapid signaling across large distances. One mechanism which overcomes these drawbacks involves the coupling of diffusion with rapid activation in nearby regions to generate traveling chemical waves. These chemical waves are varied in their construction and regulation and will be the focus of the remainder of this work.

Typical waves in biological systems are found in excitable media where small stochastic fluctuations and responses do not yield a response but excitations above a certain threshold leads to a rapid and large change in biochemical activity.[13-15] When multiple of these units are positioned in spatial proximity, signal can diffuse from one unit to the next and trigger a wave to propagate. A classic example is the generation of action potentials in neurons.[16] When sufficient depolarization has occurred, voltage gated ion channels open, leading to a large increase in voltage across the membrane. This increase in voltage causes neighboring channels to open, propagating the change in voltage across the axon. After an action potential has been triggered, the neuron is

refractory to further wave generation for a time until the neuron repolarizes.[17] Chemical waves have been reported in widely different biological contexts from calcium waves following egg fertilization (a single large cell)[18] to aggregation of slime mold (a large collection of cells)[19] to transmission of infectious disease (large populations).[20] Recent advances in imaging techniques and technologies continue to lead to the discovery of an increasing number of systems which communicate through the use of chemical waves.

1.4 Mathematical theory of chemical waves

Biological systems are constantly in a state of flux. Molecules are constantly being produced, reacting, diffusing, and degrading. A set of reaction-diffusion equations describing the spatiotemporal concentrations of various molecules generally capture this dynamic behavior. Historically, the fundamentals of reaction-diffusion mathematics was used to describe how an allele of a particular gene can spread through a population.[21] Later work by Alan Turing showed how systems with interacting activators and inhibitors may give rise to standing waves which generate patterns and enable morphogenesis.[22]

To understand how a system may behave from a theoretical perspective, consider a system with two chemical species, x, and y, where their rates of change are given by $\frac{dx}{dt} = f(x, y)$; $\frac{dy}{dt} = g(x, y)$. While it may be algebraically impossible to obtain explicit solutions for x(t) and y(t), it is possible to explain the dynamics of the system by looking at the nullclines of the system. Nullclines occur when either $f(x, y)$ or $g(x, y)$ are

equal to 0. At the exact moment in time when $\frac{dx}{dt} = f(x, y) = 0$, the concentration of x is unchanging regardless of the concentration of y. An analogous situation arises for y when $\frac{dy}{dt} = g(x, y) = 0$. Nullclines cross at fixed points where $\frac{dx}{dt} = \frac{dy}{dt} = 0$ and the concentration of both species are at equilibrium and are unchanging. By analyzing the rate of change of the concentrations of x and y near these fixed points, we may fully understand the dynamics of the system. When both concentrations get progressively closer to the fixed point, the point is classified as stable, and when at least one concentration moves away from the point, it is classified as unstable. Examples of nullclines with two species is shown in Figure 2.

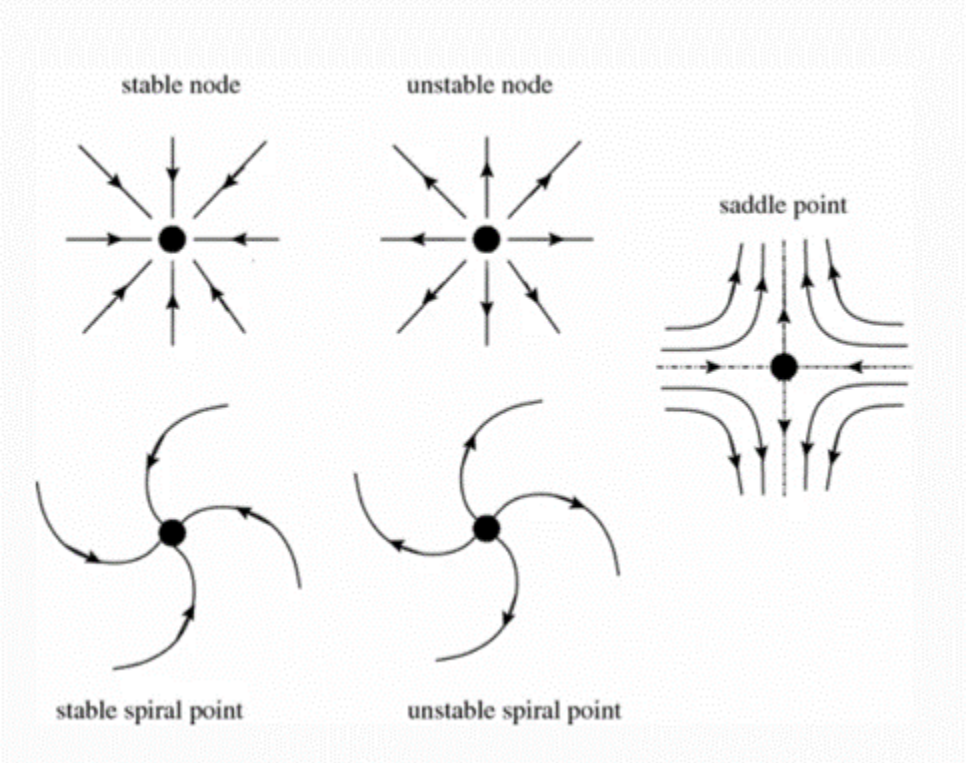

Figure 2: Fixed point stabilities. Trajectories of the concentrations of example species x (vertical) and y (horizontal). Arrows indicate concentration change with time. Adapted from[23].

A system which has multiple fixed points can display behaviors conducive to propagating a signal. For example, an excitable system could exist wherein a stable fixed point lies near an unstable saddle point and the concentrations of both molecules lie at the stable point. A small perturbation in the concentration of one species may be hindered by the instability of the unstable point, causing the concentration of both species to return to the stable point with little change. However, a large perturbation may lead to a state where the system relaxes to the stable point by moving around the

unstable point resulting in an oscillation in concentrations of the two species. When neighboring excitable regions are coupled through diffusion, an oscillation in one region can lead to an oscillation in an adjacent region, propagating across a domain as a wave. Chapter 2 discusses this behavior in the context of recently discovered Erk activity waves which control osteoblast regeneration during zebrafish scale regeneration.[10,11] This work highlights the importance of chemical waves as a mechanism to transmit proliferation signals which could not be transmitted in a reasonable time with diffusion alone.

1.4.1 Erk kinase signaling and regulation

Extracellular signal-regulated kinase (Erk) has emerged as a master regulator of a host of cellular behaviors.[24,25] Importantly it acts to relay signals in the extracellular environment to intracellular behaviors and is therefore an important molecular player in the relay of a growth signal across a cell or tissue. Erk is activated through phosphorylation in response to signaling by a host of growth factors.[26,27] By binding to a receptor, these growth factors stimulate recruitment and activation of intracellular proteins to the cell membrane which eventually lead to the activation of Erk. In zebrafish scales—which is the focus of Chapter 2—Fgfs are good candidates for the regulation of osteoblast hypertrophy.[10,28]

Upon activation, Erk translocates to the nucleus where it triggers a host of responses related to cell proliferation.[29] One of the main targets of Erk is Elk-1 which

induces expression of immediate early genes like c-Fos which is further stabilized by Erk and triggers accumulation of cyclin D1 and a progression from G_1 to S phase.[25,30] Interestingly, Erk has variable and sometimes opposite roles depending on duration and magnitude of activation. Strong activation of Erk leads to cell cycle arrest and possible cell death.[29] Thus it is not simply enough for a biological system to spread a signal, but it must do so with precise strength and temporal dynamics to ensure the correct response.

1.5 Cell cycle control in the early Drosophila embryo

Embryonic development is controlled by the integration of mechanical and biochemical signals which span the embryo in a tightly coordinated series of events. Cytoskeletal rearrangements, especially actomyosin, are critical for such integration and have been the focus of many recent studies.[31-33] The *Drosophila* embryo offers a powerful model system to study how biochemical signals are transmitted across a long distance, how these signals coordinate with the cytoskeleton to regulate proper development through cell cycle control, and how the physical properties of the embryo enable a useful regime in which biochemical and mechanical signals can operate.

Nuclei undergo 13 synchronous rounds of division following fertilization.[34] During the first three cycles, nuclei are located anteriorly, near the center of the embryo. During cycles 4-6, nuclei spread across the AP axis in a process called axial expansion. Recent work on this process has shown that synchronization of the cell cycle across the embryo is achieved through a self-organized mechanism where nuclei regulate their

own positioning.[5] Local degradation of cyclins around the nuclear cloud leads to a reduction in Cdk1 activity and a consequent exit from mitosis.[5,35] The mitotic phosphatase PP1 then activates and spreads outward as a wave which is able to reach the cortex once the nuclear cloud is of sufficient size, around cycle 4. Upon reaching the cortex, PP1 recruits Myosin II through the activity of Rho. Because myosin is only recruited to the cortex locally near the nuclear cloud, myosin accumulates as a gradient which generates cortical contractions which are coupled to flows of the cytoplasm, again centered on the nuclear cloud. These flows spread the nuclei across the AP axis. In mutants with disrupted cytoplasmic flows, asynchronies develop in the cell cycles, eventually causing disruptions at the entrance of the mid-blastula transition.[5]

1.6 The mid-blastula transition

In most organisms, the early developmental program is characterized by unusually fast cell cycles which slow down upon the beginning of morphogenesis. In organisms that have externally developing eggs, like *Drosophila*, *Xenopus*, and zebrafish, this pattern is ubiquitous and has been termed the mid-blastula transition (MBT). In these organisms, the MBT marks a developmental point in time where the new organism shifts from a reliance on maternally deposited factors to an increase in transcription and translation. This transition has been widely studied, but a comprehensive mechanism for its timing and regulation remains elusive.

One of the fundamental regulators of the timing of the MBT is ratio of the number of nuclei to cytoplasmic content (N/C ratio). Early studies in *Xenopus* showed this fact by physically altering the number of nuclei in the embryo and measuring the delay in MBT events.[36,37] Similarly, experiments in *Drosophila* showed that haploid *Drosophila* embryos undergo an additional division before pausing their cell cycles.[38] Later studies identified a threshold nuclear density around 70% of the wildtype values at the MBT required to arrest the cell cycle in *Drosophila*. Embryos with modified DNA content less than that threshold performed an extra division, while embryos above the threshold did not. Interestingly, near the threshold density, embryos showed patchy behavior where only part of the embryo underwent a division.[39,40] This phenomenon is revisited in Chapter 3.

While haploid embryos performed an extra division, thereby delaying some MBT events, cellularization and upregulation of zygotic transcription began at the normal time.[38] When embryos were arrested two cell cycles early by reducing the activity of mitotic cyclins, cellularization again occurred at the normal time.[41] These results indicate that the N/C ratio may play a passive role in regulating MBT timing by altering Cdk1 activity. In accordance with this theory, one of the prevailing models of MBT timing is titration of an MBT inhibitor against DNA content. Thus, MBT events are repressed by the inhibitor until DNA content rises to a sufficient level. Histones are an emerging candidate for this MBT inhibitor as altering H3 and H4 histone proteins

modulated the DNA threshold required for cell cycle arrest as well as the onset of transcription and cell cycle lengthening.[42]

Chapter 3 will build upon previous work[5,43] to describe the regulation of the signaling required for synchronized mitotic activity in the early Drosophila embryo. This activity is required for uniform entry into the MBT, ensuring organism survival. Recent advances have enabled the high spatiotemporal resolution of molecular dynamics which has continued to illustrate the importance of chemical waves as a crucial mechanism to propagate signals across large distances in biological systems. Chapter 4 serves as a discussion where I present future directions for further elucidating the mechanism of Erk activity waves in zebrafish scale regeneration and the regulation of mitotic waves and cell cycle control in the *Drosophila* embryo.

2. Mathematical modeling of Erk activity waves in regenerating zebrafish scales

This chapter was modified from the manuscript: Luke D. Hayden, Kenneth D. Poss, Alessandro De Simone, Stefano Di Talia, Mathematical modeling of Erk activity waves in regenerating zebrafish scales, Biophysical Journal 120, 4287-4297 (2021). doi: 10.1016/j.bpj.2021.05.004.[11] The contributions of co-authors to the manuscript are detailed in Section 2.5 Author contributions.

2.1 Summary

Erk signaling regulates cellular decisions in many biological contexts. Recently, we have reported a series of Erk activity traveling waves that coordinate regeneration of osteoblast tissue in zebrafish scales. These waves originate from a central source region, propagate as expanding rings, and impart cell growth, thus controlling tissue morphogenesis. Here, we present a minimal reaction-diffusion model for Erk activity waves. The model considers three components: Erk, a diffusible Erk activator, and an Erk inhibitor. Erk stimulates both its activator and inhibitor, forming a positive and negative feedback loop, respectively. Our model shows that this system can be excitable and propagate Erk activity waves. Waves originate from a pulsatile source that is modeled by adding a localized basal production of the activator, which turns the source region from an excitable to an oscillatory state. As Erk activity periodically rises in the source, it can trigger an excitable wave that travels across the entire tissue. Analysis of the model finds that positive feedback controls the properties of the traveling wavefront

and that negative feedback controls the duration of Erk activity peak and the period of Erk activity waves. The geometrical properties of the waves facilitate constraints on the effective diffusivity of the activator, indicating that waves are an efficient mechanism to transfer growth factor signaling rapidly across a large tissue.

2.2 Significance

Signaling waves are a possible mechanism of spatiotemporal organization of multicellular tissues. We have recently shown that waves of activity of the kinase Erk control osteoblast regeneration in adult zebrafish scales. Here, we present a detailed characterization of a mathematical model of these signaling waves. We show that a source region poised in an oscillatory state can broadcast traveling waves of Erk activity in the surrounding excitable tissue. The dynamics of the source control the number and frequency of waves. Geometrical arguments support the notion that excitable Erk waves are an effective mechanism to transport growth factor signaling across a large regenerating tissue.

2.3 Introduction

The proper function of multicellular systems requires tight coordination of their cellular components. Coordination across tissues is often provided by nonuniformly distributed signaling molecules.[44-46] In the classic "morphogen gradient" model, a certain information-carrying molecule, the morphogen, is distributed in a graded manner across the tissue, and cell behaviors are instructed differentially by morphogen local

concentration or its dynamics.[45,47,48] These morphogens can be transcription factors, as in the case of Bicoid in Drosophila embryos, or extracellular ligands that bind to a transmembrane receptor and activate signaling cascades. In a simple model of gradient formation, morphogen molecules are produced in a localized source, diffuse in the extracellular space, and are absorbed or processed ("degraded") by cells on a characteristic timescale. Under these conditions, a gradient would form, characterized by an exponential decay profile with a length scale equal to the square root of diffusivity divided by degradation rate. Although morphogen gradients can form quickly in small tissues, it might be difficult to establish such diffusion gradients spanning large tissues, as the time needed to distribute molecules by diffusion scales with the square of the distance. Moreover, the time needed for morphogen concentration to approach its equilibrium value can vary significantly across the gradient[49], suggesting that for large tissue, a static morphogen gradient might be difficult to generate and/or maintain. As a consequence, although several examples of morphogen gradients have been described in embryonic tissues of size of 10–100 μm, the role or mechanism of establishment of these gradients in larger tissues of order of a millimeter or longer remains poorly understood.[50] Active transport, for example, through specialized cytonemes[51,52], can provide faster morphogen spreading. Alternatively, coupling diffusion with positive feedback can transport information across large spatial scales by generating waves.[15,53-55] Waves can propagate quickly across a tissue and maintain their intensity, providing

efficient information transport.[56,57] Thus, waves are an alternative mechanism to morphogen gradients for the regulation of cellular dynamics in large tissues.

Signaling waves might be particularly important in the control of adult tissue regeneration, i.e., the process through which tissues regain their functional form after injury. Tissue regeneration requires precise control of cellular dynamics across a wide range of temporal and spatial scales.[58] Many pathways that are important during development are reactivated in regeneration[59], but it is unclear how these signals are coordinated across the large spatial dimensions of adult regenerating tissues. Extracellular signal-regulated kinase (Erk) is a signaling component that has been implicated in many developmental contexts, including regeneration.[60-62] Several feedback systems confer on Erk activity a variety of dynamic behaviors, which can lead to different outcomes in a context-dependent manner.[24,63] Understanding how these feedback mechanisms are explored in different biological processes is likely to reveal important regulatory principles. In particular, it has been shown that Erk oscillations can be transmitted to nearby cells and propagate as waves, thereby coordinating cellular dynamics across multiple cells.[64-68] For example, in response to a wound in the mouse skin, epithelial cells collectively migrate toward the wound.[66,69] This process is recapitulated in wound assays of MDCK cell cultures, in which it has been extensively studied. Cells most proximal to the wound first move toward the injury site, inducing stretching forces on the neighboring cells.[65,70-72] This mechanical deformation likely

triggers activation of a disintegrin and metalloprotease 17 (ADAM17), which in turn drives the release of membrane-tethered epidermal growth factor (EGF), signaling to neighboring cells through the EGF receptor (EGFR).[65] ERK activation through the EGFR signaling cascade induces cell contraction in follower cells. Contraction in these cells exerts stretching forces on the next follower cells, prompting another round of ERK activation. This positive feedback loop between mechanical forces and ERK activation.[65] can result in traveling waves. It has been proposed that the coupling of forces and ERK activity facilitates long-range order and migration in the direction of the wound[73], whereas mechanical forces alone would tend to lose directionality and strength while spreading across a tissue.[74,75]

Recently, we have reported Erk activity waves in vivo in regenerating osteoblast tissue in zebrafish scales.[10] These waves have properties of reaction-diffusion waves in an excitable medium. Here, we present a detailed characterization of a mathematical model of Erk activity propagation in zebrafish scales. Our model shows that coupling a localized oscillatory source region with a surrounding excitable tissue can generate periodic excitable waves. Thus, our model suggests that tuning the dynamic properties of the source region is a simple strategy to control wave generation and, ultimately, tissue growth.

2.4 Materials and methods

2.4.1 Experimental data

Experimental data were published previously.[10] Experimental data collection and analysis were described as previously.[10]

2.4.2 Numerical solutions of the model

The numerical solution of the presented mathematical model and analysis were performed with custom MATLAB (The MathWorks, Natick, MA) 2019b software. The system of partial differential equations was simulated using the finite differences method.[76] In the standard simulation, the simulation domain is a 1090 μm × 1090 μm square. Absorbing boundary conditions are set at the domain edge. A circle with a radius of 520 μm, centered in the simulation domain, is the scale region. Erk activity and the inhibitor concentration are set to 0 outside the scale region. Because a gap of at least 25 μm exists between the edge of the scale region and the domain edge and the activator degradation length is 7 μm, boundary conditions do not majorly affect system dynamics in the scale region. In the standard simulation, the activator source region is a small off-center circle with a radius of 40 μm. The standard time step is 0.01 h, and the spatial coordinates were discretized using a square lattice with grid size of 5 μm. The initial condition is that all chemical species are set to 0. Parameters (Table 1) were chosen to generate waves with properties (peak speed, frequency, Erk activation and inactivation time) that are compatible with experimental observations. For parameter sensitivity

analysis (Figure 5, Figure 8) and to reduce confounding effects because of wave curvature, we used a domain geometry that generates planar waves. Thus, in this case the simulations domain is a 10 μm × 1000 μm rectangle with a 10 μm × 50 μm rectangular source region at one end. Reflecting boundary conditions are used for the activator diffusion at the domain edges. Velocity was calculated by measuring the time required for the planar wave to travel 20 μm, starting from when a wave was 130 μm away from the source region. The analysis was limited to parameters that generate dynamics compatible to those observed in vivo (i.e., each source oscillation generates a traveling wave reaching the edge of the tissue). A source oscillation event was scored when active Erk in the source reached transiently a prominence above 0.2 (the "prominence" is the Erk active fraction at any given time minus the baseline Erk active fraction). A wave reaching the edge event was scored 500 μm from the source when active Erk reached transiently a prominence above 0.2. Wave period was calculated by the duration between successive peaks in the excited region, 150 μm away from the source region. Wave width was calculated as full width half-maximum when the wave peak was ~900 μm from the source region. Wave period, velocity, and width were calculated exclusively for parameter sets that led to the formation of a stable wave at every oscillation of the source region as it is seen experimentally.

Table 1. Parameters of the standard simulation of Erk activity waves. Note that to fully nondimensionalize the equations of the mathematical model, we would need to specify the concentration of total Erk [E_T]. We lack experimental data on this parameter; however, experiments in different cell types argue for values in the range of [E_T] ~0.1–1 μM.[77] Notice that these parameters are slightly different from those of[10], as we found that by rescaling all time-dependent parameters, we could tune α_2 to obtain any wave frequency seen experimentally.

Parameter	Value	Description
α_1	12.6 h^{-1}	maximal Erk activation rate
β	0.35	Erk activation AC_{50}
γ_1	15.4 h^{-1}	Erk inhibitor-dependent inactivation rate
γ_e	0.14 h^{-1}	Erk autonomous inactivation rate
α_2	0.112 h^{-1} (at the source); 0 (outside the source)	activator deposition rate
α_3	3.9 h^{-1}	Erk-dependent activator production rate
γ_2	11.8 h^{-1}	activator degradation rate
D	566 μm^2 h^{-1}	activator diffusion constant
γ_3	0.14 h^{-1}	inhibitor timescale separation
α_4	0.5	inhibitor Erk-dependent

The oscillatory deposition model was similar to the standard simulation, but the activator deposition at the source $\alpha 2$ varied over time as a periodic Gaussian pulse:

$$\alpha_2(t) = \frac{a}{s(2\pi)^{1/2}}\ exp\left(-\frac{(t\ mod\ T\ -\ \varphi)^2}{2s^2}\right)$$

with amplitude a, standard deviation s, oscillation period T, and oscillation phase φ. mod indicates the modulus function, that is, the remainder of the division of t by T. The oscillation period is set to 24.3 h to match the period of source oscillation in the constant deposition model. The oscillation phase is chosen as half the period. The standard

deviation of the temporal oscillation was chosen to be 1 h to approximately match the activation and inactivation time of the wave. The Gaussian peak amplitude was 2.8, calculated so that the total amount of activator deposited by the source over one oscillation period is approximately equal in the two models. To simulate treatment with an Erk inhibitor (Figure 6D), $\alpha 1$ was set to 0 for 10 h and then set back to its standard value. The time elapsed until the formation of the next wave was calculated as the time from the end of the treatment to that of the formation of a local maximum of Erk activity in the source region. In the model including inhibitor diffusion (Fig. 3 F), inhibitor diffusion was treated in the same way as activator diffusion. To determine whether stationary waves formed, simulations were performed for at least 200 h of simulated time.

To calculate the velocity of Erk activity waves as a function of radial distance (Figure 7A) and to minimize the effect of the source on wave propagation, a 6 μm radius source region was used. To measure the minimal radius of the source excited region that can generate traveling waves (Figure 7D), the source activator production $\alpha 2$ was set to 0, and a certain concentration of activator was deposited in a circle of 10 μm radius at the onset of the simulation; each simulation was performed for 50 h of simulation time. At each time step, the excited region was calculated by testing for each grid point (grid size, 1 μm) if it reached the region of the phase space in which an excitation occurs (in a

simulation with null diffusion). The total excited region is the set of points that reached the excitation region at a certain moment during the simulation.

In the model of activator simple diffusion (Figure 7G), all model parameters were set to 0, except α_2 and D.

In Figure 8B, the experimental wave frequency was measured by smoothening the number of waves as a function of time and calculating its numerical derivative. Values of $\alpha 2$ and $\gamma 3$ relative to the value in the standard simulation were inferred using the predictions of Figure 5. The simulation code is available at https://github.com/lhaydene26/Hayden_modelingErkWaves2021.

2.3 Results

2.3.1 A three-component excitable system generates Erk activity waves

Zebrafish scales are millimeter-sized bone disks that form a protective skeletal array on the body of the fish.[78] The scale bone is covered by a monolayer of osteoblasts that secrete bone matrix. After scale loss, a new osteoblast pool regenerates and reforms the bone. The osteoblast tissue forms first by differentiation of an unknown progenitor, then osteoblasts proliferate and finally increase in size without cell division (cell hypertrophy).[10,79,80] This latter hypertrophic phase is coordinated by repeated waves of Erk activity, which can be visualized using a transgenic biosensor expressed specifically in osteoblasts (Figure 3A).[10] Using image analysis methods, we were able to map Erk activity in the entire osteoblast population of regenerating scales—see Figure 3A.[10] This

approach revealed repeated Erk activity waves that originate from a central source region and propagate outward as expanding rings (Figure 3A).[10] These waves move at a speed on the order of 10 μm/h and cross the entire scale in a few days; Erk is activated in 3 h and deactivated in 5 h, thus generating a peak 50–100 μm wide.[10] The dynamic properties of the central source region suggest that it could be a dynamic system operating in an oscillatory regime, whereas the rest of the scale would be excitable. An excitable system is a nonlinear system that displays small responses to small stimuli but undergoes a large excursion in the phase space in response to perturbations above a certain threshold.[13,14] Multiple excitable units can be coupled by diffusion and generate waves. Compatible with this idea, we found that wave initiation and propagation depend on fibroblast growth factor receptor (Fgfr) signaling, which is activated by extracellular diffusible ligands of the fibroblast growth factor family (Fgfs).[10] Thus, Fgfs are candidates for propagating Erk activity from one cell to the next. To form an excitable system that can sustain a wave, Erk active cells need to produce or stimulate Fgfs, thus generating a positive feedback loop. In addition, cells at high Erk activity switch off after a certain time, indicating that one or multiple Erk inhibitors are activated in Erk active cells, generating a negative feedback loop. Thus, the minimal components of the proposed model are Erk itself, an Erk activator, and an Erk inhibitor. In our model, the activator can diffuse in the extracellular space, whereas the Erk kinase and its inhibitor are confined within each cell. We use a coarse-grained continuum approach

and describe the extracellular movement of the Erk activator by simple diffusion (Figure 3B). These assumptions lead to the following model for Erk activity:

$$\frac{\partial [E]}{\partial t} = \frac{\alpha_1 [A]^2}{\beta^2 + [A]^2}(E_T - [E]) - [E](\gamma_1 [I] + \gamma_e)$$

$$\frac{\partial [A]}{\partial t} = \alpha_2 + \alpha_3 [E] - \gamma_2 [A] + D\nabla^2 [A]$$

$$\frac{\partial [I]}{\partial t} = \gamma_3 (\alpha_4 [E] - [I])$$

where $[E]$, $[A]$, and $[I]$ represent the concentrations of active Erk, diffusible activator, and inhibitor, respectively. For simplicity, reaction terms are described according to the law of mass action with the exception of the rate of Erk activation by the activator, expressed as a Hill function of the activator concentration (a non-linearity in the positive feedback regulation between the activator and Erk is needed for the system to be excitable). In the model, α_1 is the Erk activation rate at saturating activator, β is the AC_{50} of Erk activation by the activator, E_T is the mass-conserved sum of active and inactive Erk, γ_1 is the Erk inactivation rate by the inhibitor I, γ_e is the Erk autonomous de-activation rate, α_2 is the activator production rate, α_3 is the Erk-dependent activator production rate, γ_2 is the autonomous activator decay rate, D is the diffusion constant of the activator, $\gamma_3 \alpha_4$ is the inhibitor production rate and γ_3 is the inhibitor autonomous degradation rate. By nondimensionalizing the concentrations [E], [A], and [I] by dividing by the total amount of Erk E_T, we obtain the equations (brackets are omitted):

$$\frac{\partial E}{\partial t} = \frac{\alpha_1 A^2}{\tilde{\beta}^2 + A^2}(1 - E) - E(\tilde{\gamma}_1 I + \gamma_e)$$

$$\frac{\partial A}{\partial t} = \widetilde{\alpha_2} + \alpha_3 E - \gamma_2 A + D\nabla^2 A$$

$$\frac{\partial I}{\partial t} = \gamma_3(\alpha_4 E - I)$$

where $\tilde{\beta} = \beta/E_T$, $\widetilde{\gamma_1} = \gamma_1 E_T$, and $\widetilde{\alpha_2} = \alpha_2/E_T$ For sake of simplicity, we omit the tilde signs from $\tilde{\beta}$, $\widetilde{\gamma_1}$, and $\widetilde{\alpha_2}$ hereafter. To tune the system to an oscillatory state in the source region (Figure 3C), instead of an excitable state, we introduced in that region a constant term of production of the activator α_2. This term can be interpreted as a basal activator production by osteoblasts in the source region or a contribution from an external cellular pool. This term is null in the excitable region. Numerical solutions of the previous equations demonstrate that the system can generate traveling waves of Erk activity (Figure 3D). As expected, linear stability analysis shows that with the chosen set of parameters, the source region oscillates (limit cycle, Figure 3E), whereas outside the source region, the system is excitable (Figure 3F). Thus, oscillations of activator levels (and Erk activity) in the source trigger the propagation of excitable waves. The features of the excitable wave can be understood through the following arguments.[54] The leading edge of the wave (inhibitor levels low) can be approximated with a bistable system, with stable fixed points at high and low Erk activity (Figure 3G). Activator diffusion triggers excitations in the tissue in front of the leading edge. In that region, the system will leave the basin of attraction of the low Erk activity state and move toward the high Erk activity state. At the same time, the accumulating active Erk triggers the production of its own inhibitor. As the inhibitor accumulates, the level of active Erk decreases until the

system resets to a state of low Erk activity. The system cannot be excited again until the inhibitor has substantially degraded (refractory period). Thus, our analysis points to a simple dynamical picture for Erk waves in scale regeneration.

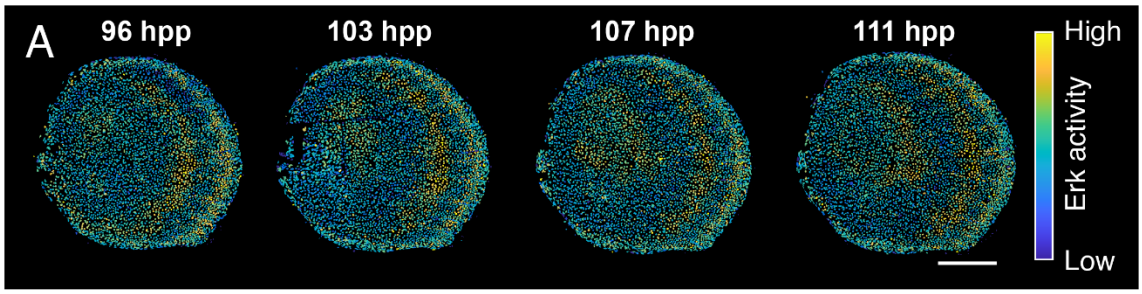
A
96 hpp
103 hpp
107 hpp
111 hpp
High
Erk activity
Low

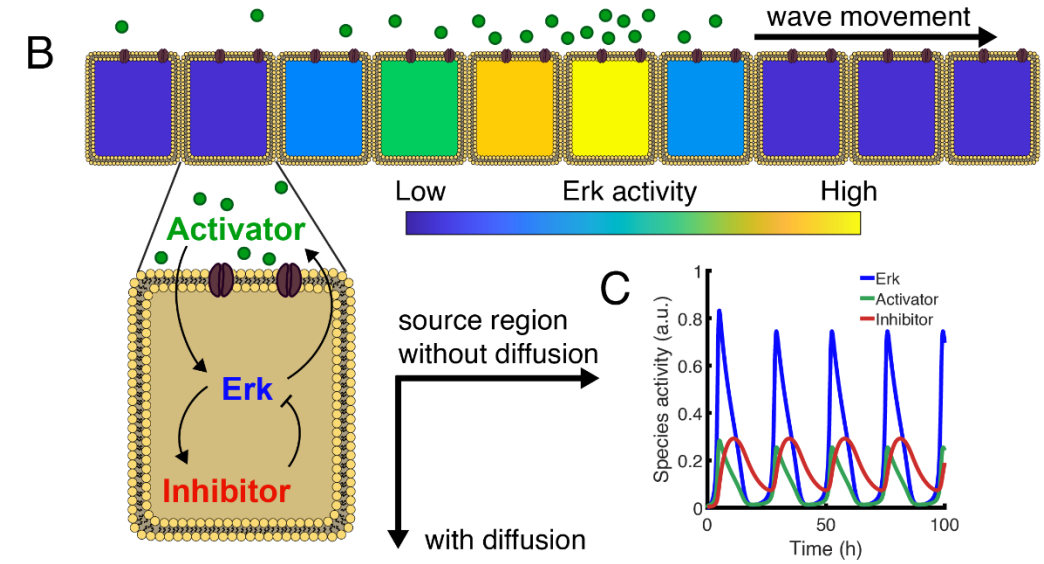
B
wave movement
Low
Erk activity
High
Activator
Erk
Inhibitor
source region
without diffusion
with diffusion
C
Erk
Activator
Inhibitor
Species activity (a.u.)
Time (h)

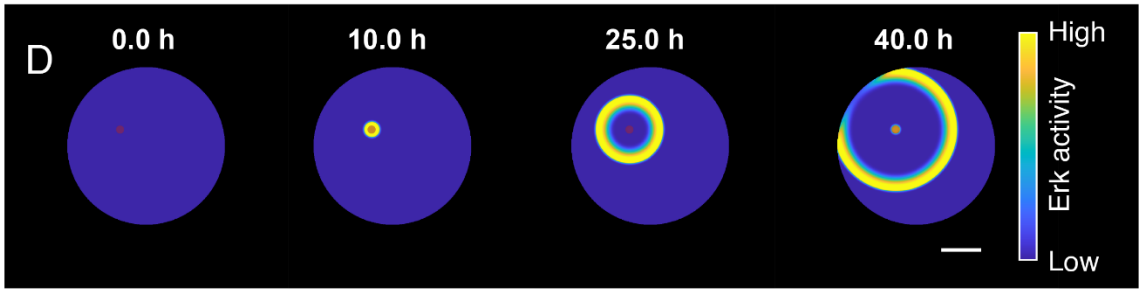
D
0.0 h
10.0 h
25.0 h
40.0 h
High
Erk activity
Low

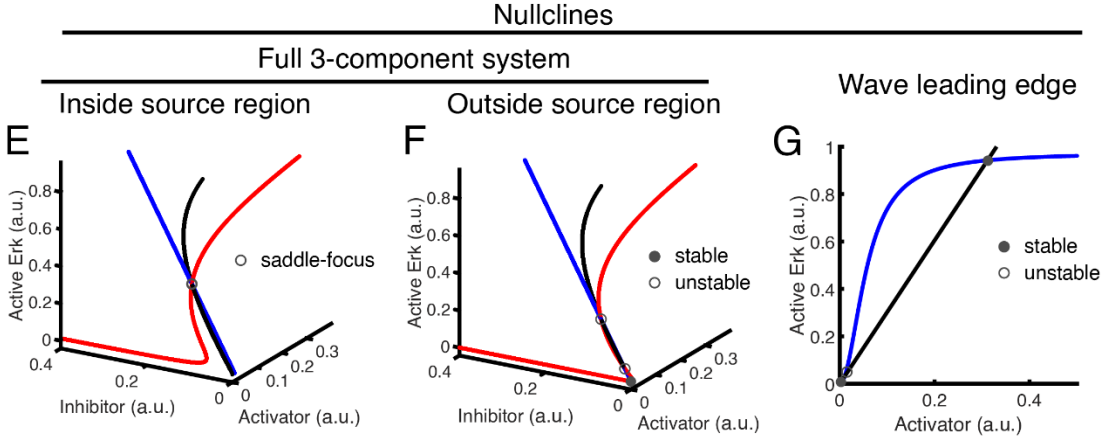
Nullclines
Full 3-component system
Inside source region
Outside source region
Wave leading edge
E
F
G
saddle-focus
stable
unstable
Active Erk (a.u.)
Inhibitor (a.u.)
Activator (a.u.)

Figure 3: Model formulation and stability analysis. (A) Erk activity in regenerating scales in vivo, measured using an Erk kinase translocation reporter (Erk KTR). The Erk KTR sensor provides a proxy of Erk activity through measurement of its subcellular localization. The sensor contains both a nuclear localization signal and a nuclear export signal and preferentially localizes to the nucleus when unphosphorylated and to the cytoplasm when phosphorylated.[81] Thus, a readout of Erk activity at cellular resolution is calculated by measuring the ratio of nuclear and cytoplasmic Erk KTR signals. The data shown were imaged and analyzed previously.[10] hpp, hours post plucking. (B) Schematics of theoretical model including a diffusible extracellular activator, Erk, and an inhibitor of Erk. Arrows between chemical species indicate feedback. (C) Numerical simulation of the dynamical system in the source region when diffusion is null. (D) Numerical simulation of the reaction-diffusion dynamical system. (E and F) Stability analysis of the system when diffusion is null. E: source region; F: outside the source region. Curves indicate pairwise intersections between nullcline surfaces. (G) Leading edge fixed-point analysis: nullclines in the leading edge of the wave, where the inhibitor is taken to be 0. Circles: fixed points at 4 h from simulation start (stability is indicated). Scale bars, 250 μm. a.u., arbitrary unit.

To understand which parameters control wave properties, namely wave frequency and speed, we performed a parameter sensitivity analysis by varying a single parameter at a time. The phenomenology of source oscillation and wave propagation can change while varying parameters. For example, for some parameter variations, damped waves originate from the source, or the source or excitable region is locked in a high or low Erk activity state (Figure 4).

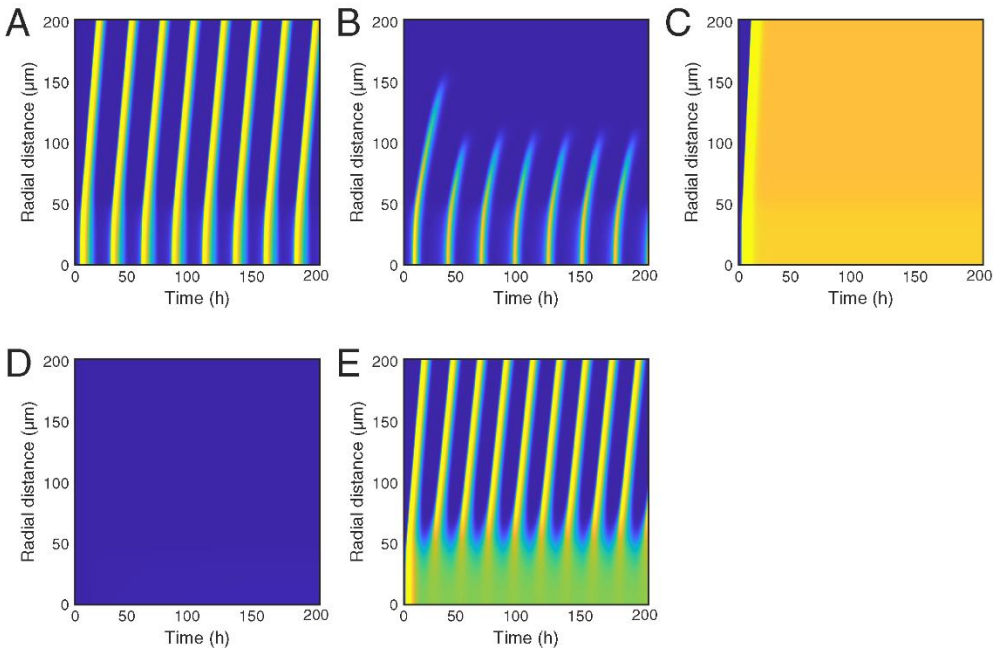

Figure 4: Examples of Erk activity dynamics in different regions of the parameter space. (A) Standard simulation. Periodic waves travel across the domain. (B) Damped waves, $\boldsymbol{\alpha_1 = 0.63\alpha_1(standard)}$. A fraction of waves does not reach the scale edge. (C) Bistable wave, $\boldsymbol{\alpha_1 = 1.77\alpha_1(standard)}$. A front of high Erk activity propagates across the simulation domain. (D) Waves are not generated, $\boldsymbol{\alpha_2 = 0.15\alpha_2(standard)}$. (E) The source is locked in a high Erk activity state and travelling waves are periodically generated, $\boldsymbol{\alpha_2 = 3\alpha_2(standard)}$.

However, in our in vivo observations, each oscillation of the source corresponded to the generation of a wave reaching the edge of the tissue. Therefore, we limited our analysis to parameter values that generate a phenomenology that corresponds to these observations (see 2.4 Materials and methods for details). We found that waves with a well-defined speed and frequency are generated in a wide region of the parameter space, with some parameters having broader ranges than others. As the parameters are varied outside this range, stable waves are replaced either by unstable

pulses that lose amplitude over time or by a stable propagating front of high Erk activity, indicating the establishment of a bistable system (Figure 5).

The theory of chemical waves predicts that the speed of the wave is determined by the activator diffusion constant D and by the timescale of activation τ via v ∼(D/τ)1/2.[15,53,54] As predicted, the speed of Erk activity waves scales as the square root of the diffusion constant (Figure 5A). Furthermore, our analysis demonstrates that parameters controlling the activator-Erk positive feedback loop have a larger impact on wave speed than its frequency (Figure 5B–F). This can be intuitively understood by the fact that the positive feedback loop between Erk and its activator dominates in the leading edge, i.e., where the inhibitor concentration is low. However, parameters controlling inhibitor dynamics mainly impact wave frequency as they control the duration of the refractory period and thus the intrinsic minimal lag time between subsequent excitation events. An interesting exception is the rate of deposition of the activator at the source (α_2), which controls the period of oscillation of the source. When the period imparted by α_2 is longer than the intrinsic oscillation period of the excitable region (Figure 5G and H), this period imparted by $\alpha 2$ will determine the tempo of wave generation (Figure 5I). However, when the oscillation period at the source is shorter than the intrinsic oscillation period of the excitable system, this latter intrinsic oscillation period will limit the rate of wave generation.

Sensitivity analysis also indicates that several parameters have a similar impact on wave speed and frequency, and this codependency is strengthened by changing two parameters simultaneously (Figure 5J–L). For some of these parameters, this codependency is intuitive. For example, the speed of the Erk wave is controlled by the dynamics of the leading edge at concentration A ≪ β; therefore, the term controlling Erk activation by the activator effectively reduces to α_1/β^2, which indeed captures the codependency between the two parameters (Figure 5J). This analysis suggests that although our model has several parameters that are not known experimentally, the emergent properties of the system belong to a few general scenarios. Furthermore, parameter values are constrained by the dynamic features of Erk oscillations and waves.

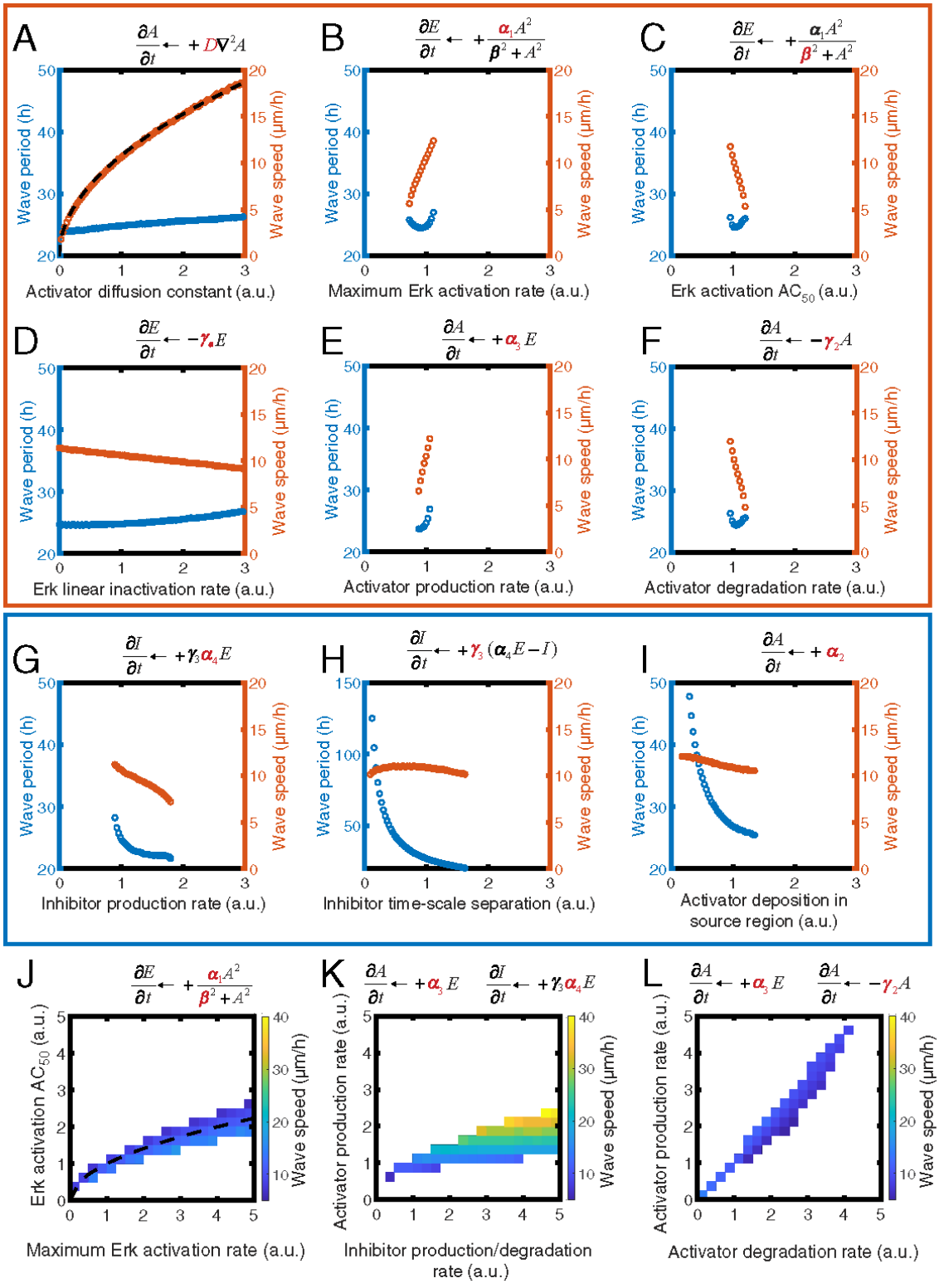
A
$\frac{\partial A}{\partial t} \leftarrow + D\nabla^2 A$
Wave period (h)
Wave speed (μm/h)
Activator diffusion constant (a.u.)
B
$\frac{\partial E}{\partial t} \leftarrow + \frac{\alpha_1 A^2}{\beta^2 + A^2}$
Maximum Erk activation rate (a.u.)
C
$\frac{\partial E}{\partial t} \leftarrow + \frac{\alpha_1 A^2}{\beta^2 + A^2}$
Erk activation AC_{50} (a.u.)
D
$\frac{\partial E}{\partial t} \leftarrow - \gamma_* E$
Erk linear inactivation rate (a.u.)
E
$\frac{\partial A}{\partial t} \leftarrow + \alpha_3 E$
Activator production rate (a.u.)
F
$\frac{\partial A}{\partial t} \leftarrow - \gamma_2 A$
Activator degradation rate (a.u.)
G
$\frac{\partial I}{\partial t} \leftarrow + \gamma_3 \alpha_4 E$
Inhibitor production rate (a.u.)
H
$\frac{\partial I}{\partial t} \leftarrow + \gamma_3 (\alpha_4 E - I)$
Inhibitor time-scale separation (a.u.)
I
$\frac{\partial A}{\partial t} \leftarrow + \alpha_2$
Activator deposition in source region (a.u.)
J
$\frac{\partial E}{\partial t} \leftarrow + \frac{\alpha_1 A^2}{\beta^2 + A^2}$
Erk activation AC_{50} (a.u.)
Wave speed (μm/h)
Maximum Erk activation rate (a.u.)
K
$\frac{\partial A}{\partial t} \leftarrow + \alpha_3 E$
$\frac{\partial I}{\partial t} \leftarrow + \gamma_3 \alpha_4 E$
Activator production rate (a.u.)
Inhibitor production/degradation rate (a.u.)
L
$\frac{\partial A}{\partial t} \leftarrow + \alpha_3 E$
$\frac{\partial A}{\partial t} \leftarrow - \gamma_2 A$
Activator production rate (a.u.)
Activator degradation rate (a.u.)

Figure 5: Parameter analysis and sensitivity. Wave speed and period varying the parameters of the model: D (A), $\boldsymbol{\alpha_1}$ (B), $\boldsymbol{\beta}$ (C), $\boldsymbol{\gamma_e}$ (D), $\boldsymbol{\alpha_3}$ (E), $\boldsymbol{\gamma_2}$ (F), $\boldsymbol{\alpha_4}$ (G), $\boldsymbol{\gamma_3}$ (H), and $\boldsymbol{\alpha_2}$ (I) individually and covarying $\boldsymbol{\alpha_1}/\boldsymbol{\beta}$ (J), $\boldsymbol{\alpha_3}/\boldsymbol{\alpha_4}$ (K), and $\boldsymbol{\alpha_3}/\boldsymbol{\gamma_2}$ (L). Parameters are expressed relative to the reference value in our standard simulation (see Table **1**). Predicted square root dependencies in (A, J) are plotted as dashed black curves: (A) $\boldsymbol{v = v_0 D^{1/2}}$ where $\boldsymbol{v_0 = 10.75}$ μm/h is velocity for the standard set of parameters and D is expressed in relative units and (J) square root dependency: $\boldsymbol{\beta = {\alpha_1}^{1/2}}$. Wave speed and period are calculated for regions of parameter space which feature periodic stable waves. Orange box: parameters that affect mainly wave speed. Blue box: parameters that affect mainly wave period. Please note that $\boldsymbol{\gamma_1}$ and $\boldsymbol{\alpha_4}$ together determine the action of the inhibitor by controlling its activity towards Erk and its levels, respectively. Thus, the dependencies of the wave period and speed on those parameters are identical, and the plot for $\boldsymbol{\gamma_1}$ was omitted.

2.3.2 The dynamic properties of the source region can impact how wave generation responds to perturbations

In the proposed model, the Erk activator is deposited in the source region, forcing it to an oscillatory regime (Figure 6A). In an alternative model, external activator deposition may be intrinsically oscillatory (Figure 6B). In principle, these two different scenarios could be distinguished experimentally by pharmacological inhibition of Erk. In this experiment, Erk activity would be temporarily impaired using a pharmacological inhibitor; then this pharmacological inhibitor would be washed away, and the recovery of the system would be monitored. When the inhibitor is washed out, there would be a delay before the system recovers and another wave is generated (Figure 6C). The constant deposition model predicts a constant delay in wave onset determined by the time needed for the activator to build up in the source region and trigger the positive feedback loop. By contrast, the oscillatory deposition model predicts a variable delay

that depends on the phase of the deposition oscillation at the time of pharmacological inhibitor washout (Figure 6D). Thus, experiments that analyze how new waves arise after perturbations of Erk activity could provide insights on the dynamic properties of the source. However, we note that this analysis may be complicated by potential additional feedback mechanisms between the rate of production of the activator and its downstream activity.

2.3.3 Analysis of the effects of diffusion argue for waves as an effective mechanism to transfer information

The diffusivity of ligands in vivo is context dependent because of the complex microscopic details of ligand movement, and a wide range of different values have been observed for ligands of the Fgf family.[50] Our experimental data on the speed of Erk waves (v = 10 μm/h) and the typical timescale of Erk activation (τ = 3 h) allow us to estimate the effective diffusion constant of the signal propagating Erk waves as $D \sim v^2\tau \sim 0.1\ \mu m^2/s$.[10] To further strengthen the evidence toward a small diffusion constant, we consider the possibility that an alternative model could generate the slow waves seen experimentally but for larger values of the diffusion constant of the activator. In particular, we tested whether a faster activator diffusion would be compatible with our experimental observations in a model in which the Erk inhibitor could also diffuse extracellularly (Figure 6E and F). However, we found that allowing the inhibitor to diffuse slows waves down only minorly (Figure 6F). In addition, waves are replaced by stationary patterns at high inhibitor diffusion (Figure 6E). We conclude

that simply adding a diffusing inhibitor to our model does not allow higher values of the activator diffusion constant, given the experimentally observed wave speed.

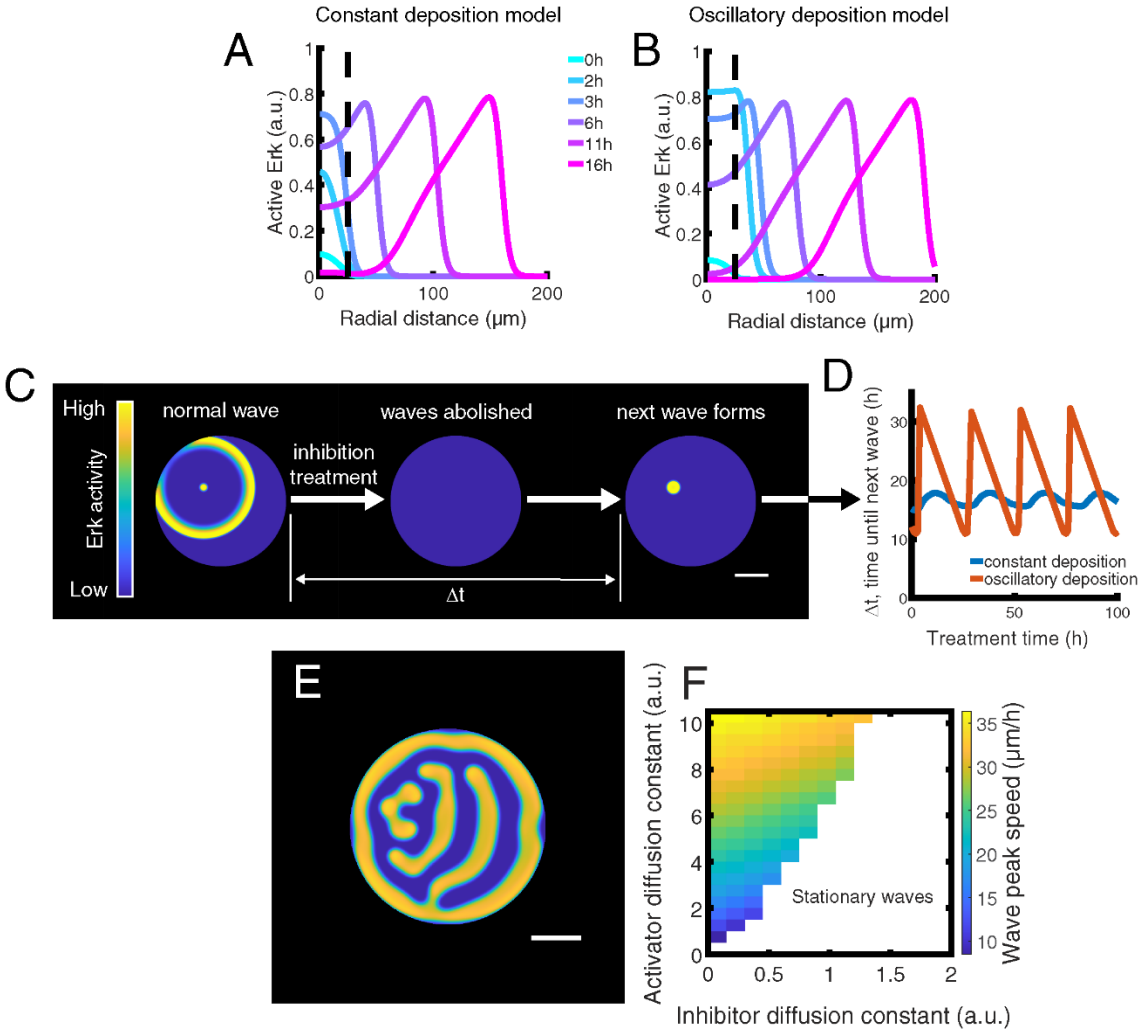

Figure 6: Variations in model type and assumptions. (A and B) Erk activity as a function of time in two models of wave generation at the source region. Dashed lines indicate the boundary of the source region. The standard model with a constant (A) or oscillatory (B) activator deposition in the source region is shown. (C and D) In silico Erk inhibition and recovery experiment. Pharmacological inhibition is implemented in our model by setting $\alpha 1$ to 0 for the duration of the treatment. (E and F) Alternative wave propagation model in which the Erk inhibitor diffuses. (E) Example of stationary pattern

established after 200 h of simulation time. (F) Wave peak speed as a function of activator and inhibitor diffusion constants relative to value of the activator diffusion constant in the standard simulation. Scale bars, 250 μm.

To understand the physical implications of the low value of inferred diffusivity, we tested the ability of a diffusible morphogen (Figure 7A) to propagate a signal across a domain of size similar to a regenerating adult zebrafish scale in a timescale like that of scale regeneration.[10] To that end, we simulated the dynamics of an undegradable/unprocessed diffusible morphogen produced at the source. We found that for D ≈ 0.1 μm2/s, it takes on the order of weeks to achieve a significant morphogen concentration across the domain (Figure 7B), whereas the wave mechanism in our model forms and propagates a wave across the same distance in just a couple days (Figure 7C). Thus, we conclude that for values of the diffusion constant of the activator similar to the ones we estimated, morphogen gradients established by diffusion are, in principle, not well suited to coordinate cellular dynamics on the observed timescales.

2.3.4 The effects of the geometry of the source on wave propagation

Wave geometry impacts the speed of excitable wave propagation according to the relationship v = vp + DK for normal and planar velocity v and vp, respectively, and curvature K (11,44). K is negative for wavefronts that curve away from the propagation direction. This relationship predicts that circular stable waves have a minimal radius. This critical radius is estimated to be Rc ≈ D/vp ≈ 45 μm in our system. However, in

simulations, we can observe wave propagation even when the source region is smaller than the critical radius (Figs. 1 D and 3, A and B). We hypothesize that this is because of the fact that diffusion generates a larger profile of baseline activator concentration surrounding the source, thus an "effective source region." The radius of this effective source region would be larger than that of the source by the order of magnitude of the activator diffusion length, $\sqrt{D\tau}$. Compatibly with this idea, the initial spatially inhomogeneous profile of activator triggers the system excitation at different times, thus resulting in a high apparent speed of the Erk activity peak in and around the source (Fig. 4 D). Thus, it is the size of this effective source region, and not the size of the source domain (i.e., when activator deposition $\alpha 2 > 0$), that determines whether a wave can propagate outward. To test this idea, we varied the amount of an initial pool of activator in the source region and tested system dynamics in the absence of additional activator production at the source ($\alpha 2 = 0$; Fig. 4 E). Depending on the initial concentration of activator, regions of different sizes were excited; for small initial activator amounts, small regions were excited, and when regions larger than the critical radius $Rc \approx D/vp \approx 45$ μm were activated, then the entire scale eventually reached excitation (Fig. 4 F). Thus, our results support the notion that Erk activity waves can propagate only when their radius of curvature is above a certain threshold. These results further argue against a value of the diffusion constant much larger than $D \approx 0.1$ μm2/s, as for such values the

effective source region would be significantly larger and occupy a large fraction, if not the entirety, of the scale tissue.

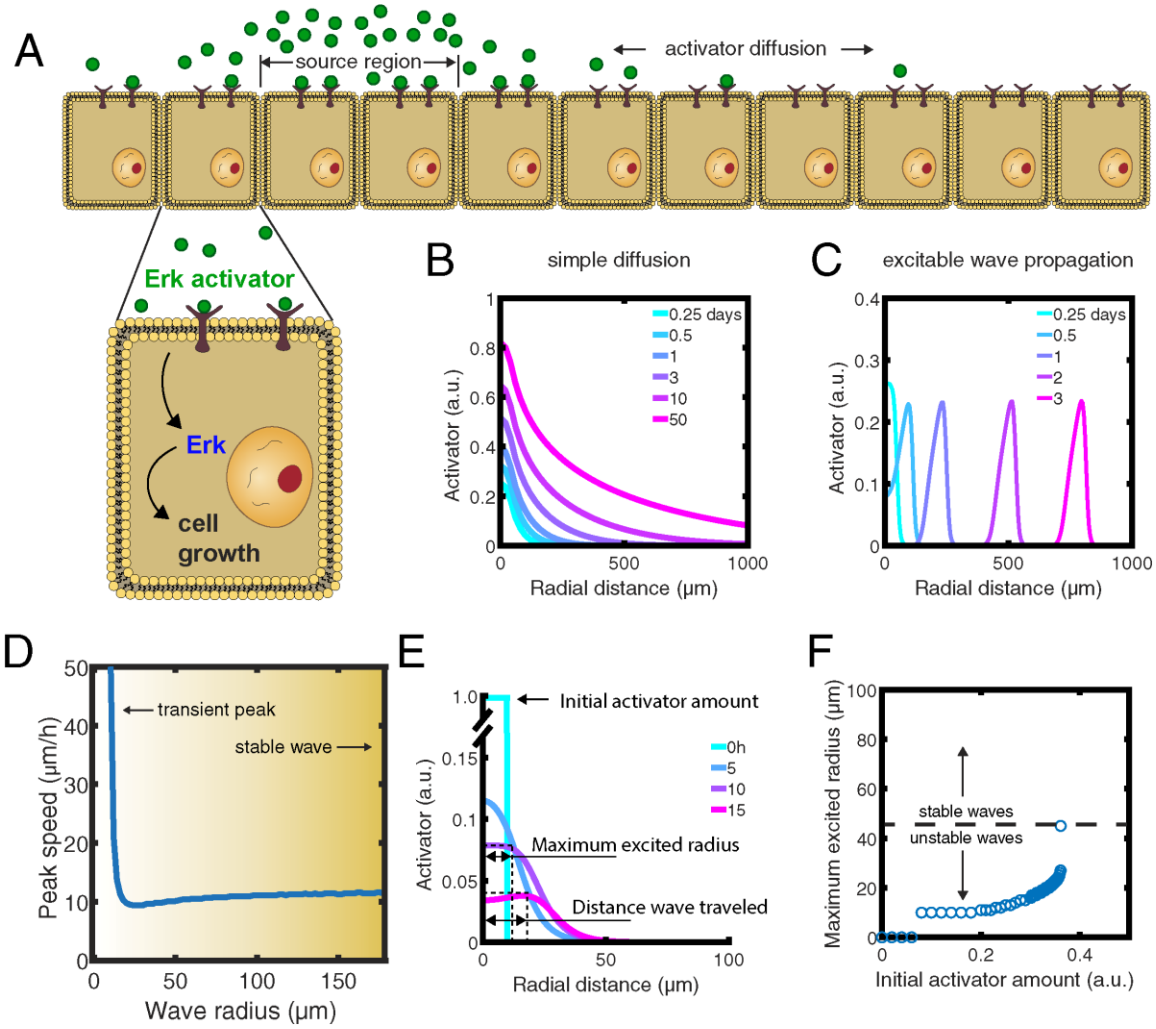

Figure 7: Consequences of activator diffusion constant and effects of curvature on wave propagation. (A) Schematics of activator gradient established by simple diffusion alone. (B and C) Activator gradient formation by simple diffusion (B) versus excitable wave propagation (C). (D) Wave speed as a function of radial distance from the source. (E) Definitions of wave profile characteristics. (F) Radius of the excited region for different initial activator amounts. Initial activator concentrations higher than ~0.36 E_T induced an excited radius above 45 μm and triggered wave propagation.

2.3.5 A change in activator deposition can control wave frequency during regeneration

During regeneration of zebrafish scales in vivo, wave generation starts with a frequency of ~1 wave per day and slows down over time until it stops (Figure 8A and B). Wave frequency directly controls the rate at which scales grow over the timescale of regeneration.[10] Our parameter analysis suggests that a change over time of the rate of deposition of the activator in the source region (α_2) could explain this phenomenology (Figure 5H). Alternatively, a change over time in the rate of degradation of the inhibitor $\gamma 3$ could reduce the frequency of wave generation (Figure 5I). We combined experimental data with the numerical predictions to infer how these two parameters would have to vary to explain the experimentally observed change in frequency. We found that an approximately exponential decrease of the activator deposition rate at the source over time (α_2) would be sufficient to explain wave generation dynamics (Figure 8C). Thus, reducing the amount of activator delivered to the regenerating scale could be a mechanism to control the duration of regeneration and thus the size of the regenerated scale. This exponential reduction of activator deposition could be achieved, for example, if the activator at the source was deposited by a pool of cells, each independently switching to a nondepositing state with a constant probability. Importantly, $\alpha 2$ controls only the dynamic of the source region, whereas the geometrical properties of the traveling excitable waves would be unaltered. Conversely, a reduction in the timescale of separation between Erk and the inhibitor (γ_3) could explain the slowing of wave

frequency but would result in an increase in wave width (Figure 8D). This can be understood by noting that for smaller γ_3, the time required to extinguish Erk increases, and thus, the width of the traveling Erk activity peak increases. Therefore, our results argue that the mechanism for controlling the duration of scale regeneration can be distinguished experimentally by monitoring waves throughout regeneration.

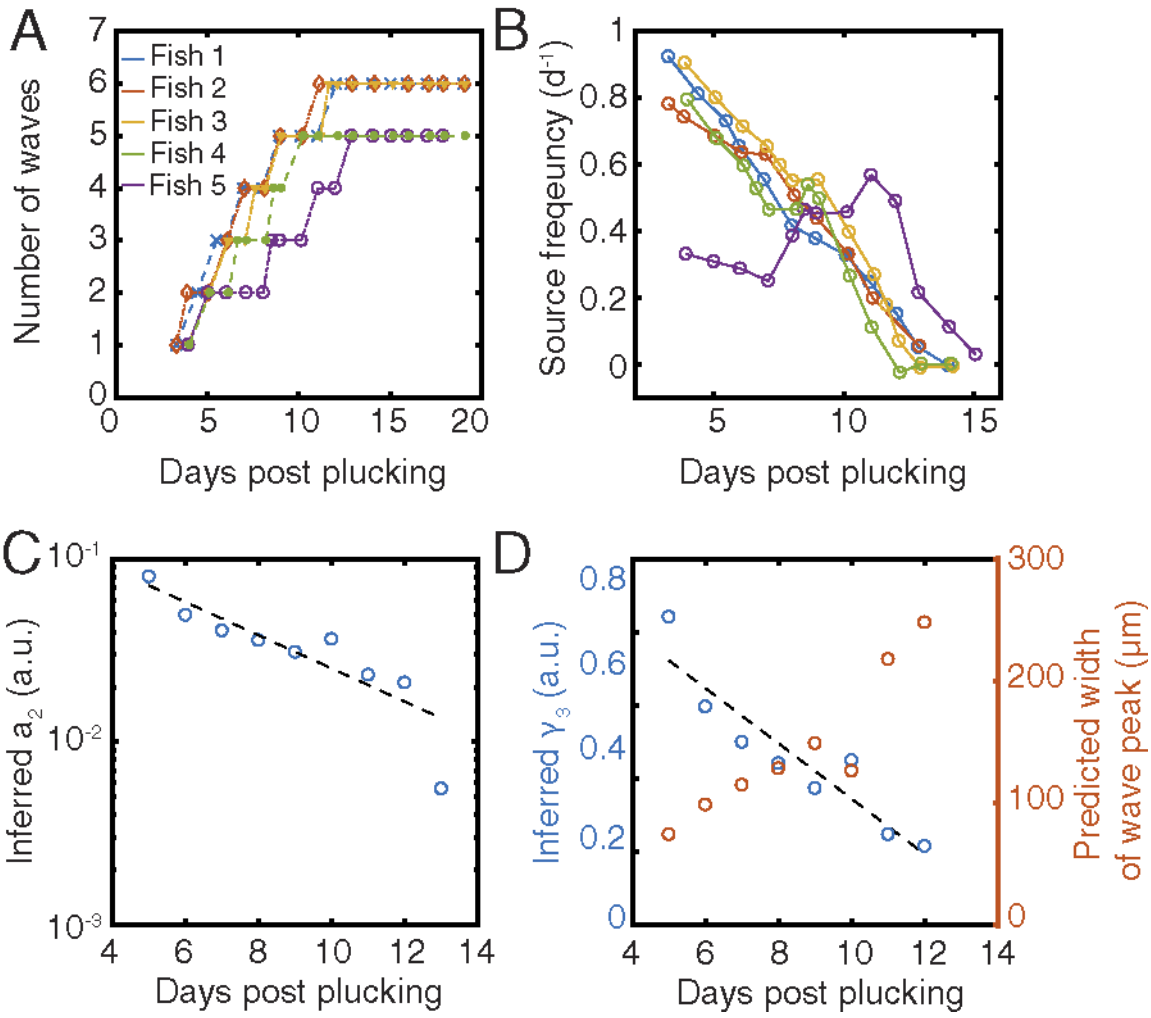

Figure 8: Effects of parameter changes on wave frequency. (A, B) Number of *in vivo* waves (A, panel adapted from [10]) and wave frequency (B) over the course of scale regeneration. (C) Inference of $\boldsymbol{\alpha_2}$ from experimentally measured wave frequency. Dashed line: exponential fit $\boldsymbol{\alpha_2 = \alpha_2(0)e^{-rt}}$ with $\boldsymbol{\alpha_2(0) = (0.20 \pm 0.05)}$ and $\boldsymbol{r =}$

$(\mathbf{0.21} \pm \mathbf{0.04})\mathbf{d^{-1}}$. (D) Inference of $\boldsymbol{\gamma_3}$ and wave width over time. Dashed line: linear fit $\boldsymbol{\gamma_3} = \boldsymbol{\gamma_3(0)} + \boldsymbol{rt}$ with $\boldsymbol{\gamma_3(0)} = (\mathbf{1.1} \pm \mathbf{0.1})$ and $\boldsymbol{r} = (\mathbf{-3.2} \pm \mathbf{0.6})\ \mathbf{10^{-3}\ h^{-1}}$. Inferred parameter values are relative to the values in the standard simulation.

2.4 Discussion

Waves can propagate stable signals across large tissues. We have recently reported that periodic waves of Erk activity, originating from a common source, control osteoblast regeneration in the zebrafish scale.[10] This work provides a rare example of a source region emitting repeated and coherent signals traveling across an entire growing and developing tissue. Here, we provide a mathematical model of Erk activity wave propagation in an excitable medium. At the core of this mechanism is an oscillatory source region, whose cellular nature and molecular regulation remain to be discovered. Once Erk activity is turned on in the source region, an excitable wave can travel across the rest of the tissue. Excitability requires positive and negative feedback mechanisms. Our analysis of the dependency of wave properties on model parameters supports the notion that the positive feedback between Erk and its activator controls the speed of the traveling wave. Conversely, the negative feedback between Erk and its inhibitor impacts the period of Erk excitable oscillations with little impact on wave speed. The periodic and repetitive nature of the wave is also controlled by the properties of the source region. Scenarios in which the ligand is continuously or periodically produced in the source region are both compatible with the observed repetitive nature of the waves. However, the two scenarios make different predictions on when a new wave would appear after inhibition of Fgf or Erk signaling. Future experiments should focus on

discovering the nature and dynamic properties of the source region and how Erk oscillatory activity is controlled in such regions. In particular, it will be important to discover whether the source region is created by interactions with other tissues, e.g., the vasculature or dermis, or whether cells in the source region become specified by a self-organized mechanism that locks them in an oscillatory Erk regime, thus making them act as pacemakers.

Erk activity waves in scale regeneration present features that are different from many previously observed examples of Erk activity propagation. In scale regeneration, Erk activity propagates as a stable wave, with a constant amplitude. Similar long-distance (several hundred microns) traveling waves have recently been discovered in the morphogenesis of the murine cochlear duct.[68] By contrast, in homeostatic mouse epidermis, ERK activity waves feature damped propagation up to ~50 μm and have a lifetime of ~30 min.[66] In the epithelium of Drosophila tracheal placodes, waves propagate comparable distances over the course of about an hour.[82]. Similar to the case of scale regeneration, in wound-healing assays, ERK activity waves can propagate from the edge of the wound for hundreds of microns, typically up to 200 μm. However, the remaining tissue displays a multitude of more disorganized waves that travel shorter distances (<~100 μm).[83] Less organized waves with origins influenced by noise are also seen in the activity of Cdk1 spanning the early Drosophila embryo to organize mitotic waves.[84,85]

The directionality of cellular flows is a crucial feature differentiating Erk activity waves in osteoblast regeneration from those reported in other systems. Thus, in the mouse epidermis and cochlear duct and in cultured MDCK cells, tissue flow is retrograde to the direction of ERK activity waves.[65-68] Instead, in osteoblast regeneration, Erk activity triggers tissue growth and thus leads neighboring cells away from the expanding region.[10] In fact, a retrograde flow in regenerating scales would move osteoblasts toward the central source region, arguably an undesirable feature for tissue growth. In the wound-healing assays and cochlear duct morphogenesis, cellular contractions precede ERK activation[65,68], whereas in our model, Erk activation triggers osteoblast hypertrophy and the corresponding cellular flows.[10] These observations suggest a different relationship between Erk activity waves and tissue flows in osteoblast regeneration and other systems. The Erk waves in scale regeneration and in wound healing are also characterized by different timescales. For example, Erk activity waves in regeneration are slower than those observed in wound healing (5–10 μm/h vs. ~60 μm/h).[65,66,69] This slower speed is accompanied by an overall slower oscillation of Erk activity in individual cells (~10 h in osteoblast regeneration vs. ~1 h seen in wound healing).

The slower dynamics and different flow patterns observed during osteoblast regeneration[10] argue for different mechanisms of wave propagation. In our experiments, Erk activates in ~3 h, a timescale compatible with a reaction-diffusion mechanism

involving the activation of gene expression. Consistently, inhibition of de novo protein synthesis decreases the speed of wave propagation.[10] Notably, a similar timescale or speed of propagation has been observed in the Drosophila eye imaginal disks, where the role of a transcriptional positive feedback is well documented.[86] In wound-healing assays, however, ERK activates in <1 h, which suggests that faster mechanisms are at play.[65] Consistent with this scenario, a mechanochemical mechanism in which the cleavage of pro-growth factor signaling molecules is coupled with cell contraction has been proposed.[65] Interestingly, ERK activity waves in murine cochlear duct morphogenesis have intermediate speeds and periods (~25 μm/h and ~3 h, respectively) and were proposed to originate from mechanochemical mechanisms similar to those of wound healing.[68]

Collectively, these observations suggest that different molecular processes can control Erk activity waves and that these processes might be selected to match the relevant timescales of the biological process. Interestingly, Erk waves are dependent on different ligand families in different contexts. Waves in regenerating osteoblasts and in the cochlear duct are Fgf dependent, whereas waves in wound healing are EGF dependent.[65,66] In the future, it would be interesting to determine whether and how the different mechanisms depend on different ligand and tissue properties.

The longer timescales of Erk oscillations also have implications on the possible mechanisms of the negative feedback that turns Erk activity off. Several negative

feedback mechanisms exist that may regulate Erk. Some of these mechanisms involve phosphorylation by active Erk, which can, for example, desensitize the pathway.[87] These mechanisms would likely operate on rapid timescales, and it is not obvious how they can be compatible with ~10 h of Erk excitation. However, mechanisms of negative feedback that involve the transcriptional activation of Erk inhibitors, namely proteins belonging to the Spry and Dusp families, are likely compatible with the timescales observed experimentally. In agreement with this, we previously reported that spry and dusp transcripts are enhanced in Erk active cells.[10]

The geometric features of Erk waves have interesting implications on the role of diffusion. If the diffusion constant is high, molecules quickly move away from the source region, and as a result, the system would require a high activator production to surpass the threshold to begin a wave. Moreover, a high diffusion constant is predicted to lead to wide waves and a more uniform-like Erk activation profile.[10] Because a wave-like pattern of Erk activity is more conducive to regeneration than a wide activation of Erk[10], this further argues against a high value of the diffusion constant. Finally, the speed of a stable wavefront is negatively influenced by curvature-dependent effects. These theoretical arguments suggest that the diffusion constant must be on the order of 0.1 μm2/s, which implies that simple diffusion would take several weeks to form a gradient across the tissue. It will be important for future experiments to investigate the receptors and ligand(s), as well as the extracellular matrix, determining the properties of

this system. In conclusion, we speculate that waves provide two important advantages in the regulation of scale regeneration: rapid delivery of growth factor signaling and stereotypical pulses of fixed amplitude eventually exciting all cells across the tissue. It is likely that excitable waves will emerge as a general principle of coordination of cell behaviors across large regenerating tissues.

2.5 Author contributions

L.D.H., K.D.P., A.D., and S.D. designed research. L.D.H. and A.D. performed numerical simulations. L.D.H., A.D., and S.D. analyzed the numerical and experimental data. L.D.H., A.D., and S.D. contributed analytical tools. L.D.H., A.D., and S.D. wrote the manuscript with comments from K.D.P.

2.6 Acknowledgements

A.D. was supported by Early (P2ELP3_172293) and Advanced (P300PA_177838) Postdoc. Mobility fellowships from the Swiss National Science Foundation, Switzerland. This work was supported by an Innovation in Stem Cell Science Award from the Shipley Foundation, Inc. to S.D. and National Institutes of Health grant R01-AR076342 to K.D.P. and S.D.

3 Cullin-5 mutants reveal collective sensing of the nucleocytoplasmic ratio in Drosophila embryogenesis

This chapter was modified from the manuscript: Luke Hayden, Anna Chao, Victoria E. Deneke, Massimo Vergassola, Alberto Puliafito, and Stefano Di Talia, Cullin-5 mutants reveal collective sensing of the nucleocytoplasmic ratio in Drosophila embryogenesis in review at Current Biology with an earlier version published as a pre-print to BioRxve, doi: 10.1101/2022.01.24.477546. The contributions of co-authors to the manuscript are detailed in Section 3.5 Author contributions.

3.1 Summary

In most metazoans, early embryonic development is characterized by rapid division cycles which pause before gastrulation at the mid-blastula transition (MBT).[88] These cleavage divisions are accompanied by cytoskeletal rearrangements which ensure proper nuclear positioning. Yet, the molecular mechanisms controlling nuclear positioning are not fully elucidated. In *Drosophila*, early embryogenesis unfolds in a multinucleated syncytium. Nuclei rapidly move across the anterior-posterior (AP) axis at cell cycles 4-6 in a process driven by actomyosin contractility and cytoplasmic flows.[5,89] In *shackleton* (*shkl*) mutants, this axial spreading is impaired.[90] Here, we show that *shkl* mutants carry mutations in the cullin-5 (cul-5) gene. Live imaging experiments show that Cul-5 is downstream of the cell cycle but required for cortical actomyosin contractility. The nuclear spreading phenotype of cul-5 mutants can be rescued by reducing Src activity, suggesting that a major target of Cul-5 is Src kinase. cul-5 mutants

display gradients of nuclear density across the AP axis which we exploit to study cell cycle control as a function of the N/C ratio. We found that the N/C ratio is sensed collectively in neighborhoods of about 100μm and such collective sensing is required for a precise MBT in which all the nuclei in the embryo pause their division cycle. Moreover, we found that the response to the N/C ratio is slightly graded along the AP axis. These two features can be linked to Cdk1 dynamics. Collectively, we reveal a new pathway controlling nuclear positioning and provide a dissection of how nuclear cycles respond to the N/C ratio.

3.2 Results

3.2.1 *shkl* encodes the ubiquitin ligase *cullin-5*

shkl mutants are among the few available genetic perturbations which directly impinge on the spreading of nuclei in early *Drosophila* embryogenesis.[90,91] Moreover, *shkl* embryos display gradients in nuclear density, which have been linked to a significant decrease in the synchrony of the last cell cycle preceding the MBT.[5] To elucidate how *shkl* regulates nuclear positioning and how such regulation impacts cell cycle lengthening at the MBT, we first obtained two *shkl* alleles identified in the original mutagenesis screen (*shkl*^{GM130} and *shkl*^{GM163}) and imaged embryos laid by transheterozygous mothers (hereinafter *shkl* embryos). We confirmed that in *shkl* embryos the nuclear cloud failed to reach the posterior pole of the embryo at the correct time and nuclei were not positioned uniformly, as seen previously (Figure 9A-B).[90]

Moreover, we found that the lower density of nuclei in the posterior of the embryo was frequently accompanied by an extra round of nuclear divisions. Thus, failures in nuclear positioning can have significant impact on the decision of nuclei to lengthen the cell cycle at the MBT.

To identify the *shkl* gene, we used a DNA sequencing approach, centered on the fact that the original screen was performed in a strain carrying an isogenic third chromosome and that two alleles of the shkl gene were available.[90] We reasoned that the third chromosomes of these two alleles had little time (~20 years) to accumulate mutations with respect to each other. Thus, we predicted that genomic sequencing of *shkl* flies ($shkl^{GM130}/shkl^{GM163}$) would show a much lower number of heterozygous single nucleotide polymorphisms (SNPs) than homozygous ones relative to the reference genome on the third chromosome, a prediction which we readily confirmed (Figure 9C). Taking advantage of the low number of heterozygous SNPs and the previous mapping[90] of *shkl* between two markers (ebony and claret) on the right arm of chromosome 3, we looked for genes that carried two heterozygous missense SNPs with the idea that this would narrow our search to only a handful of genes (Figure 9D). Bioinformatics analysis confirmed the validity of this argument, and we identified cullin-5 (Cul-5) as the best candidate as allele $shkl^{GM163}$ carried a premature stop codon at amino acid 51 and $shkl^{GM130}$, a missense mutation (E to K) in the very conserved neddylation domain, a domain required for ubiquitin ligase activity and which is well conserved across

evolution (Figure 9E).[92] To perform complementation and rescue experiments, we fixed and stained embryos with DAPI to estimate the extent of nuclear spreading by measuring the shape of the nuclear cloud in cell cycle (cc) 6. We found that *shkl* alleles failed to complement an available cullin-5 mutant (Figure 9F). In addition, maternal expression of cullin-5 from the twine promoter (which drives expression specifically in the germline[93]) was able to significantly rescue the nuclear spreading defects (Figure 9F). Collectively, these results identify *shkl* mutants as alleles of the cullin-5 genes and demonstrate that maternal expression of cullin-5 is important for nuclear positioning in *Drosophila* embryos.

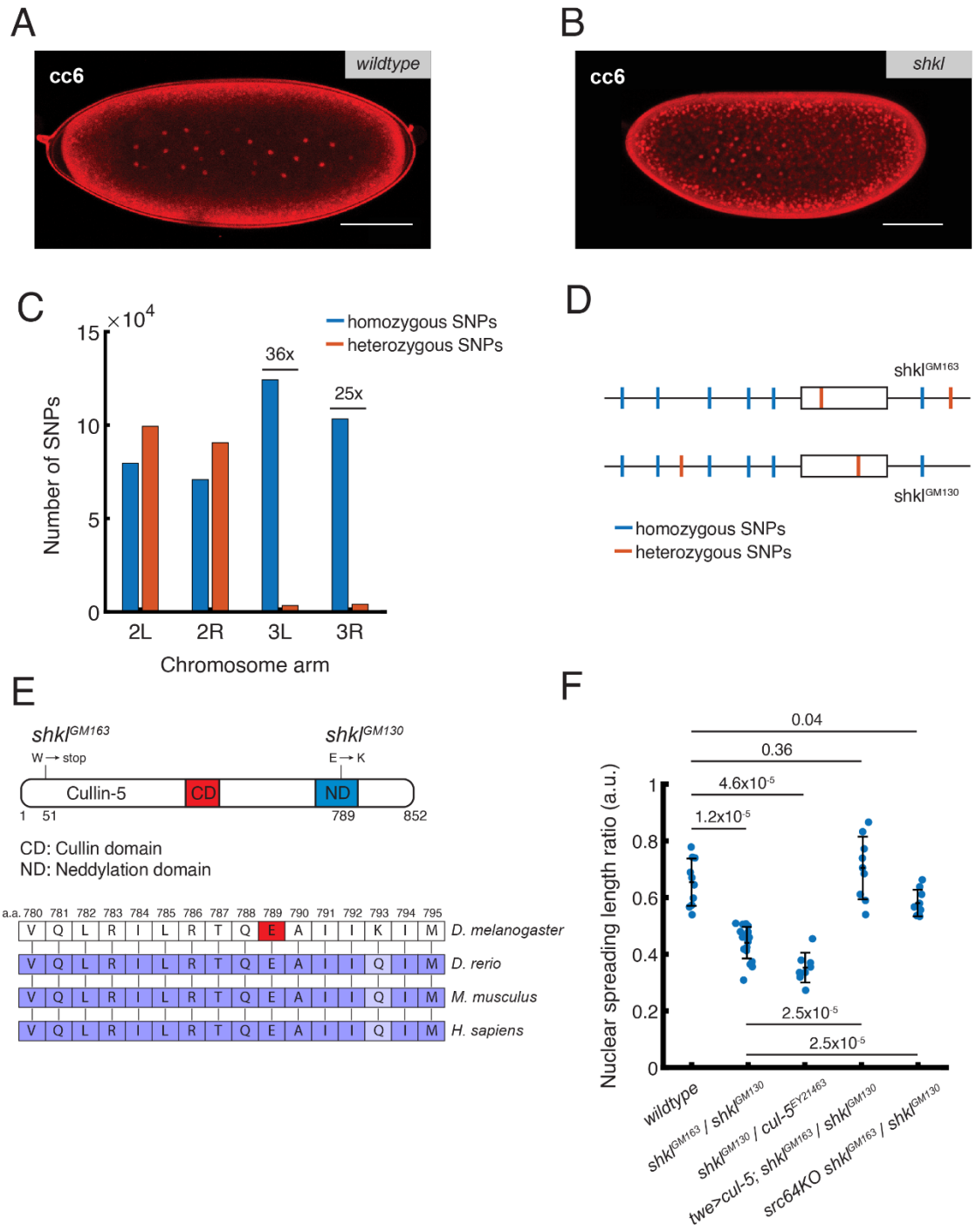

Figure 9: Genetic identification of shkl mutants. (A, B) Nuclear positioning in interphase of cc 6 in wildtype (A) and shkl (B) embryos, visualized with PCNA-TagRFP. (C) Number of homozygous and heterozygous SNPs (relative to the reference genome) in shkl embryos in each arm of chromosome 2 and 3. The mutant screen[90] was

performed on an isogenic third chromosome and thus only the third chromosome has reduced heterozygous SNPs. (D) A theoretical example gene with heterozygous SNPs between the two shkl alleles. (E) Top: Schematic for the Cul-5 protein with domains and shkl mutations shown. The GM130 allele of shkl contains a point mutation in the neddylation domain where it is evolutionarily conserved. The GM163 allele contains a point mutation leading to an early stop codon. Bottom: Part of the neddylation domain of the Cul-5 protein in different model organisms. Highlighted residue indicates GM130 mutation site. (F) Genetic complementation and rescue tests. Fixed embryos were stained with DAPI to show nuclear positioning at cc 6. The ratio between the length of the nuclear cloud and the length of the embryo was measured. Data are represented as mean ± SEM. P-values (Kolmogorov– Smirnov test) are shown. Each dot represents one embryo. cul-$5^{EY21463}$ is a hypomorphic mutant allele. twe>cul-5 is a transgenic line carrying a plasmid with cul-5 cDNA under the regulation of the twine promotor. Scale bar: 100μm.

3.2.2 *shkl* is downstream of the cell cycle and regulates cortical contractility

In our previous work, we showed that nuclear spreading is driven by cytoplasmic flows generated by cortical actomyosin contractility, which is in turn controlled spatiotemporally by the cell cycle oscillator (Figure 10A).[5] To quantify the degree to which cytoplasmic flows are disrupted in *shkl* embryos, we used yolk autofluorescence images to perform particle image velocimetry (PIV) in live embryos also expressing PCNA-TagRFP (which allows visualization of nuclei deep in the embryo) and measured the velocity of the cytosol and nuclei during the early cell cycles when axial expansion occurs. As previously shown, the wildtype embryos showed strong cytoplasmic flows coupled with nuclear movement which spread the nuclei

across the anterior-posterior (AP) axis by the end of cc 6 (Figure 10B, D, Figure 11).[5] In contrast, cytoplasmic flows and nuclear movement in *shkl* embryos were sharply reduced (Figure 10C, E, Figure 11). Since cytoplasmic flows are generated by recruitment of active Myosin II to the cortex by active Rho[5,94] we sought to determine if the activities of these regulators are perturbed in *shkl* embryos. To that end, we measured the dynamics of a Rho biosensor[95] and myosin II recruitment to the embryo cortex. Both Rho activity (Figure 10F, Figure 11) and myosin II recruitment (Figure 10G) were reduced in *shkl* embryos as compared to wildtype. Next, we analyzed whether Cul-5 might impact actomyosin contractility by regulating the cell cycle. To this end, we measured the Cdk1-to-PP1 activity ratio using a FRET-based biosensor in both wildtype and *shkl* embryos.[84,96] The oscillations in the activity ratio were similar in wildtype and *shkl* embryos. Moreover, the duration of the cell cycle near the middle of the embryo was also essentially unaltered (Figure 10H, Figure 12). Therefore, we argue that Cul-5 does not regulate the cell cycle oscillator. Taken together, our results indicate that Cul-5 is necessary for the proper activity of Rho and recruitment of myosin II which in turn regulate cortical contractility and nuclear positioning.

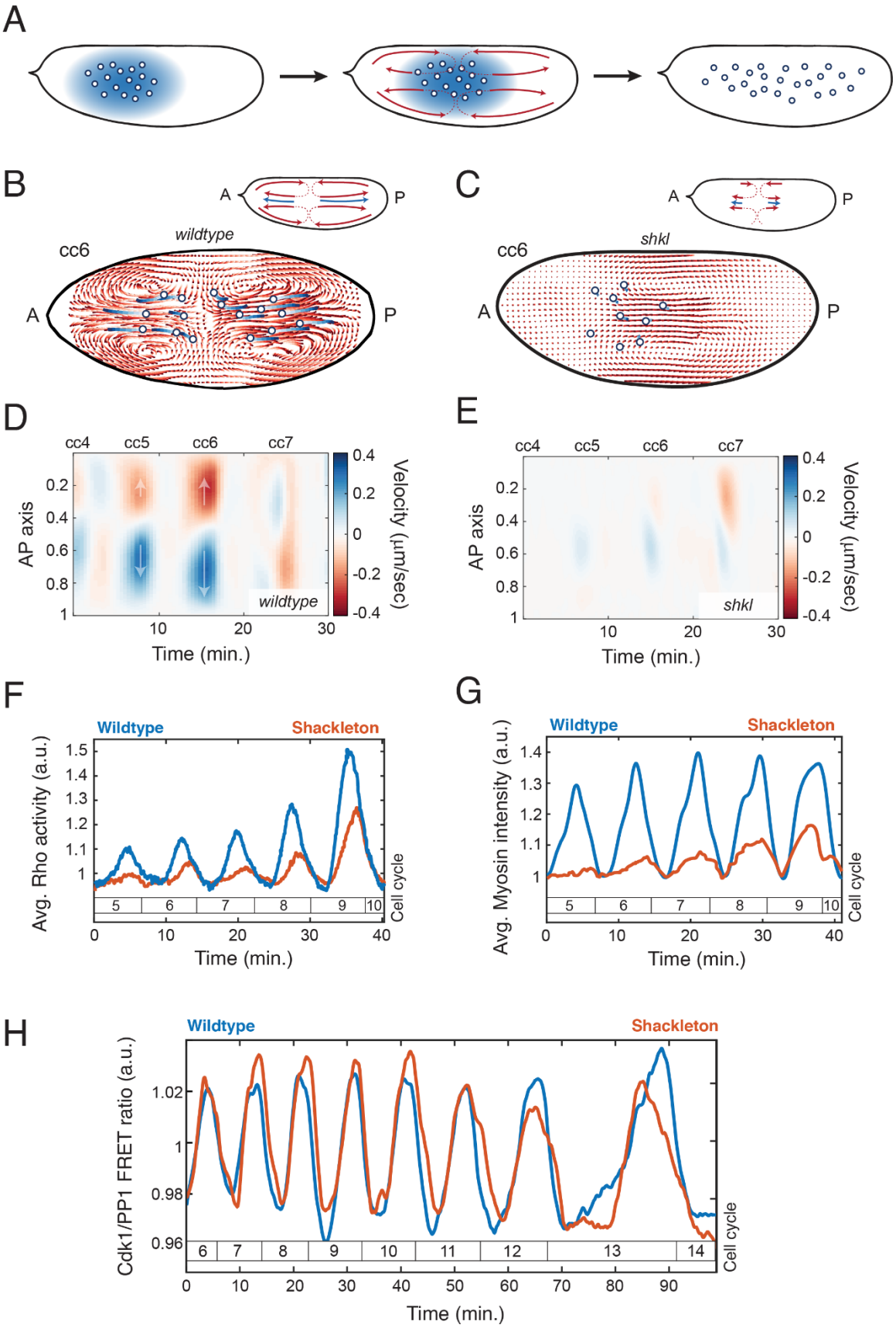
A
B
wildtype
cc6
A
P
C
shkl
cc6
A
P
D
cc4
cc5
cc6
cc7
AP axis
0.2
0.4
0.6
0.8
1
wildtype
10
20
30
Time (min.)
0.4
0.2
0
-0.2
-0.4
Velocity (µm/sec)
E
cc4
cc5
cc6
cc7
AP axis
shkl
Time (min.)
Velocity (µm/sec)
F
Wildtype
Shackleton
Avg. Rho activity (a.u.)
1.5
1.4
1.3
1.2
1.1
1
5
6
7
8
9
10
Cell cycle
0
10
20
30
40
Time (min.)
G
Wildtype
Shackleton
Avg. Myosin intensity (a.u.)
1.4
1.3
1.2
1.1
1
Cell cycle
Time (min.)
H
Wildtype
Shackleton
Cdk1/PP1 FRET ratio (a.u.)
1.02
1
0.98
0.96
6
7
8
9
10
11
12
13
14
Cell cycle
0
10
20
30
40
50
60
70
80
90
Time (min.)

Figure 10: Characterization of the Cul-5 pathway. (A) Pathway for self-organized nuclear positioning in wildtype embryos; PP1 activity spreads from nuclei to the embryo cortex where it leads to gradients of myosin accumulation, thus generating cytoplasmic flows. These flows position nuclei uniformly across the AP axis. (B, C) PIV in wildtype (B) and *shkl* (C) embryos showing reduced cytoplasmic flows and nuclear movement in *shkl* embryos. Top insets depict magnitude and directionality of flows. (D, E) Heatmap quantification of the cytoplasmic flows in wildtype (D) and *shkl* (E) embryos. Arrows depict directionality of flows. (F, G) Both cortical Rho activity (F) and cortical myosin accumulation (G) are reduced in *shkl* embryos. (H) Cortical oscillations of the Cdk1/PP1 ratio from the FRET biosensor are similar in wildtype and *shkl* embryos.

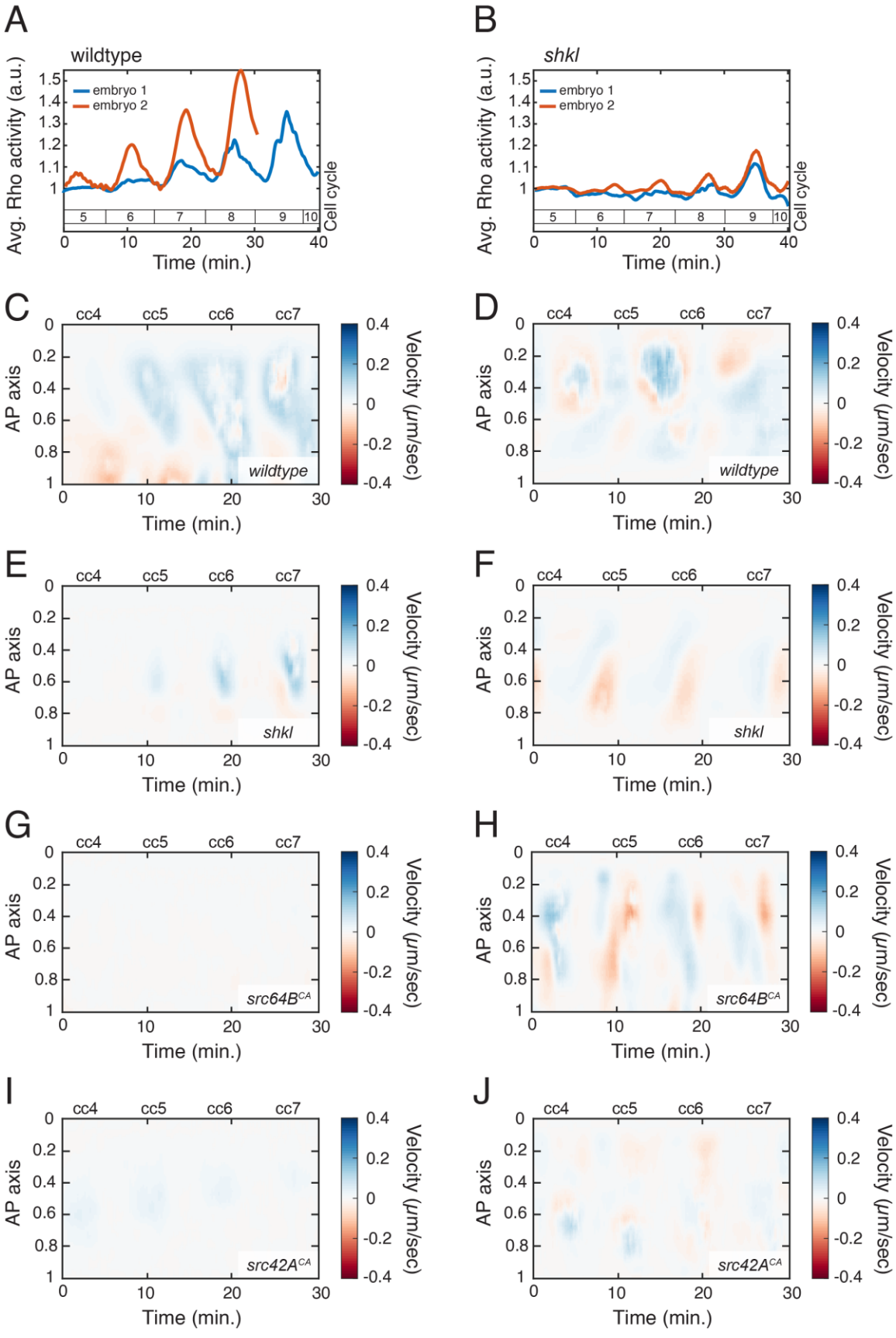
A
wildtype
embryo 1
embryo 2
Avg. Rho activity (a.u.)
Cell cycle
Time (min.)
B
shkl
C
D
E
F
G
H
I
J
cc4
cc5
cc6
cc7
AP axis
Velocity (μm/sec)
wildtype
shkl
src64B^CA
src42A^CA

Figure 11: Quantification of cortical contractility and cytoplasmic flows. (A, B) Replicate quantification of Rho activity in wildtype (A) and shkl (B) embryos. (C-J) Replicate heatmap quantification of cytoplasmic flows in wildtype (C, D) shkl (E, F), src64B overexpression (G, H), and src42A overexpression (I, J).

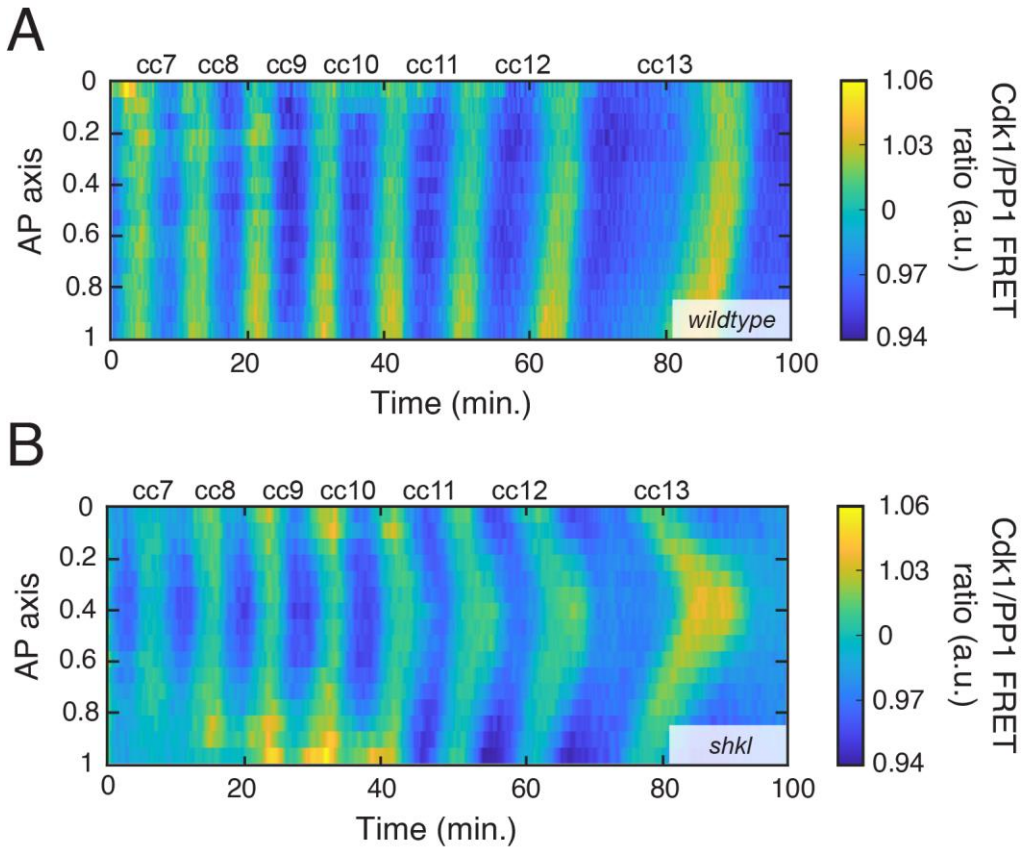

Figure 12: Spatial quantification of Cdk1/PP1 FRET sensor. Cdk1/PP1 FRET emission ratio for wildtype (A) and shkl (B) embryos, measured across the AP axis and time. In time, oscillations are unperturbed, and cell cycle duration is unchanged. The lower nuclear density in the posterior relative to the anterior lead to slightly earlier divisions and a gradual asynchrony in cell division builds up over time.

3.2.3 Cul-5 regulates cortical contractility through restricting the activity of Src

Cul-5 is a ubiquitin ligase which works in conjunction with other factors to regulate protein stability.[97] A major target of Cul-5 is Src kinase[98-100], whose activity is restricted by several ubiquitin ligases.[101-103] Src is known to regulate the cytoskeleton[104,105], including actomyosin contractility.[106] These observations suggest that Cul-5 could (at least partly) regulate the axial expansion process by restricting Src activity. To test this hypothesis, we performed experiments using the Gal4/UAS system to overexpress constitutively active forms of the two Src homologs in *Drosophila*, Src42A or Src64B.[107] We saw that overexpression of either homolog is sufficient to recapitulate the *shkl* phenotype with sharply reduced cytoplasmic flows and nuclear spreading (Figure 11). Similarly, if *shkl* embryos have reduced cortical contractions due to excessive Src activity, then genetically decreasing Src activity should rescue the *shkl* phenotype. We examined *shkl* mutants also carrying only one functional copy of Src64B (heterozygous for Src64BKO, described previously[105]) and quantified cytoplasmic flows and nuclear positioning. We saw that reducing Src activity in *shkl* embryos significantly reduced the defects in axial expansion (Figure 9F). Collectively, these results implicate the Cul-5/Src cascade in the regulation of nuclear positioning in *Drosophila* embryos.

3.2.4 Nuclei sense the local nuclear density in large groups to determine whether to divide

In wildtype embryos, the morphogenetic processes driving nuclear positioning ensure that nuclear density is rather uniform across the embryo.[5] Since nuclear divisions are synchronized within minutes[84,108] by Cdk1 waves[43,84], nuclear density increases in 2-fold increments, which likely facilitates the consistent cell cycle lengthening observed in all nuclei at the MBT. To gain insights on how the embryo can achieve a robust response to changes in the N/C ratio, we observed that the nuclear spreading defects in *shkl* embryos cause a nuclear density gradient across the AP axis with lower density at the posterior (Figure 13A-B, Figure 15B). Therefore, we exploited this gradient to probe the response to gradual changes in nuclear density. We observed that the lower density of nuclei in the posterior of the embryo is frequently accompanied by an extra round of nuclear division (Figure 13C). Interestingly, the size of the region which does an extra division varies across embryos and is frequently less than half the size of the embryo. Moreover, a salt-and-pepper phenotype with many regions of extra divisions next to regions of normal divisions is never observed.[40,109,110] These two observations suggest that the nuclei do not sense the N/C ratio globally or in an autonomous manner, but rather they do so in a collective manner over some distance, here called the community radius. To infer this radius, we divided embryos into grids, measured the nuclear density within circles of different radii, and scored whether each grid point was within a region of normal or extra division (Figure 13D). We then fit these curves to logistic

equations and used the N/C ratio at which the curves crossed 50% probability as the best N/C ratio threshold predictor, above which we predict embryos do not divide (Figure 13E). As previously reported, these thresholds were around 70% of the wildtype cell cycle 14 nuclear densities.[40] This value is about half-way between the nuclear density at cell cycle 13 and 14, which likely contributes to the decision of all nuclei to divide rapidly at cell cycle 13 and lengthen their cycle 14. Next, we asked what is the fraction of nuclei that would fail to lengthen their cell cycle at the MBT as a function of the community radius. We found that to ensure that all nuclei (>99%) undergo a collective pause at the MBT, the response to the N/C ratio must be averaged over a community radius of at least 35μm (Figure 13F). Such a community would contain about one hundred nuclei, thus implying that a robust cell cycle decision at the MBT requires a collective nuclear response.

Next, we tried to infer the optimal radius and a possible molecular mechanism for the collective nature of the cell cycle decision. Using the estimated thresholds, we measured the proportion of correct predictions made in a test data set of *shkl* embryos with regions of extra division and saw a peak in the fraction of correct predictions at a community radius of about 70μm (Figure 13F). We used the Cdk1/PP1 FRET biosensor to measure the correlation length of the Cdk1/PP1 activity field. The correlation length can be estimated from the two-point correlation function, which measures how variables at different positions co-vary with one another. Specifically, we measure how Cdk1/PP1

activity at a position relates on average to Cdk1/PP1 activity at distance x. We found that the correlation length (about 100 μm) is similar to the optimal community radius, thus suggesting that the collective decision of nuclei to undergo an extra division or not might reflect the fact that Cdk1/PP1 activity in neighboring nuclei influences each other (Figure 13G). We have previously shown that spatial correlations in Cdk1/PP1 activity arise from the reaction-diffusion dynamics that drive the cell cycle during interphase.[43] To strengthen this argument, we performed numerical simulations of a mathematical model of Cdk1 activity[43] in the presence of spatially varying N/C ratios. Our model assumes that the N/C ratio locally sets different levels of activation of the DNA replication checkpoint, which feeds into Cdk1 activity via Chk1. The reaction-diffusion dynamics of Cdk1 activity then smoothen these inhomogeneities and result in nuclei collectively deciding whether to divide or not within regions of about 70 microns in radius (Figure 13H, Figure 14). Thus, our model and experiments suggest a phenomenological mechanism for the N/C-based decision process that controls nuclear divisions. We conclude that the syncytial nature of the nuclear cycles coupled to the reaction-diffusion properties of the cell cycle oscillator ensure that nuclei act as large collectives and that such collectives increase the robustness of the MBT. Finally, we found that nuclear density can also predict the duration of cycle 13 in shkl embryos (Fig. 3I and S3), in line with a model in which the N/C ratio sets the levels of Chk1 activation which, in turn, controls cell cycle duration.[84,111]

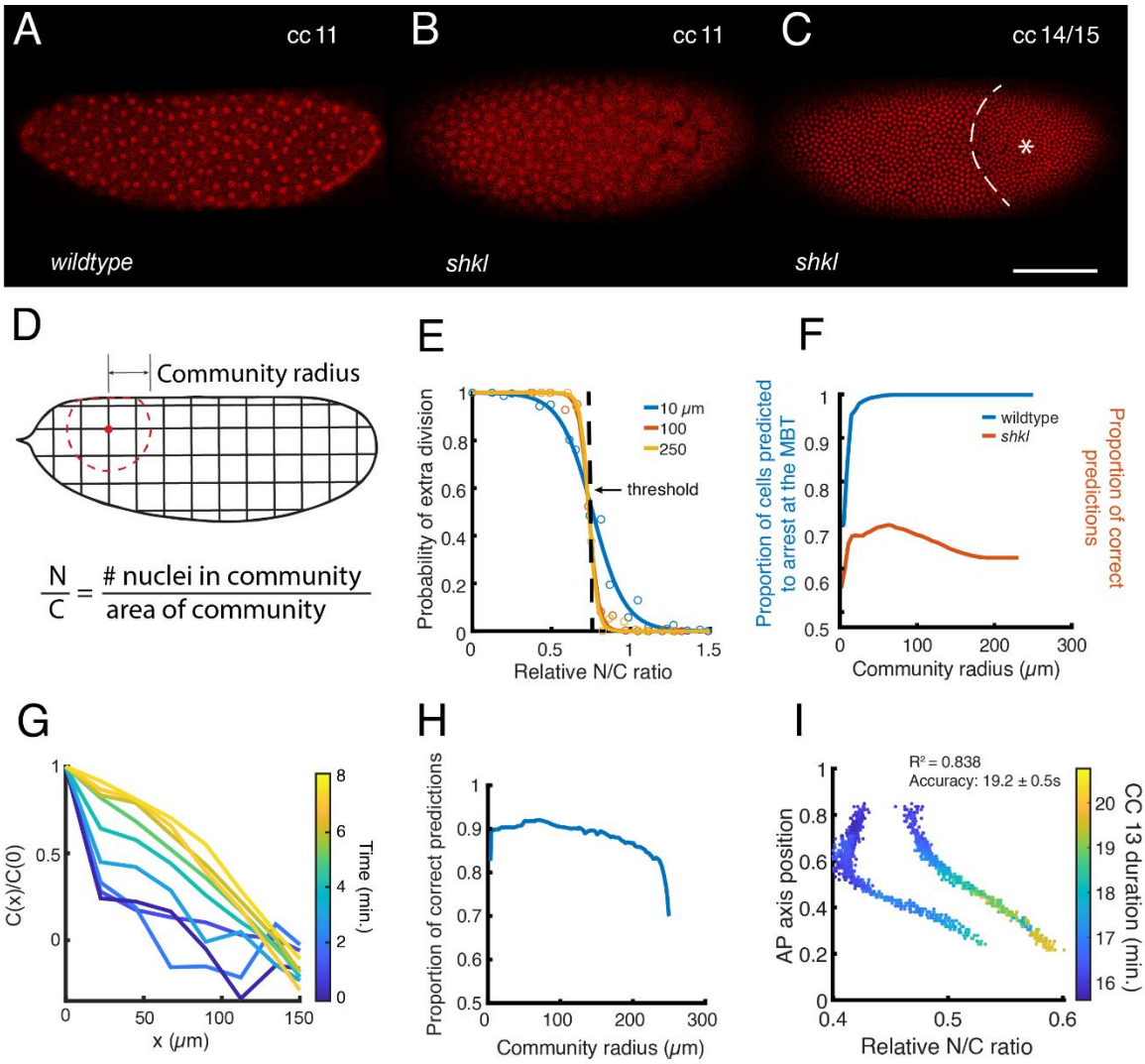

Figure 13: Sensing of the N/C ratio in shkl embryos. (A, B) Positioning of nuclei at cc 11 in wildtype (A) and shkl (B) embryos, visualized with His-RFP. (C) A shkl embryo at the MBT. The gradient of N/C ratio in shkl embryos frequently leads to the posterior undergoing an extra division. Dashed line: boundary between the normal and extra division regions. Asterisk: The region of the embryo which underwent an additional division. (D) Schematic of experimental design. Each embryo was discretized in a grid and a region with a certain community radius was specified. The N/C ratio was calculated as the number of nuclei in the community divided by the area. (E) The probability of a region dividing as a function of the local N/C ratio, relative to the average N/C ratio in wildtype embryos at cc 14. Curves for local neighborhoods of 10, 100, and 250μm are shown. A simple predictive model is a constant N/C ratio threshold, shown as a dashed line. (F) The proportion of nuclei in wildtype embryos which should

arrest at the MBT and the proportion of correct predictions in a test data set of shkl embryos using a simple threshold model as a function of community radius. (G) Two-point correlation function of the Cdk1/PP1 field as a function of distance for embryos in interphase of cell cycle 13. The correlation length was estimated as the point at which the correlation reaches 0.5 at the last time point and occurs at ~100μm. (H) The proportion of correct predictions in the *in-silico* data set of 22 embryos with a N/C ratio gradient across the AP axis. (I) Duration of cc 13 in 30μm neighborhoods as a function of N/C ratio and position across the AP axis. Accuracy is the average ± SEM of the error in prediction. Scale bar: 100μm.

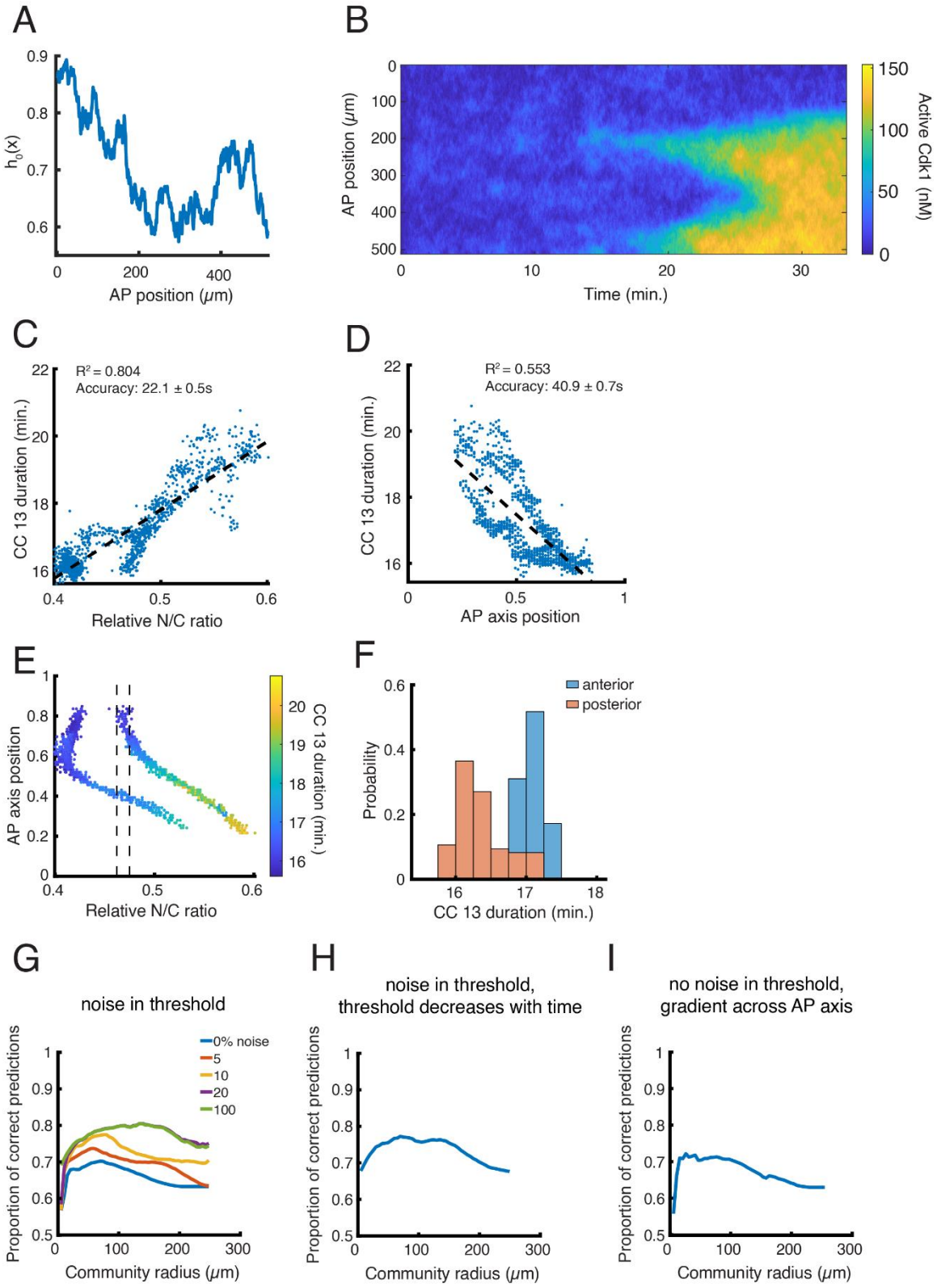
A
B
C
D
E
F
G
H
I
AP position (μm)
Time (min.)
Active Cdk1 (nM)
CC 13 duration (min.)
Relative N/C ratio
AP axis position
Probability
anterior
posterior
R² = 0.804
Accuracy: 22.1 ± 0.5s
R² = 0.553
Accuracy: 40.9 ± 0.7s
noise in threshold
noise in threshold, threshold decreases with time
no noise in threshold, gradient across AP axis
Proportion of correct predictions
Community radius (μm)
0% noise
5
10
20
100

Figure 14: Additional models of N/C ratio sensing. (A, B) N/C ratio parameter (A) and simulation (B) of the Cdk1 activity model with a gradient of N/C ratio across the AP axis to recapitulate a shkl phenotype. The simulation shows the low nuclear density in the posterior has resulted in the posterior entering mitosis while the anterior has paused divisions. (C-F) The duration of cc 13 can be predicted by the N/C ratio (C), position across the AP axis (D), and is well predicted by both (E). Dashed lines indicate a small region of N/C ratio in two different embryos with different AP positioning. (F) Histogram of cc 13 durations in the anterior and posterior. With the same nuclear density, the anterior of the embryo tends to have a longer duration of cc 13. (G-I) Proportion of correct predictions in possible models of N/C ratio sensing. (A) The decision to pause the cell cycle is determined by a global threshold of ~70% (see main text Fig. 3E) which varies up to a certain percentage of this threshold (colored lines). Allowing "noise" of 10% means the threshold for that embryo must fall in the range [1/1.1 to 1.1]. (B) The decision to pause the cell cycle is determined by a global threshold (Fig. 3E) with an additional gradient in threshold of up to 10% across the AP axis. (C) The decision to pause the cell cycle is determined by a global threshold with noise (as in panel B). Additionally, when the first nucleus divides, the threshold lowers at some rate over time (tested uniformly from 0 to up to 15%/minute), making it more difficult for nuclei to divide.

3.2.5 A gradient in sensing of the N/C ratio improves the ability to predict nuclear behaviors

While our previous results revealed the importance of collective N/C ratio sensing, we observed that the frequency of correct predictions from the model was limited to ~70% (Figure 13F), suggesting that we might be missing some additional regulation of the MBT or some additional aspects of the response to the N/C ratio. Thus, we sought to determine whether a more complex model, still centered on the N/C ratio, would account for the incorrect predictions (see Figure 14). Notably, we found that the errors in prediction were distributed in a gradient across the AP axis (Figure 15A), suggesting that nuclei might sense the N/C ratio differently depending on their location.

We therefore hypothesized that a slight gradient in the N/C ratio threshold (with some small variance between embryos) would be a better predictor (Figure 15B). With this model, we were able to correctly predict ~90% of nuclear divisions with the best community radius of ~100μm (Figure 15C). Moreover, most of the errors in this model accumulated very close to the border of the normal and extra division regions (Figure 15D), where we would expect that the ability of Cdk1 to propagate spatially might influence the decision.[43,84,112,113]

To further test the idea that the posterior of the embryo has a slightly higher N/C ratio threshold than the anterior, we compared the probability of nuclei dividing as a function of N/C ratio in the anterior and posterior. As predicted, the posterior third of the embryo showed a higher N/C ratio threshold than the anterior third (~8% higher, Figure 15E) which was independent of the community radius used (Figure 15F). To control that the apparent gradient in N/C ratio response is not due to cytoskeletal and/or other effects of reduced Cul-5 activity, we investigated the decision of nuclei to arrest at the MBT when the N/C ratio in embryos (with uniform nuclear positioning) is brought closer to the threshold by genetic manipulations. We reasoned that in these embryos the proximity of the nuclear density to the threshold will result in a significant fraction of embryos having an extra division. To this end, we imaged embryos generated by crossing wildtype females to males carrying compound chromosomes[40]. As a consequence, these embryos contained either one extra or one fewer copy of either

chromosome 2 or 3. The embryos with one fewer copy of chromosome 2 or 3 have a DNA content (83% and 80% respectively) close to the 70% threshold seen in wildtype and also frequently had regions of an extra nuclear division.[40] As in *shkl* embryos, the posterior of the embryos featured a slightly higher threshold than the anterior (~2% increase for chromosome 2 and ~8% increase for chromosome 3; Figure 15G). In accordance, 100% (n=33) of extra divisions began in the posterior. The N/C ratio is an excellent predictor of the decision of nuclei to divide also in embryos with altered DNA content (Figure 16). However, the optimal threshold is shifted to higher values (~0.85, 11% higher than in wildtype; Figure 15G) which explains why a large number of extra divisions are observed in embryos with only one copy of chromosome 2 or 3. Since the community radius and the correlation length of the Cdk1/PP1 field are both ~100μm, we expect there to be a correlation between the Cdk1 activation rate measured during S phase (Figure 15H) and nuclear density in the compound chromosome embryos. Indeed, we saw there was a correlation between the two, and the regions of the embryo which underwent an extra division were clustered at a low DNA content and higher Cdk1 activation rate (Figure 15I).

To gain further insight on the slight gradient in the N/C ratio threshold across the AP axis, we divided wildtype embryos into grids and measured the Cdk1 activation rate in neighborhoods of each grid point at cc 13. We saw a slight but significant increase in the Cdk1 activation rate across the AP axis (Figure 15J) which was not due to

differences in the N/C ratio (Figure 16). Since the increased duration of S phase at cc 13 is primarily due to the Cdk1 inhibition by Chk1[114-116], we measured the Cdk1 activation rate in *chk1 chk2* mutants and saw that the gradient across the AP axis was ablated (Figure 15K, Figure 16). Thus, our results argue that the response of the cell cycle to nuclear density is not uniform across the embryo and that this difference might be dependent on the DNA replication checkpoint.

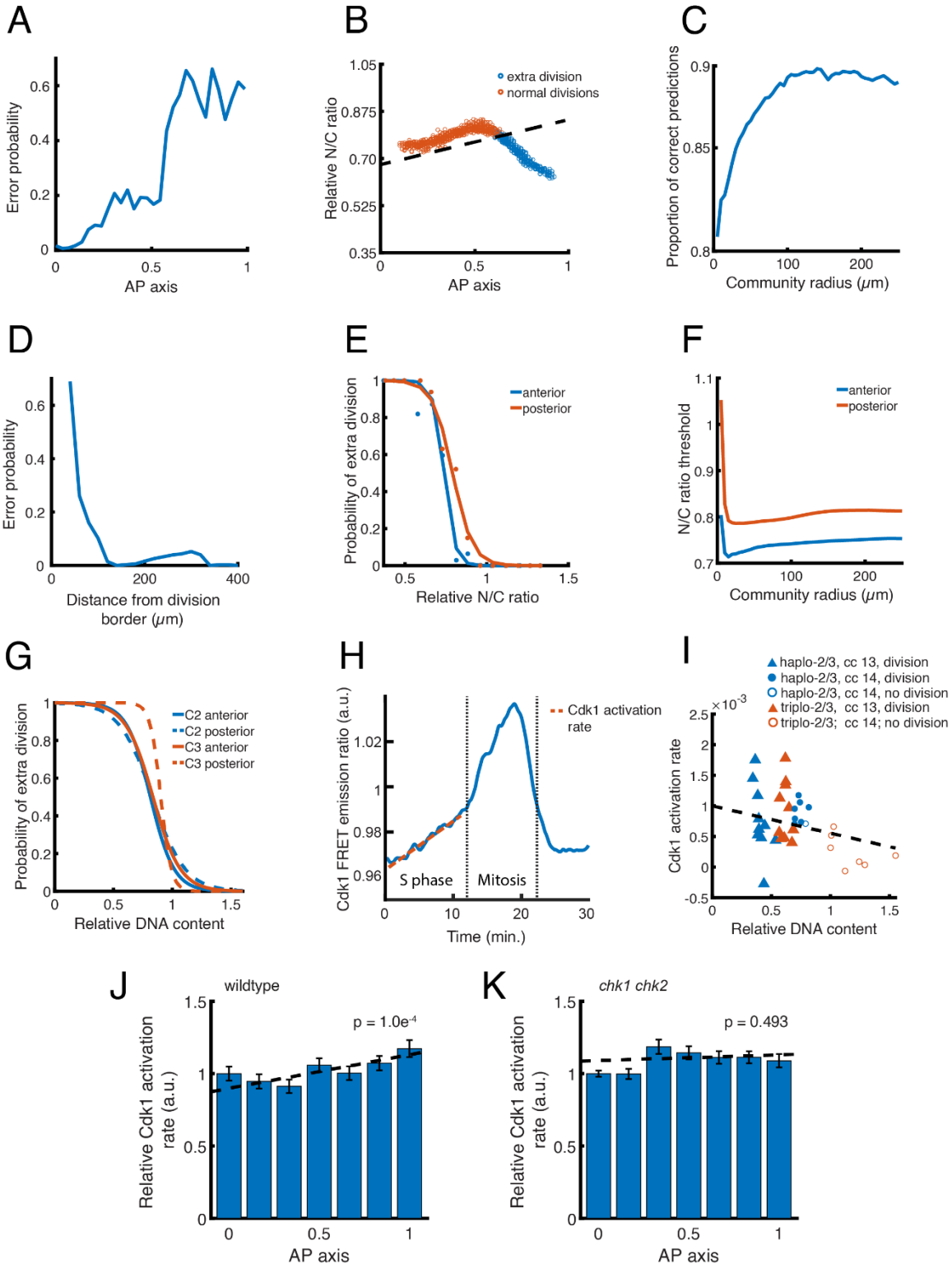
A
Error probability
AP axis
B
Relative N/C ratio
extra division
normal divisions
AP axis
C
Proportion of correct predictions
Community radius (μm)
D
Error probability
Distance from division border (μm)
E
Probability of extra division
anterior
posterior
Relative N/C ratio
F
N/C ratio threshold
anterior
posterior
Community radius (μm)
G
Probability of extra division
C2 anterior
C2 posterior
C3 anterior
C3 posterior
Relative DNA content
H
Cdk1 FRET emission ratio (a.u.)
Cdk1 activation rate
S phase
Mitosis
Time (min.)
I
haplo-2/3, cc 13, division
haplo-2/3, cc 14, division
haplo-2/3, cc 14, no division
triplo-2/3, cc 13, division
triplo-2/3; cc 14; no division
Cdk1 activation rate
Relative DNA content
J
wildtype
p = 1.0e-4
Relative Cdk1 activation rate (a.u.)
AP axis
K
chk1 chk2
p = 0.493
Relative Cdk1 activation rate (a.u.)
AP axis

Figure 15: A gradient in N/C ratio sensing across the AP axis. (A) Errors made by the simple threshold model as a function of position across the AP axis. (B) The N/C ratio in local neighborhoods of 70μm (the maximum of the correct predictions of the simple threshold model) across the AP axis during cc 14. Dashed line shows that an N/C ratio threshold with a slight gradient across the AP axis does a much better job at dividing the normal and extra division regions. (C) This gradient threshold model predicts the division behavior correctly upwards of 90% of the time at a community radius of ~100μm. (D) Errors in prediction from the gradient threshold model are largely near the border between normal and extra division regions. (E) Probability of a region undergoing an extra division as a function of N/C ratio in the anterior third versus posterior third of the embryo at a community radius of 100μm. The posterior curve is shifted towards a higher N/C ratio. (F) The N/C ratio threshold in the anterior and posterior of the embryo at different community radii. (G) Probability of a region undergoing an extra division as a function of N/C ratio at a community radius of 100μm, performed in embryos with either one additional or one fewer copy of either chromosome two or three. These embryos have altered DNA content but normal nuclear spreading. (H) Diagram showing an oscillation of Cdk1/PP1 FRET ratio during cc 13. The dashed red line indicates a linear fit of the slope of the ratio during S phase which we use as the Cdk1 activation rate. (I) Correlation between Cdk1 activation rate and division behavior in normal and extra division regions in compound chromosome embryos. At low DNA content and high Cdk1 activation rate, nuclei tend to divide. Dashed line: linear fit. (J, K) Cdk1 activation rate across the AP axis (relative to the anterior of the embryo) in wildtype (J) and chk1 chk2 (K) mutants. Dashed lines indicate linear fit and p values (F-test) for the significance of the slope are shown. Data are represented as mean ± SEM.

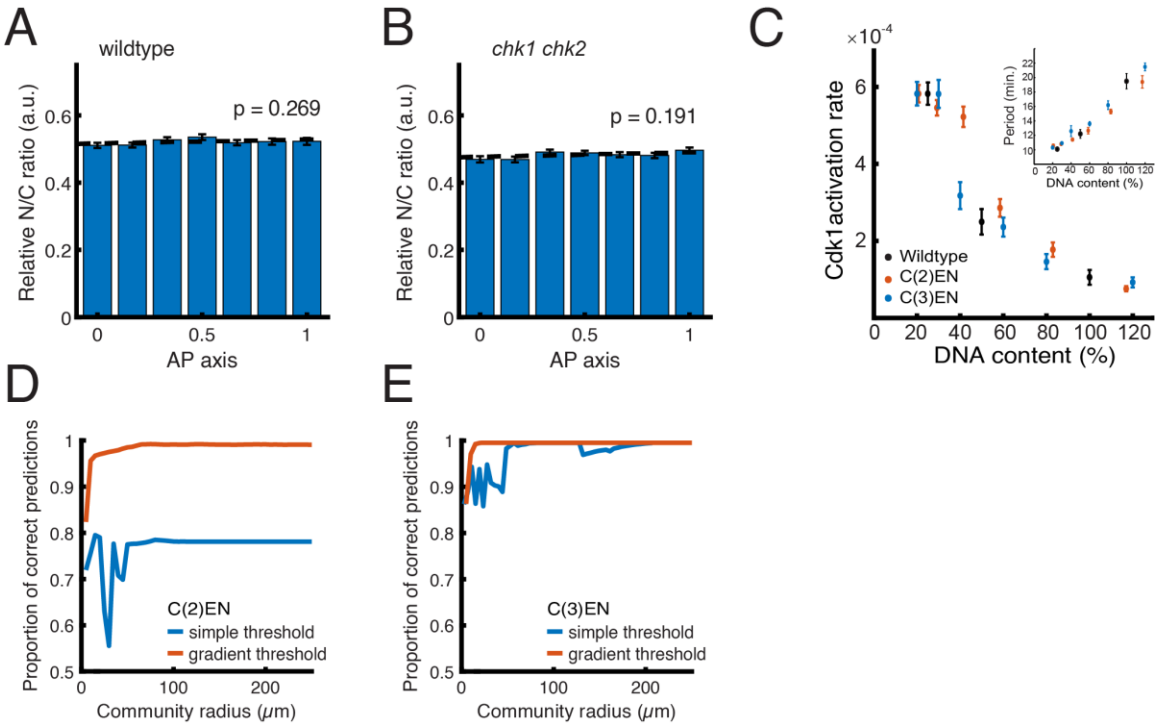

Figure 16: Nuclear density across the AP axis. (A, B) N/C ratio (relative to the embryo's anterior) across the AP axis in wildtype (A) and chk1 chk2 (B) embryos. P-values (F-test) for the significance of the slope are shown and indicate a uniform nuclear density across the AP axis for both genotypes. (C) Cdk1 activation rate and period of cc 13 as a function of DNA content; adapted from10. (D, E) Proportion of correct predictions from the simple and gradient threshold models in C(2)EN (D) and C(3)EN (E) embryos.

3.3 Discussion

The tight control of the cell cycle and nuclear (cell) positioning and number is a ubiquitous feature of metazoan development and is crucial to the proper development of early embryos. In this work we have taken advantage of *shkl* mutants which have defects in nuclear spreading to identify a novel pathway involved in the control of cortical contractility and gain insights into how nuclei respond to changes in the N/C

ratio. Through DNA sequencing and complementation tests, we have identified *shkl* mutants as mutations of the ubiquitin ligase Cul-5.

In the early embryo, Cul-5 does not regulate the cell cycle oscillator but is required for Rho and myosin activity. Cul-5 restricts the levels of active Src kinase[98-100], which is a known regulator of the actomyosin cytoskeleton. Indeed, we found that the cullin-5 phenotype could be largely rescued through a genetic reduction in Src activity and recapitulated through Src overexpression, indicating that a main function of Cul-5 is to downregulate Src activity. These results implicate the Cul-5/Src axis as a crucial pathway involved in the control of cortical contractility in early *Drosophila* embryos. In the early embryo, nuclei regulate their own positioning through PP1 activity which spreads from the nuclei to the cortex.[5] This localized PP1 activity drives activation of Rho and Myosin II accumulation in turn.[5] Our results argue that Cul-5 and Src act in a pathway downstream or parallel to the cell cycle to regulate Rho activity. The molecular mechanisms by which Cul-5 and Src control Rho remain to be elucidated, as is the possible connection between the cell cycle oscillator and Cul-5/Src activities. Since Src has been shown to regulate Rho GTPases in several contexts[117-119], these mechanisms are natural candidates for the regulation of cortical actomyosin regulation via the Cul-5/Src pathway.

Control of the MBT by the N/C ratio is important in several species, including *Drosophila* and *Xenopus*[36-38,40,109,120] but likely excluding zebrafish.[121-124] This density of

DNA (as well as nuclear size[125,126]) can directly or indirectly impact multiple aspects of the MBT, namely zygotic gene expression[110,123,127-129] and cell cycle control.[36,41,109,111,130] Previous experiments with embryos irradiated to generate different nuclear densities across the AP axis argued that nuclear cycles and zygotic activation of a large set of genes respond to the local N/C ratio.[110] Here, we have exploited the changes in nuclear positioning in *shkl* embryos to generate a continuous range of nuclear densities. This property allowed us to gain insights into how the decision of nuclei to pause their cell cycles at the MBT is affected by the N/C ratio. We found that the threshold for nuclear division is about 70% of the density at nuclear cycle 14, which confirms previous results.[39] This value—about 250 halfway between the density at cycle 13 and 14—likely contributes to the robustness of the MBT. However, it is not sufficient for the robustness of the MBT. To ensure reliable lengthening of cycle 14 in all nuclei, the sensing of the N/C ratio must be averaged over hundreds of nuclei. Consistently, our results suggest that nuclei sense the local N/C ratio in neighborhoods of ~100μm. This length essentially coincides with the correlation length of the Cdk1 activity field, which is established via reaction-diffusion mechanisms.[43] Additionally, we found that a model based on uniform sensing of the N/C ratio fails to predict the behavior of a large fraction of nuclei. However, a model assuming a slightly higher N/C ratio threshold in the posterior is highly predictable and mainly misses the behavior of nuclei at the interface between the region of extra division and that of normal division. Thus, we propose that the N/C ratio

is the major regulator of the cell cycle at the MBT and that no mechanism other than a slight spatial modulation of the N/C threshold is needed to account for nuclear behaviors. This spatial modulation likely reflects the fact that the rate of Cdk1 activation is also slightly graded across the AP axis. The Cdk1 activation gradient is dependent on the DNA replication checkpoint, which argues that the gradient might be controlled by an asymmetric distribution of factors controlling DNA replication and/or Chk1 activity.[131-133] Alternatively, the DNA replication checkpoint and Cdk1 activity might be influenced by factors controlling AP patterning and expressed in gradients across the embryos.[134,135] In the future, it will be interesting to understand the mechanisms and possible functional significance of this gradient.

The precise coordination of biochemical and mechanical signals is a ubiquitous feature of embryonic development. In early Drosophila embryogenesis, it is necessary for the uniform positioning of nuclei and timing of the MBT. Our work has identified a new pathway wherein Cul-5 regulates cortical contractility by restricting Src activity. Our results investigating embryos with patchy divisions indicate that nuclei sense the N/C ratio in neighborhoods of ~100μm and pause the cell cycle when the local density exceeds a threshold around 70% of the normal density at the MBT. Moreover, the threshold required to arrest the cell cycle is slightly graded across the AP axis and is coupled to the spatiotemporal dynamics of Cdk1. Quantitatively measuring biochemical

and physical dynamics during specific morphogenic events will undoubtedly continue to reveal new insights into the mechanisms and regulations of these pathways.

3.4 Acknowledgements

I thank the Bloomington Drosophila Stock Center, the Kyoto Drosophila Stock Center, Ruth 281 Lehmann, Denise Montell and Alana O'Reilly for providing stocks. I thank the Drosophila Genomics Resource Center for constructs. I thank members of the Di Talia lab for comments on the manuscript. This work was supported by a Schlumberger Faculty for the Future Fellowship and an HHMI International Student Research Fellowship to V.D., Associazione Italiana Ricerca sul Cancro (AIRC) MFAG-2020 n. 25040 to A.P.; University of Torino Fondo Ricerca Locale 2019 and 2020 PULA_RILO_19_01 and PULA_RILO_2020 to A.P., and NIH (R01-GM122936 and R01-GM136763) to S.D.

3.5 Author contributions

Conceptualization, L.H., A.C., V.E.D., M.V., and S.D.; Methodology, L.H., A.C., V.E.D., M.V., A.P., and S.D.; Software, L.H., A.P., and S.D.; Investigation, L.H., A.C., V.E.D., A.P., and S.D.; Writing – Original Draft, L.H. and S.D.; Supervision, A.C and S.D. Funding Acquisition, S.D.

3.6 Materials and methods

Table 2: Key resources used in this chapter

REAGENT or RESOURCE	SOURCE	IDENTIFIER
Chemicals, peptides, and recombinant proteins		
Halocarbon Oil 27	Sigma	Cat # 9002-83-9
Aqua-Poly/Mount	Polysciences, Inc.	Cat # 18606
Deposited data		
Shkl genomic sequencing data	This paper	ID: PRJNA799361
Experimental models: Organisms/strains		
D. melanogaster: w; Cdk1-FRET; His2Av-mRFP	S. Di Talia[84]	N/A
D. melanogaster: w; AniRBD-GFP	T. Lecuit[95]	N/A
D. melanogaster: w[*];; P{w[+mC]=sqh-mCherry.M}3	Bloomington Drosophila Stock Center	BDSC: 59024; FlyBase: FBst0059024
D. melanogaster: w;; PCNA-TagRFP-T	S. Di Talia[84]	N/A
D. melanogaster: w;; shkl^{GM130}/TM3	R. Lehmann[90]	N/A
D. melanogaster: w;; shkl^{GM163}/TM3	R. Lehmann[90]	N/A
D. melanogaster: w[1118]	S. Di Talia	Duke University
D. melanogaster: w[1118];; P{w[+mC]=GAL4::VP16-nos.UTR}CG6325[MVD1]	Bloomington Drosophila Stock Center	BDSC: 4937; FlyBasee: FBst0004937
D. melanogaster: w; grp^{209} lok^{30}/grp^{z5170} lok^{30}	J. Sekelsky	N/A
D. melanogaster: w[1118]; P{w[+mC]=UAS-Src42A.CA}5	Bloomington Drosophila Stock Center	BDSC: 6410; FlyBase: FBst0006410
D. melanogaster: w[*]; P{w[+mC]=UAS-Src64B.C}2	Bloomington Drosophila Stock Center	BDSC: 8477; FlyBase: FBst0008477
D. melanogaster: w[*]; TI{w[+mW.hs]=TI}Src64B[ko] P{w[+mW.hs]=FRT(w[hs])}2A/TM6B, Tb[1]	Bloomington Drosophila Stock Center	BDSC: 81022; FlyBase: FBst0081022
D. melanogaster:w; twe > Cul5	This study	N/A
D. melanogaster: y[1] w[67c23]; P{y[+mDint2] w[+mC]=EPgy2}Cul5[EY21463]	Bloomington Drosophila Stock Center	BDSC: 22482; FlyBase: FBst0022482
D. melanogaster: C(2)EN	Bloomington Drosophila Stock Center	BDSC: 2974; FlyBase: FBab0000106
D. melanogaster: C(2)EN, b[1] pr[1]	Bloomington Drosophila Stock Center	BDSC: 1112; FlyBase: FBab0000106

D. melanogaster: C(3)EN, st[1] cu[1] e[s]	Bloomington Drosophila Stock Center	BDSC: 1117; FlyBase: FBab0000131
Software and algorithms		
MATLAB R2020a	Mathworks	N/A

3.6.1 Resource availability

3.6.1.1 Lead contact

Further information and requests for resources and reagents related to this chapter should be directed to and will be fulfilled by the lead contact, Stefano Di Talia (stefano.ditalia@duke.edu).

3.6.1.2 Materials availability

Newly generated fly lines in this study have not been deposited to a central repository but are available without restriction from the lead contact.

3.6.1.3 Data and code availability

Genomic sequencing data have been deposited at NCBI Sequence Read Archive and are publicly available as of the date of publication. The accession number is listed in the key resources table All other data reported in this paper will be shared by the lead contact upon request.

All original code has been deposited at Github at the following link and is publicly available as of the date of publication:

https://github.com/lhaydene26/Hayden_NCratio2022

Any additional information required to reanalyze the data reported in this paper is available from the lead contact upon request.

3.6.2 Experimental model and subject details

3.6.2.1 Fly lines and husbandry

For all experiments, adult male and female flies of Drosophila melanogaster were raised at room temperature (~22°C) on standard molasses food without light/dark cycle. Prior to embryo collection, adult flies were moved to a 25°C incubator without light/dark cycle for a minimum of 2 days. Embryos were collected on apple juice agar plates with yeast paste from containers containing both male and female flies. Experiments in this study used embryos from ~cc 4 to cc 14/15 at the MBT at ~2h of age, determined by examining nuclear numbers and movement. The fly lines used or generated in this study are described in Table 2.

3.6.3 Method details

3.6.3.1 Transgenic line construction

To construct the Cul-5 rescue line, cDNA for Cul-5 (FI20194) was obtained from the Drosophila Genomics Resource Center and cloned in plasmid pBabr containing the twe promotor and 3'UTR.[93] Transgenic flies were generated by phiC31 integrase-mediated transformation onto the second chromosome (attP40).

3.6.3.2 Genomic sequencing

DNA isolation was performed using Qiagen DNeasy Blood and Tissue kit. 50 adult $shkl^{GM163}/shkl^{GM130}$ flies were used. Isolated DNA at a concentration of > 20ng/μL was sent to BGI Genomics for sequencing. Sequencing was performed using the Hiseq 4000 experimental platform with read lengths of 150PE. Standard bioinformatics procedures were used to generate alignments, assemblies, and SNP calling.

3.6.3.3 Embryo processing

For live imaging experiments, after collection, embryos were dechorionated with 50% bleach for 1 minute, rinsed twice with water, placed in halocarbon oil on a gas-permeable membrane, and covered with a glass coverslip.

For fixed embryo experiments, after collection, embryos were dechorionated with 50% bleach for 1 minute, rinsed with water, placed in a fixation solution (8mL nuclease-free water, 1mL 10x PBS, 1mL 37% formaldehyde, and 10mL heptane) in a scintillation vial, and shaken for 20 minutes. The bottom aqueous phase was then removed, 10mL methanol was added, and the vial was shaken forcefully for 30 seconds to remove the vitelline membrane. Embryos were then removed with a pipette from the methanol layer. Embryos were then washed three times with methanol and stored at -20°C in a microcentrifuge tube for < 3 days before staining. Fixed embryos were blocked with 1% BSA/0.1% Tween in PBS three times for 10 minutes each and stained with DAPI at 1μg/mL for 20 minutes. Stained embryos were rinsed twice for 15 minutes in a 1%

BSA/0.1% Tween PBS solution followed by a 15-minute rinse in a 0.1% Tween PBS solution. Embryos were mounted on slides with Aquapolymount, covered with glass cover slides, and stored at 4°C.

3.6.3.4 Microscopy

Images were acquired through confocal microcopy using a Leica SP8 confocal microscope and its software, Leica Application Suite X, using a 20x/0.75 numerical aperture air objective, an argon ion laser and either a 405nm diode laser (for DAPI stained embryos) or a 561nm diode laser (for live imaged embryos).

For imaging cytoplasmic flows, z-stack images (800 x 300 pixels, pixel size 0.73μm) were acquired in ~10μm steps from the cortex to the center of the embryo with a frame rate of 1/7.14s. For imaging the FRET and Rho sensors as well as myosin accumulation, images (800 x 300 pixels, pixel size 0.56μm) were acquired at the cortex of the embryo with a frame rate of ~1/4s. For fixed embryo experiments, single images (800 x 300 pixels, pixel size 0.97) were acquired near the center of the embryo to visualize DAPI stained nuclei. Embryos were screened for current cell cycle at the time of imaging by counting the number of nuclei in the embryo, and only those embryos fixed during cc 6 were imaged.

3.6.4 Quantification and statistical analysis

3.6.4.1 Image analysis

All image analysis steps were performed using custom-written MATLAB algorithms unless otherwise noted. Confocal images were exported as .tif files from LAS AF software for use in MATLAB algorithms.

3.6.4.2 Quantification of nuclear spreading

Following image acquisition of fixed and DAPI stained embryos, individual nuclei were manually segmented. The convex hull of the set of nuclei was calculated from which the length of the nuclear cloud was obtained. The ratio of this length to the length of the entire embryo became the metric for the degree of nuclear spreading in an embryo. This analysis was performed with all genotypes listed and the nonparametric Kolmogorov–Smirnov statistical test was used to compare the distributions of nuclear spreading.

3.6.4.3 Quantification of cytoplasmic flows and PIV

Following image acquisition of z-stack timeseries, the ~4 z-slices (a vertical distance of ~30μm) towards the center of the embryo were isolated, and a maximum projection of the data was performed. This yielded a timeseries with one image channel with stained yolk (to calculate cytoplasmic flows) and one image channel with PCNA-TagRFP (to calculate nuclear movement). To further smooth the data to be used in particle image velocimetry and to ensure nuclei had moved between each time point,

each image in the time series was averaged with its temporal neighbors. One thousand random points were distributed across the embryo which became the initial points for PIV (for PIV using the nuclei, the centroids of the nuclei became the initial points). For each time point, the correlation between the fluorescence in a 35 x 35px square around each point and neighboring regions in the next time point was calculated, and the location of the highest correlation yielded the trajectory of the cytoplasm or nuclei for each time point. To generate heatmaps of the cytoplasmic flows for visualization, the trajectories were discretized across the AP axis in 8-pixel wide bins for each time point. This data set was then smoothed using a Savitzky– Golay filter with a 3rd degree polynomial over 45 time points for visualization.

3.6.4.4 Quantification of the N/C ratio

To quantify the N/C ratio in neighborhoods of different sizes, we discretized embryos containing His-RFP with grid points every 10px (5.6μm) to give 2400 (80 x 30) grid points in the 800 x 300px image domain. Grid points outside the embryo were discarded. We selected the frame either ~5 minutes before a mitotic division began (when all nuclei were immobile following the previous mitotic division) or ~ 5 minutes after the embryo had halted at the MBT (as defined by no mitotic events for >~20 minutes at cc 14). At that time point, the nuclei were segmented using MATLAB's adaptive thresholding function adaptthresh with a sensitivity of 0.35, and a mask of the entire embryo was generated manually. Regions of the embryo where nuclear

segmentation was poor (due to being slightly out of focus for example) were discarded. The N/C ratio was then calculated as the number of nuclei within a value for the community radius divided by the area of embryo within that same distance. We then normalized that value by the embryo-wide average N/C ratio at cc 14 in normally dividing embryos.

3.6.4.5 N/C ratio threshold models

After calculating the N/C ratio in a region and scoring whether that region had divided, we tested different models to determine their ability to predict division behavior. We used a training data set consisting of 33 embryos, 15 in which the entire embryo divided, 12 of which none of the embryo divided, and 6 of which only part of the embryo divided to fit parameters in these models and a test data set of 6 embryos in which only part of the embryo divided to determine predictive ability.

For a simple threshold model, we fit the N/C ratio and division behavior data to a logistic curve and used the N/C ratio value at which the curve crossed 50% as the single parameter in the model, P_1. This model predicted that if a region had a local N/C ratio below that threshold value, it should undergo a mitotic division. We then considered whether adding some variance in the threshold between embryo would yield a better model. For this model we varied the threshold for each embryo individually and chose the best threshold in the range $P_1/(1+a)$ to $P_1*(1+a)$ where a takes the value of 0, 0.05, 0.1, 0.2, and 1 in Figure 14G.

We next considered a model with a global threshold which decreases with time, starting when the first nucleus divides (Figure 14H). This model might reflect the fact that Cdc25 is degraded at the MBT, in principle reducing the likelihood of nuclei dividing after some time and increasing the likelihood of generating embryos with a portion undergoing an extra division. This model contained two parameters which were fit to the training data consisting of the initial N/C ratio threshold at time = 0 (tested uniformly between 0 and ~1.15) and the rate of threshold decrease with time (tested uniformly between 0 and ~0.4), both parameters relative to the average N/C ratio at cc 14 in normally dividing embryos.

We finally tested a model with a threshold which had some slight gradient across the AP axis. This model contained two parameters, where the threshold T at a certain point x across the AP axis is given as $T = mx + b$. In Figure 14I, the parameters are fit to the training data set. By allowing both parameters to vary slightly between embryos, a much better prediction could be made (Figure 15C). Specifically, m is constrained such that the threshold at the posterior is no more than 10% higher than the threshold at the anterior.

3.6.4.6 Compound chromosome embryo analysis

To generate embryos with altered DNA content, we first used the C(2)EN^{+} stock which is known to give very few embryos with three copies of chromosome 2 (triplo-2, about 1%).[136] Using this stock, we could be confident of the cell cycle timing of embryos

with only one copy of chromosome 2 (haplo-2). We found that these embryos had consistently faster cell cycles 12 and 13 than wild type. Next, we repeated the experiments with C(2)EN$^{b\ pr}$ which is expected to have a significant fraction of triplo-2 embryos (roughly 40%).[136] We observed about 40% of embryos which had longer cell cycles 12 and 13 and never did an extra division.[84] Thus, we have assumed that those embryos are triplo-2. While the same approach could not be performed with the C(3)EN stocks, as they both give haplo-3 and triplo-3, we naturally extended the reasoning for chromosome 2 and found that the duration of cell cycle 12 and 13 could be easily clustered into two separate groups which we interpreted as haplo and triplo-3 (Figure 16). These stocks giving roughly equal numbers of haplo-2/3 and triplo-2/3 were used for experiments.

3.6.4.7 Quantification of biosensors and Cdk1 activation rates

Fluorescence intensity of Rho and myosin images were averaged across the embryo cortex in each time frame. Cdk1 FRET curves were computed by taking the fluorescence intensity ratio of YFP signal over CFP signal (the emission ratio). To correct for slight out-of-focus shifting and embryo drift, the data were normalized and detrended as in previous work.[5] This signal was averaged over the entire embryo cortex in Figure 15I and in rectangles of width 22.4μm across the AP axis in Figure 11. To determine whether there was a difference in Cdk1 activation rates across the AP axis (Figure 15J, K), the emission ratio was averaged in neighborhoods of 40μm in a grid

divided evenly across the embryo. S phase Cdk1 activation rates were computed by fitting a straight line through the first ~5 min of Cdk1 activity increase after the last mitotic division finished at the beginning of cc 14 (Figure 15I) or at mitosis of cc 13 (Figure 15J, K). The F test was used to compare Cdk1 activation rates across the AP axis to test the significance of a non-zero slope term over the naive model with only the intercept parameter.

3.6.4.8 Mathematical modeling

We modified a mathematical model of Cdk1 activity[43] to introduce a gradient of N/C ratio across the AP axis. The model reads:

$$\frac{\partial a(x,t)}{\partial t} = D\nabla^2 a(x,t) + G(a,t) + \eta(x,t)$$

where

$$G(a,t) = G_0[\alpha + r_+(a)(c(t) - a) - r_-(a)a]$$

and

$$r_+(a) = \left(c_0 + c_1 \frac{a^n}{K_{Cdc25}^n + a^n}\right)\left(1 - h_0(x)\frac{K_{Chk1}^s}{K_{Chk1}^s + a^s}\right)\left(\frac{1}{1 + \left(\frac{t}{t_0}\right)^5}\right)$$

$$r_-(a) = h_0(x)\left(w_0 + w_1 \frac{K_{Wee1}^n}{K_{Wee1}^n + a^n}\frac{K_{Chk1}^s}{K_{Chk1}^s + a^s}\right)$$

The quantity $c(t) = \alpha t$ denotes the total amount of Cyclin-Cdk1 complexes, so that the difference $c(t) - a(x,t)$ reflects the amount of inactive Cdk1. The first term in $r_+(a)$ describes the positive feedback between Cdk1 and Cdc25, the second term the negative regulation of Cdc25 by Chk1 and the negative feedback of Cdk1 on Chk1, the third, time-dependent term models the degradation of Cdc25 at cycle 14 which is required for cell cycle lengthening at cycle 14.[41,137] The $r_-(a)$ describes the double negative feedback between Cdk1 and Wee1, the modulation of Wee1 activity by Chk1 and the negative feedback of Cdk1 on Chk1. Note that our model focuses on the activation of Cdk1 and does not explicitly model its inactivation at the exit from mitosis. The rationale is that we have previously shown that the exit from mitosis is controlled by a phase wave that reflects the delays set by the earlier Cdk1 wave, which times the entry into mitosis.[84] The noise term is a Langevin, Gaussian noise with short spatiotemporal correlations:

$$\langle \eta(x,t)\eta(x',t')\rangle = \sigma^2 G_0[\alpha + r_+(a)(c(t)-a) - r_-(a)a]\delta(x-x')\delta(t-t')$$

A gradient of N/C ratio was introduced by defining $h_0(x)$ as a piecewise linear, noisy gradient:

$$h_0(x) = \begin{cases} h_0 + h_1\left(1 - \dfrac{x}{0.7}\right) + \xi(x) \;\; for\; x < 0.7 \\ h_0 + \xi(x) \quad for\; x \geq 0.7 \end{cases}$$

where x is the normalized position along the Anterior-Posterior Axis ($x = 0$ at the Anterior pole and $x = 1$ at the Posterior pole) and $\xi(x)$ is a brown noise term ($\frac{1}{f^2}$ spectrum) with $\langle \xi(x)\rangle = 0$ and $\langle \xi^2(x)\rangle = \Gamma^2$, generated using the MATLAB function

dsp.ColoredNoise. The stochastic model was simulated using finite differences and Euler method with reflecting boundary conditions.

Table 3: Parameters of the Cdk1 activity model

Parameters	Values
D	$5\mu m^2\ s^{-1}$
K_{Chk1}	32 nM
K_{Cdc25}	26.4 nM
K_{Wee1}	26.4 nM
α	8 nM min^{-1}
c_0	0.12 min^{-1}
c_1	0.65 min^{-1}
w_0	0.24 min^{-1}
w_1	1 min^{-1}
n	5
s	10
t_0	20.3 min
σ	9 $nM^{1/2}\mu M^{1/2}$
h_0	0.65
h_1	0.15
Γ	0.05

4. Conclusion: understanding the physical properties which enable and regulate wave propagation

Thus far, I have largely discussed the discovery and characterization of waves in different cells and tissues. I conclude this work by considering future directions which may be pursued by experimentalists and theorists to further explore the construction, regulation, and physical properties of each system.

4.1 Regulation of zebrafish osteoblast regeneration by manipulation of Erk activity wave properties

Because Erk activity waves in the zebrafish scale have only recently been discovered, work to date has largely involved their discovery[10] and description.[10,11] Many details—like with the exact molecular players and regulatory pathways involved—remain to be discovered. We have shown that a simple three component model consisting of Erk, an activator, and an inhibitor is sufficient to generate successive traveling waves which propagate across a scale[10] (see Chapter 2); however, the identities of the activator(s) and inhibitors(s) *in vivo* remain unknown. Potential activator candidates include those from the fibroblast growth factor (Fgf) family as Erk activity here depends on Fgf (but not epidermal growth factor) receptor activity.[10] In the case of Erk inhibitors, we have seen enhancement of transcripts in the Spry and Dusp family of genes in Erk active cells, indicating active Erk could lead to gene expression of these inhibitors, which is compatible with the timescale of Erk inactivation.[10,11]

4.1.1 Identification of the source region

In addition to molecular identities, the construction of the source region is critical to form both the wave pattern of Erk activity and the geometric properties necessary for wave formation. Our model relies on the deposition of an extracellular, diffusible species which originates in the source region.[11] If the source region is circumnavigated in such a way that Erk activity becomes active everywhere, scale regeneration actually slows and normal morphology is perturbed.[10] These results indicate the importance of proper spatiotemporal coordination of the propagating Erk signal, enabled and maintained in the source region. Multiple possible mechanisms exist which could in principle explain the formation of successive waves in a source region through deposition of an activator molecule.

One mechanism which could explain the formation of a source region is due to collective cell behavior. In the initial ~3 days of regeneration, osteoblasts show uniformly high Erk activity.[10] Within the next day, Erk activity is globally reduced across the scale, and the system switches to a pattern of wave propagation. It is possible that when a sufficiently large number of osteoblasts, they coordinate in such a way to generate oscillations in the source region which then propagate across the scale. A similar mechanism has been observed in somitogenesis where explants from the mouse tail bud will self-organize to generate waves once a sufficient density has been achieved.[138] Thus

a sufficiently sized pool of scale osteoblasts may self-induce this change to regime of wave propagation.

A second class of mechanisms involve delivery of an activator molecule to the osteoblast in the scale. This delivery could be paracrine, neighboring dermal cells releasing activator molecules which activate the proximal scale osteoblasts, or endocrine, activator arriving through the vasculature. In support of this kind of mechanism, across all observed scales, the source region always lies off-center, towards the anterior. This region is proximally close to the dermal cells which differentiate to form the initial pool of osteoblasts in the regenerating scale as well as clusters of blood vessels (Figure 17). Various simulations of the Erk activity wave model with an irregular source region generated from these maps of blood vessels and other scale architecture yield disorganized aperiodic waves which do not agree with experimental observations (data not shown). It will be important for future experiments to distinguish between these possible mechanisms and others to fully understand the construction and regulation of the source region.

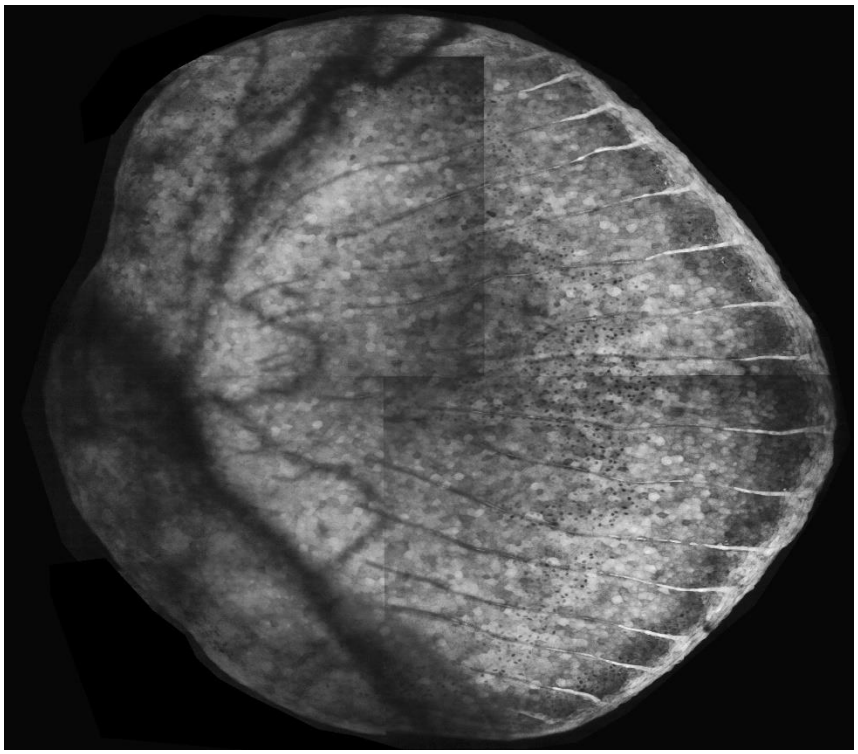

Figure 17: Blood vessels in a regenerating scale. This image of a partially regenerated scale shows partially opaque regions of the scale's anterior (left side)) where blood vessels are located. See Chapter 2 and previous work[10] for exact imaging conditions.

4.1.2 Scale regeneration in other fish species

A model of tissue regeneration controlled by successive waves which in turn controlled by the dynamics in a small, localized source could be extendable to other kinds of fish with vastly different scale sizes. Because these waves propagate stably across a tissue, regardless of size, no additional modification would be required to extend this behavior to regenerate significantly larger scales in larger fish. The target final size of a regenerating scale could be simply set by the size of the dermal pocket in which the scale sits and grows in proportion to the fish. In support of this idea, sufficient

physical damage to the dermal pocket in zebrafish can lead to larger pockets and larger regenerated scales (Ben Cox, unpublished data). Once plucked, differentiation of new osteoblasts occurs[79] followed by cell division until achieving a sufficiently large number of osteoblasts which could be set by the size of the dermal pocket. This increase in osteoblast number could then trigger the switch to hypertrophy and Erk activity waves, the frequency of which is set through activity in the source region. This mechanism of scale regeneration could be ubiquitous across many species and sizes of fish, controlled solely by the size of the dermal pocket and rate of activator deposition.

4.2 Regulation of mitotic signaling across the anterior-posterior axis in the Drosophila *embryo*

In Chapter 3, I discussed the significance of the collective decision for syncytial nuclei to pause the cell cycle at the mid-blastula transition in the *Drosophila* embryo. This synchronous decision across the embryo is made possible by a uniform nucleocytoplasmic (N/C) ratio across the anterior-posterior (AP) axis.[5] I have discussed how when the N/C ratio is instead graded across the AP axis in *shkl* mutants, the anterior (higher nuclear density) will pause the cell cycle before the posterior (lower nuclear density). Using these mutants allows us to study the transmission of the mitotic signal across the embryo, early work of which I present here.

Until this point, I have largely discussed bistable waves where a system can exist in equilibrium in two stable states, and a perturbation leading to a shift to the other stable state travels across a domain as a bistable wave. As chemical waves, their speed

offers advantages as a signaling mechanism over a simple diffusive process; however, in the *Drosophila* embryo, an even greater speed is required to maintain cell cycle synchrony. These waves, called "sweep waves" are characterized by a uniform increase of Cdk1 activity over space rather than a traveling profile of high Cdk1 activity.[43] In this way, Cdk1 activity crosses the threshold required to induce mitosis much quicker than a traveling bistable wave. In support of this idea, the gradient of N/C ratio in *shkl* embryos is sufficient to slow the sweep wave mechanism to generate the characteristic bistable propagating wave front (Figure 18). Taken together with the results of Chapter 3, these experiments indicate the importance of regulatory mechanisms on protein levels to enable and maintain synchronous behavior across the embryo. Undoubtedly future work on chemical waves and their regulation will continue to highlight their importance as an effective mechanism of signal propagation.

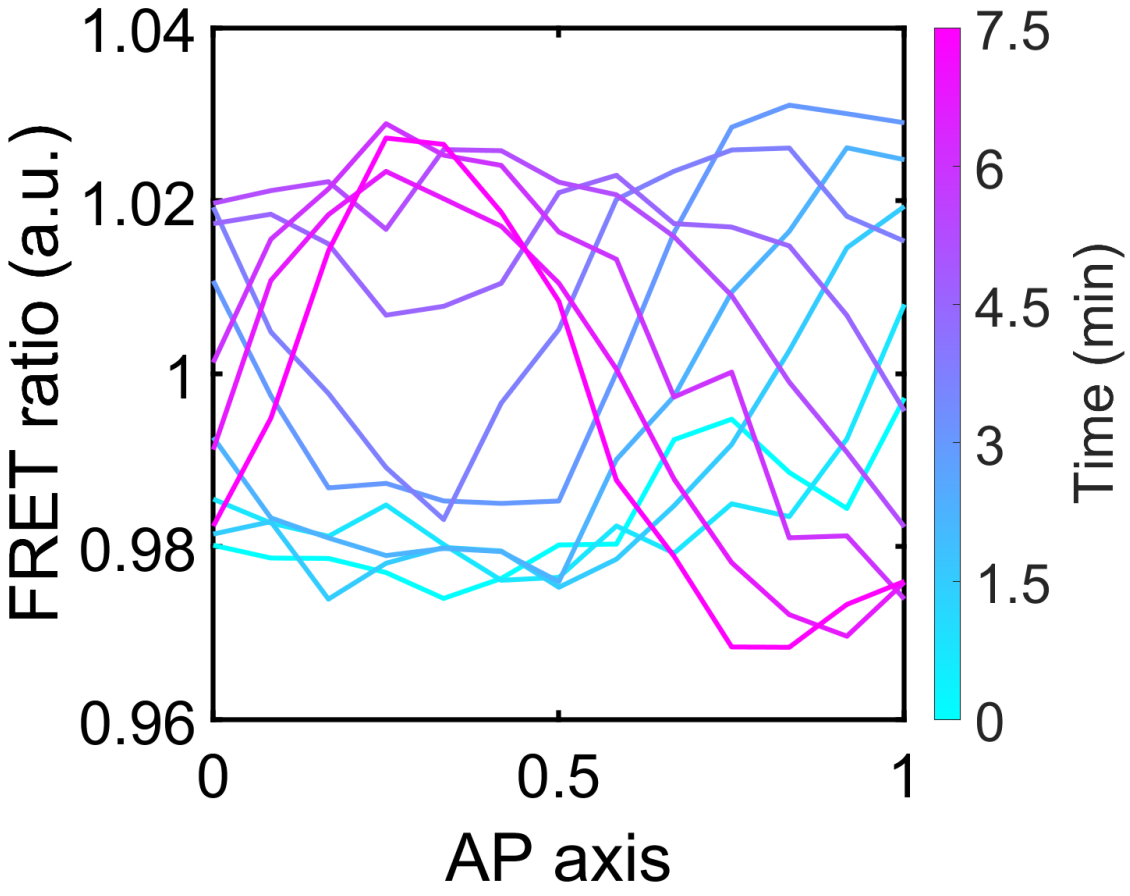

Figure 18: A bistable mitotic wave in a *shkl* embryo. Cdk1 activity initially rises in the posterior (x=1) and propagates to the anterior as a bistable wave.

4.3 Sensing the N/C ratio in Xenopus laevis

Results of Chapter 3 highlighted Cdk1 as a mechanism for coordinating the uniform entry into the MBT in *Drosophila*. Diffusion of Cdk1 across the syncytial embryo correlates with the collective decision of nuclei to pause their cell cycle prior to gastrulation. If a significant portion of the embryo performs an extra division, the initial gastrulation and formation of the mesoderm fails to occur properly, resulting in the

death of the organism. In contrast to the syncytial *Drosophila* embryo, in *Xenopus*, the early embryo develops as a collection of cells without a shared cytoplasm. It is therefore unclear whether the same mechanism of Cdk1 coordination among neighboring cells would ensure a uniform entry into the MBT. Recent work in *Xenopus* has shown that neighboring regions of the embryo can be desynchronized with respect to the mitotic program by subjecting the embryo to a gradient of temperature.[139] Neighboring cells with different cell cycle timings do not show corrective behavior leading up to the MBT, indicating that neighboring cells to not coordinating mitotic activities like in *Drosophila*. However, *Xenopus* embryos which do not enter gastrulation uniformly do not have significantly lower survival rates. Rather, embryos show a corrective behavior whereby some as-of-yet unknown mechanism serves to actively compensate for nonuniformities.[139] This striking difference from *Drosophila* development shows how different organisms regulate proper developmental times by active and passive mechanisms depending on the physical structure of the embryo.

References

1. Brown, R. (1828). On the particles contained in the pollen of plants; and on the general existence of active molecules in organic and inorganic bodies. Edinburgh New Philosophical Journal *5*, 358–371.

2. Caspi, A., Granek, R., and Elbaum, M. (2000). Enhanced Diffusion in Active Intracellular Transport. Physical Review Letters *85*, 5655-5658. 10.1103/PhysRevLett.85.5655.

3. Lau, A.W.C., Hoffman, B.D., Davies, A., Crocker, J.C., and Lubensky, T.C. (2003). Microrheology, Stress Fluctuations, and Active Behavior of Living Cells. Physical Review Letters *91*, 198101. 10.1103/PhysRevLett.91.198101.

4. Bursac, P., Lenormand, G., Fabry, B., Oliver, M., Weitz, D.A., Viasnoff, V., Butler, J.P., and Fredberg, J.J. (2005). Cytoskeletal remodelling and slow dynamics in the living cell. Nature Materials *4*, 557-561. 10.1038/nmat1404.

5. Deneke, V.E., Puliafito, A., Krueger, D., Narla, A.V., De Simone, A., Primo, L., Vergassola, M., De Renzis, S., and Di Talia, S. (2019). Self-Organized Nuclear Positioning Synchronizes the Cell Cycle in *Drosophila* Embryos. Cell *177*, 925-941.e917. 10.1016/j.cell.2019.03.007.

6. Driever, W., and Nüsslein-Volhard, C. (1988). A gradient of bicoid protein in Drosophila embryos. Cell *54*, 83-93.

7. Frohnhöfer, H.G., and Nüsslein-Volhard, C. (1986). Organization of anterior pattern in the Drosophila embryo by the maternal gene bicoid. Nature *324*, 120-125.

8. Kumar, M., Mommer, M.S., and Sourjik, V. (2010). Mobility of Cytoplasmic, Membrane, and DNA-Binding Proteins in Escherichia coli. Biophysical Journal *98*, 552-559. 10.1016/j.bpj.2009.11.002.

9. Milo, R., Jorgensen, P., Moran, U., Weber, G., and Springer, M. (2010). BioNumbers--the database of key numbers in molecular and cell biology. Nucleic Acids Res *38*, D750-D753. 10.1093/nar/gkp889.

10. De Simone, A., Evanitsky, M.N., Hayden, L., Cox, B.D., Wang, J., Tornini, V.A., Ou, J., Chao, A., Poss, K.D., and Di Talia, S. (2021). Control of osteoblast regeneration by a train of Erk activity waves. Nature. 10.1038/s41586-020-03085-8.

11. Hayden, L.D., Poss, K.D., De Simone, A., and Di Talia, S. (2021). Mathematical modeling of Erk activity waves in regenerating zebrafish scales. Biophysical Journal *120*, 4287-4297. https://doi.org/10.1016/j.bpj.2021.05.004.

12. Venero Galanternik, M., Kramer, Kenneth L., and Piotrowski, T. (2015). Heparan Sulfate Proteoglycans Regulate Fgf Signaling and Cell Polarity during Collective Cell Migration. Cell Reports *10*, 414-428. 10.1016/j.celrep.2014.12.043.

13. Fitzhugh, R. (1961). Impulses and Physiological States in Theoretical Models of Nerve Membrane. Biophysical journal *1*, 445-466. 10.1016/s0006-3495(61)86902-6.

14. Nagumo, J., Arimoto, S., and Yoshizawa, S. (1962). An Active Pulse Transmission Line Simulating Nerve Axon. Proceedings of the IRE *50*, 2061-2070. 10.1109/JRPROC.1962.288235.

15. Tyson, J.J., and Keener, J.P. (1988). Singular perturbation theory of traveling waves in excitable media (a review). Physica D: Nonlinear Phenomena *32*, 327-361. https://doi.org/10.1016/0167-2789(88)90062-0.

16. Hodgkin, A.L., and Huxley, A.F. (1952). A quantitative description of membrane current and its application to conduction and excitation in nerve. The Journal of physiology *117*, 500.

17. Reece, J.U., Lisa; Cain, Michael; Wasserman, Steven; Minorsky, Peter; Jackson, Robert. (2011). Biology, 9th Edition (Person Education).

18. Stricker, S.A. (1999). Comparative biology of calcium signaling during fertilization and egg activation in animals. Developmental biology *211*, 157-176.

19. Durston, A.J. (1973). Dictyostelium discoideum aggregation fields as excitable media. Journal of Theoretical Biology *42*, 483-504. https://doi.org/10.1016/0022-5193(73)90242-7.

20. Carey, A.B., Giles, R.H., and McLean, R.G. (1978). The Landscape Epidemiology of Rabies in Virginia. The American Journal of Tropical Medicine and Hygiene *27*, 573-580. 10.4269/ajtmh.1978.27.573.

21. Fisher, R.A. (1937). The wave of advance of advantageous genes. Annals of Eugenics *7*, 355-369. https://doi.org/10.1111/j.1469-1809.1937.tb02153.x.

22. Turing, A.M. (1952). The chemical basis of morphogenesis. Philosophical Transactions of the Royal Society of London. Series B, Biological Sciences *237*, 37-72. doi:10.1098/rstb.1952.0012.

23. Stauffer, D., Stanley, H.E., and Lesne, A. (2017). Dynamical Systems and Chaos. In From Newton to Mandelbrot: A Primer in Theoretical Physics, D. Stauffer, H.E. Stanley, and A. Lesne, eds. (Springer Berlin Heidelberg), pp. 215-251. 10.1007/978-3-662-53685-8_6.

24. Lavoie, H., Gagnon, J., and Therrien, M. (2020). ERK signalling: a master regulator of cell behaviour, life and fate. Nature Reviews Molecular Cell Biology *21*, 607-632. 10.1038/s41580-020-0255-7.

25. Cargnello, M., and Roux, P.P. (2011). Activation and Function of the MAPKs and Their Substrates, the MAPK-Activated Protein Kinases. Microbiology and Molecular Biology Reviews *75*, 50-83. doi:10.1128/MMBR.00031-10.

26. Cooper, J.A., Bowen-Pope, D.F., Raines, E., Ross, R., and Hunter, T. (1982). Similar effects of platelet-derived growth factor and epidermal growth factor on the phosphorylation of tyrosine in cellular proteins. Cell *31*, 263-273. https://doi.org/10.1016/0092-8674(82)90426-3.

27. Kazlauskas, A., and Cooper, J.A. (1988). Protein kinase C mediates platelet-derived growth factor-induced tyrosine phosphorylation of p42. The Journal of cell biology *106*, 1395-1402. 10.1083/jcb.106.4.1395.

28. Aman, A.J., Fulbright, A.N., and Parichy, D.M. (2018). Wnt/β-catenin regulates an ancient signaling network during zebrafish scale development. Elife *7*, e37001.

29. Meloche, S., and Pouysségur, J. (2007). The ERK1/2 mitogen-activated protein kinase pathway as a master regulator of the G1- to S-phase transition. Oncogene *26*, 3227-3239. 10.1038/sj.onc.1210414.

30. Shaulian, E., and Karin, M. (2001). AP-1 in cell proliferation and survival. Oncogene *20*, 2390-2400. 10.1038/sj.onc.1204383.

31. Samarage, Chaminda R., White, Melanie D., Álvarez, Yanina D., Fierro-González, Juan C., Henon, Y., Jesudason, Edwin C., Bissiere, S., Fouras, A., and Plachta, N. (2015). Cortical Tension Allocates the First Inner Cells of the Mammalian Embryo. Developmental Cell *34*, 435-447. https://doi.org/10.1016/j.devcel.2015.07.004.

32. Gross, P., Kumar, K.V., and Grill, S.W. (2017). How Active Mechanics and Regulatory Biochemistry Combine to Form Patterns in Development. Annual Review of Biophysics *46*, 337-356. 10.1146/annurev-biophys-070816-033602.

33. Gilmour, D., Rembold, M., and Leptin, M. (2017). From morphogen to morphogenesis and back. Nature *541*, 311-320. 10.1038/nature21348.

34. Rabinowitz, M. (1941). Studies on the cytology and early embryology of the egg of Drosophila melanogaster. Journal of Morphology *69*, 1-49.

35. Huang, J., and Raff, J.W. (1999). The disappearance of cyclin B at the end of mitosis is regulated spatially in Drosophila cells. The EMBO journal *18*, 2184-2195. 10.1093/emboj/18.8.2184.

36. Newport, J., and Kirschner, M. (1982). A major developmental transition in early xenopus embryos: I. characterization and timing of cellular changes at the midblastula stage. Cell *30*, 675-686. 10.1016/0092-8674(82)90272-0.

37. Newport, J., and Kirschner, M. (1982). A major developmental transition in early xenopus embryos: II. control of the onset of transcription. Cell *30*, 687-696. 10.1016/0092-8674(82)90273-2.

38. Edgar, B.A., and Schubiger, G. (1986). Parameters controlling transcriptional activation during early drosophila development. Cell *44*, 871-877. 10.1016/0092-8674(86)90009-7.

39. Lu, X., Drocco, J., and Wieschaus, E.F. (2010). Cell cycle regulation via inter-nuclear communication during the early embryonic development of Drosophila melanogaster. Cell Cycle *9*, 2908-2910. 10.4161/cc.9.14.12346.

40. Lu, X., Li, J.M., Elemento, O., Tavazoie, S., and Wieschaus, E.F. (2009). Coupling of zygotic transcription to mitotic control at the Drosophila mid-blastula transition. Development *136*, 2101-2110. 10.1242/dev.034421.

41. Farrell, J.A., and O'Farrell, P.H. (2014). From Egg to Gastrula: How the Cell Cycle Is Remodeled During the Drosophila Mid-Blastula Transition. Annual Review of Genetics *48*, 269-294. 10.1146/annurev-genet-111212-133531.

42. Amodeo, A.A., Jukam, D., Straight, A.F., and Skotheim, J.M. (2015). Histone titration against the genome sets the DNA-to-cytoplasm threshold for the Xenopus midblastula transition. Proceedings of the National Academy of Sciences *112*, E1086-E1095. 10.1073/pnas.1413990112.

43. Vergassola, M., Deneke, V.E., and Di Talia, S. (2018). Mitotic waves in the early embryogenesis of Drosophila: Bistability traded for speed. Proceedings of the National Academy of Sciences *115*, E2165-E2174. 10.1073/pnas.1714873115.

44. Briscoe, J., and Small, S. (2015). Morphogen rules: design principles of gradient-mediated embryo patterning. Development *142*, 3996-4009. 10.1242/dev.129452 %J Development.

45. Kicheva, A., Bollenbach, T., Wartlick, O., Jülicher, F., and Gonzalez-Gaitan, M. (2012). Investigating the principles of morphogen gradient formation: from tissues to cells. Current Opinion in Genetics & Development *22*, 527-532. https://doi.org/10.1016/j.gde.2012.08.004.

46. Rogers, K.W., and Schier, A.F. (2011). Morphogen Gradients: From Generation to Interpretation. Annual Review of Cell and Developmental Biology *27*, 377-407. 10.1146/annurev-cellbio-092910-154148.

47. Bollenbach, T., Pantazis, P., Kicheva, A., Bökel, C., González-Gaitán, M., and Jülicher, F. (2008). Precision of the Dpp gradient. Development *135*, 1137-1146. 10.1242/dev.012062 %J Development.

48. Sagner, A., and Briscoe, J. (2017). Morphogen interpretation: concentration, time, competence, and signaling dynamics. Wiley Interdiscip Rev Dev Biol *6*, e271. https://doi.org/10.1002/wdev.271.

49. Berezhkovskii, A.M., Sample, C., and Shvartsman, S.Y. (2010). How long does it take to establish a morphogen gradient? Biophysical journal *99*, L59-L61. 10.1016/j.bpj.2010.07.045.

50. Müller, P., Rogers, K.W., Yu, S.R., Brand, M., and Schier, A.F. (2013). Morphogen transport. Development *140*, 1621-1638. 10.1242/dev.083519 %J Development.

51. Gonzalez-Mendez, L., Gradilla, A.C., and Guerrero, I. (2019). The cytoneme connection: direct long-distance signal transfer during development. Development *146*. 10.1242/dev.174607.

52. Kornberg, T.B., and Roy, S. (2014). Cytonemes as specialized signaling filopodia. Development *141*, 729. 10.1242/dev.086223.

53. Ben-Jacob, E., Brand, H., Dee, G., Kramer, L., and Langer, J.J.P.D.N.P. (1985). Pattern propagation in nonlinear dissipative systems. Physica D: Nonlinear Phenomena *14*, 348-364.

54. Murray, J.D. (2002). Mathematical Biology (Springer).

55. Saarloos, W.v. (1998). Three basic issues concerning interface dynamics in nonequilibrium pattern formation. Physics Reports *301*, 9-43. https://doi.org/10.1016/S0370-1573(98)00004-0.

56. Deneke, V.E., and Di Talia, S. (2018). Chemical waves in cell and developmental biology. Journal of Cell Biology *217*, 1193-1204. 10.1083/jcb.201701158 %J Journal of Cell Biology.

57. Gelens, L., Anderson, G.A., and James E. Ferrell, J. (2014). Spatial trigger waves: positive feedback gets you a long way. Mol Biol Cell *25*, 3486-3493. 10.1091/mbc.e14-08-1306.

58. Tanaka, E.M., and Reddien, P.W. (2011). The cellular basis for animal regeneration. Developmental cell *21*, 172-185. 10.1016/j.devcel.2011.06.016.

59. Vervoort, M. (2011). Regeneration and Development in Animals. Biological Theory *6*, 25-35. 10.1007/s13752-011-0005-3.

60. DuBuc, T.Q., Traylor-Knowles, N., and Martindale, M.Q. (2014). Initiating a regenerative response; cellular and molecular features of wound healing in the cnidarian Nematostella vectensis. BMC Biology *12*, 24. 10.1186/1741-7007-12-24.

61. Wan, J., Ramachandran, R., and Goldman, D. (2012). HB-EGF Is Necessary and Sufficient for Muller Glia Dedifferentiation and Retina Regeneration. Developmental Cell *22*, 334-347. 10.1016/j.devcel.2011.11.020.

62. Yun, Maximina H., Gates, Phillip B., and Brockes, Jeremy P. (2014). Sustained ERK Activation Underlies Reprogramming in Regeneration-Competent Salamander Cells and Distinguishes Them from Their Mammalian Counterparts. Stem Cell Reports *3*, 15-23. 10.1016/j.stemcr.2014.05.009.

63. Johnson, H.E., and Toettcher, J.E. (2019). Signaling Dynamics Control Cell Fate in the Early Drosophila Embryo. Developmental cell *48*, 361-370.e363. 10.1016/j.devcel.2019.01.009.

64. Handly, L.N., Pilko, A., and Wollman, R.J.E. (2015). Paracrine communication maximizes cellular response fidelity in wound signaling. eLife *4*, e09652.

65. Hino, N., Rossetti, L., Marín-Llauradó, A., Aoki, K., Trepat, X., Matsuda, M., and Hirashima, T. (2020). ERK-Mediated Mechanochemical Waves Direct Collective

Cell Polarization. Developmental Cell *53*, 646-660.e648. https://doi.org/10.1016/j.devcel.2020.05.011.

66. Hiratsuka, T., Fujita, Y., Naoki, H., Aoki, K., Kamioka, Y., and Matsuda, M. (2015). Intercellular propagation of extracellular signal-regulated kinase activation revealed by in vivo imaging of mouse skin. eLife *4*, e05178. 10.7554/eLife.05178.

67. Matsubayashi, Y., Ebisuya, M., Honjoh, S., and Nishida, E. (2004). ERK Activation Propagates in Epithelial Cell Sheets and Regulates Their Migration during Wound Healing. Current Biology *14*, 731-735. https://doi.org/10.1016/j.cub.2004.03.060.

68. Ishii, M., Tateya, T., Matsuda, M., and Hirashima, T. (2021). Retrograde ERK activation waves drive base-to-apex multicellular flow in murine cochlear duct morphogenesis. eLife *10*, e61092. 10.7554/eLife.61092.

69. Fenteany, G., Janmey, P.A., and Stossel, T.P. (2000). Signaling pathways and cell mechanics involved in wound closure by epithelial cell sheets. Current Biology *10*, 831-838. https://doi.org/10.1016/S0960-9822(00)00579-0.

70. Omelchenko, T., Vasiliev, J.M., Gelfand, I.M., Feder, H.H., and Bonder, E.M. (2003). Rho-dependent formation of epithelial "leader" cells during wound healing. PNAS *100*, 10788-10793. 10.1073/pnas.1834401100 %J Proceedings of the National Academy of Sciences.

71. Reffay, M., Parrini, M.C., Cochet-Escartin, O., Ladoux, B., Buguin, A., Coscoy, S., Amblard, F., Camonis, J., and Silberzan, P. (2014). Interplay of RhoA and mechanical forces in collective cell migration driven by leader cells. Nature Cell Biology *16*, 217-223. 10.1038/ncb2917.

72. Yamaguchi, N., Mizutani, T., Kawabata, K., and Haga, H. (2015). Leader cells regulate collective cell migration via Rac activation in the downstream signaling of integrin β1 and PI3K. Scientific Reports *5*, 7656. 10.1038/srep07656.

73. Boocock, D., Hino, N., Ruzickova, N., Hirashima, T., and Hannezo, E. (2020). Theory of mechanochemical patterning and optimal migration in cell monolayers. Nature Physics. 10.1038/s41567-020-01037-7.

74. Das, T., Safferling, K., Rausch, S., Grabe, N., Boehm, H., and Spatz, J.P. (2015). A molecular mechanotransduction pathway regulates collective migration of epithelial cells. Nature Cell Biology *17*, 276-287. 10.1038/ncb3115.

75. Tambe, D.T., Hardin, C.C., Angelini, T.E., Rajendran, K., Park, C.Y., Serra-Picamal, X., Zhou, E.H., Zaman, M.H., Butler, J.P., and Weitz, D.A.J.N.m. (2011). Collective cell guidance by cooperative intercellular forces. Nat Mater *10*, 469-475.

76. Grossman, C., Roos, H.-G., and Stynes, M. (2007). Numerical Treatment of Partial Differential Equations, 1 Edition (Springer-Verlag Berlin Heidelberg).

77. Fujioka, A., Terai, K., Itoh, R.E., Aoki, K., Nakamura, T., Kuroda, S., Nishida, E., and Matsuda, M. (2006). Dynamics of the Ras/ERK MAPK Cascade as Monitored by Fluorescent Probes. J Biol Chem *281*, 8917-8926. 10.1074/jbc.M509344200.

78. Bereiter-Hahn, J., and Zylberberg, L. (1993). Regeneration of teleost fish scale. Comparative Biochemistry and Physiology Part A: Physiology *105*, 625-641. https://doi.org/10.1016/0300-9629(93)90262-3.

79. Cox, B.D., De Simone, A., Tornini, V.A., Singh, S.P., Di Talia, S., and Poss, K.D. (2018). In Toto Imaging of Dynamic Osteoblast Behaviors in Regenerating Skeletal Bone. Curr Biol *28*, 3937-3947.e3934. 10.1016/j.cub.2018.10.052.

80. Iwasaki, M., Kuroda, J., Kawakami, K., and Wada, H. (2018). Epidermal regulation of bone morphogenesis through the development and regeneration of osteoblasts in the zebrafish scale. Developmental Biology *437*. 10.1016/j.ydbio.2018.03.005.

81. Regot, S., Hughey, J.J., Bajar, B.T., Carrasco, S., and Covert, M.W.J.C. (2014). High-sensitivity measurements of multiple kinase activities in live single cells. Cell *157*, 1724-1734.

82. Ogura, Y., Wen, F.-L., Sami, M.M., Shibata, T., and Hayashi, S. (2018). A Switch-like Activation Relay of EGFR-ERK Signaling Regulates a Wave of Cellular Contractility for Epithelial Invagination. Developmental Cell *46*, 162-172.e165. 10.1016/j.devcel.2018.06.004.

83. Aoki, K., Kondo, Y., Naoki, H., Hiratsuka, T., Itoh, R.E., and Matsuda, M.J.D.C. (2017). Propagating Wave of ERK Activation Orients Collective Cell Migration. *43*, 305-317. e305.

84. Deneke, Victoria E., Melbinger, A., Vergassola, M., and Di Talia, S. (2016). Waves of Cdk1 Activity in S Phase Synchronize the Cell Cycle in Drosophila Embryos. Developmental Cell *38*, 399-412. https://doi.org/10.1016/j.devcel.2016.07.023.

85. Vergassola, M., Deneke, V.E., and Di Talia, S. (2018). Mitotic waves in the early embryogenesis of *Drosophila*: Bistability traded for speed. PNAS *115*, E2165-E2174. 10.1073/pnas.1714873115 %J Proceedings of the National Academy of Sciences.

86. Roignant, J.-Y., and Treisman, J.E. (2009). Pattern formation in the Drosophila eye disc. Int J Dev Biol *53*, 795-804. 10.1387/ijdb.072483jr.

87. Lake, D., Corrêa, S.A.L., and Müller, J. (2016). Negative feedback regulation of the ERK1/2 MAPK pathway. Cell Mol Life Sci *73*, 4397-4413. 10.1007/s00018-016-2297-8.

88. Gerhart, J.C. (1980). Mechanisms Regulating Pattern Formation in the Amphibian Egg and Early Embryo. In Biological Regulation and Development, R. Goldberger, ed. (Plenum Press), pp. 133-316.

89. Zalokar, M., and Erk, I. (1976). Division and migration of nuclei during early embryogenesis of Drosophila melanogaster. J.Microsc.Biol.Cell. *25*, 97-106.

90. Yohn, C.B., Pusateri, L., Barbosa, V., and Lehmann, R. (2003). l (3) malignant brain tumor and three novel genes are required for Drosophila germ-cell formation. Genetics *165*, 1889-1900.

91. Hatanaka, K., and Okada, M. (1991). Retarded nuclear migration in Drosophila embryos with aberrant F-actin reorganization caused by maternal mutations and by cytochalasin treatment. Development *111*, 909-920. 10.1242/dev.111.4.909.

92. Sarikas, A., Hartmann, T., and Pan, Z.-Q. (2011). The cullin protein family. Genome Biology *12*, 220. 10.1186/gb-2011-12-4-220.

93. Alphey, L., Jimenez, J., White-Cooper, H., Dawson, I., Nurse, P., and Glover, D.M. (1992). twine, a cdc25 homolog that functions in the male and female germline of drosophila. Cell *69*, 977-988. 10.1016/0092-8674(92)90616-K.

94. Royou, A., Sullivan, W., and Karess, R. (2002). Cortical recruitment of nonmuscle myosin II in early syncytial Drosophila embryos: its role in nuclear axial expansion and its regulation by Cdc2 activity. The Journal of cell biology *158*, 127-137.

95. Munjal, A., Philippe, J.-M., Munro, E., and Lecuit, T. (2015). A self-organized biomechanical network drives shape changes during tissue morphogenesis. Nature *524*, 351-355.

96. Gavet, O., and Pines, J. (2010). Progressive Activation of CyclinB1-Cdk1 Coordinates Entry to Mitosis. Developmental Cell *18*, 533-543. https://doi.org/10.1016/j.devcel.2010.02.013.

97. Okumura, F., Joo-Okumura, A., Nakatsukasa, K., and Kamura, T. (2016). The role of cullin 5-containing ubiquitin ligases. Cell Division *11*, 1. 10.1186/s13008-016-0016-3.

98. Laszlo, G.S., and Cooper, J.A. (2009). Restriction of Src Activity by Cullin-5. Current Biology *19*, 157-162. 10.1016/j.cub.2008.12.007.

99. Pan, Q., Qiao, F., Gao, C., Norman, B., Optican, L., and Zelenka, P.S. (2011). Cdk5 targets active Src for ubiquitin-dependent degradation by phosphorylating Src(S75). Cellular and Molecular Life Sciences *68*, 3425. 10.1007/s00018-011-0638-1.

100. Teckchandani, A., Laszlo, G.S., Simó, S., Shah, K., Pilling, C., Strait, A.A., and Cooper, J.A. (2014). Cullin 5 destabilizes Cas to inhibit Src-dependent cell transformation. Journal of Cell Science *127*, 509-520. 10.1242/jcs.127829.

101. Hakak, Y., and Martin, G.S. (1999). Ubiquitin-dependent degradation of active Src. Current Biology *9*, S1-1042. 10.1016/S0960-9822(99)80453-9.

102. Harris, K.F., Shoji, I., Cooper, E.M., Kumar, S., Oda, H., and Howley, P.M. (1999). Ubiquitin-mediated degradation of active Src tyrosine kinase. Proceedings of the National Academy of Sciences *96*, 13738-13743.

103. Imamoto, A., and Soriano, P. (1993). Disruption of the csk gene, encoding a negative regulator of Src family tyrosine kinases, leads to neural tube defects and embryonic lethality in mice. Cell *73*, 1117-1124. 10.1016/0092-8674(93)90641-3.

104. Brown, M.T., and Cooper, J.A. (1996). Regulation, substrates and functions of src. Biochimica et biophysica acta *1287 2-3*, 121-149.

105. O'Reilly, A.M., Ballew, A.C., Miyazawa, B., Stocker, H., Hafen, E., and Simon, M.A. (2006). Csk differentially regulates Src64 during distinct morphological events in Drosophila germ cells. Development *133*, 2627-2638. 10.1242/dev.02423.

106. Boschek, C.B., Jockusch, B.M., Friis, R.R., Back, R., Grundmann, E., and Bauer, H. (1981). Early changes in the distribution and organization of microfilament proteins during cell transformation. Cell *24*, 175-184. 10.1016/0092-8674(81)90513-4.

107. Pedraza, L.G., Stewart, R.A., Li, D.-M., and Xu, T. (2004). Drosophila Src-family kinases function with Csk to regulate cell proliferation and apoptosis. Oncogene *23*, 4754-4762. 10.1038/sj.onc.1207635.

108. Idema, T., Dubuis, J.O., Kang, L., Manning, M.L., Nelson, P.C., Lubensky, T.C., and Liu, A.J. (2013). The Syncytial Drosophila Embryo as a Mechanically Excitable Medium. PLOS ONE *8*, e77216. 10.1371/journal.pone.0077216.

109. Edgar, B.A., Kiehle, C.P., and Schubiger, G. (1986). Cell cycle control by the nucleo-cytoplasmic ratio in early Drosophila development. Cell *44*, 365-372. https://doi.org/10.1016/0092-8674(86)90771-3.

110. Yasuda, G.K., Baker, J., and Schubiger, G. (1991). Temporal regulation of gene expression in the blastoderm Drosophila embryo. Genes & Development *5*, 1800-1812. 10.1101/gad.5.10.1800.

111. Strong, I.J.T., Lei, X., Chen, F., Yuan, K., and O'Farrell, P.H. (2020). Interphase-arrested Drosophila embryos activate zygotic gene expression and initiate mid-blastula transition events at a low nuclear-cytoplasmic ratio. PLOS Biology *18*, e3000891. 10.1371/journal.pbio.3000891.

112. Chang, J.B., and Ferrell Jr, J.E. (2013). Mitotic trigger waves and the spatial coordination of the Xenopus cell cycle. Nature *500*, 603-607.

113. Novak, B., and Tyson, J.J. (1993). Modeling the cell division cycle: M-phase trigger, oscillations, and size control. Journal of theoretical biology *165*, 101-134.

114. Fogarty, P., Campbell, S.D., Abu-Shumays, R., Phalle, B.d.S., Yu, K.R., Uy, G.L., Goldberg, M.L., and Sullivan, W. (1997). The Drosophila grapes gene is related to checkpoint gene chk1/rad27 and is required for late syncytial division fidelity. Current Biology *7*, 418-426. https://doi.org/10.1016/S0960-9822(06)00189-8.

115. Shimuta, K., Nakajo, N., Uto, K., Hayano, Y., Okazaki, K., and Sagata, N. (2002). Chk1 is activated transiently and targets Cdc25A for degradation at the Xenopus midblastula transition. The EMBO journal *21*, 3694-3703.

116. Sibon, O.C.M., Stevenson, V.A., and Theurkauf, W.E. (1997). DNA-replication checkpoint control at the Drosophila midblastula transition. Nature *388*, 93-97. 10.1038/40439.

117. Brouns, M.R., Matheson, S.F., and Settleman, J. (2001). p190 RhoGAP is the principal Src substrate in brain and regulates axon outgrowth, guidance and fasciculation. Nature Cell Biology *3*, 361-367. 10.1038/35070042.

118. DerMardirossian, C., Rocklin, G., Seo, J.-Y., and Bokoch, G.M. (2006). Phosphorylation of RhoGDI by Src regulates Rho GTPase binding and cytosol-membrane cycling. Molecular biology of the cell *17*, 4760-4768. 10.1091/mbc.e06-06-0533.

119. Nagao, M., Kaziro, Y., and Itoh, H. (1999). The Src family tyrosine kinase is involved in Rho-dependent activation of c-Jun N-terminal kinase by Gα12. Oncogene *18*, 4425-4434. 10.1038/sj.onc.1202832.

120. Masui, Y., and Wang, P. (1998). Cell cycle transition in early embryonic development of Xenopus laevis. Biology of the Cell *90*, 537-548. https://doi.org/10.1111/j.1768-322X.1998.tb01062.x.

121. Chan, S.H., Tang, Y., Miao, L., Darwich-Codore, H., Vejnar, C.E., Beaudoin, J.-D., Musaev, D., Fernandez, J.P., Benitez, M.D.J., Bazzini, A.A., et al. (2019). Brd4 and P300 Confer Transcriptional Competency during Zygotic Genome Activation. Developmental Cell *49*, 867-881.e868. 10.1016/j.devcel.2019.05.037.

122. Gert, K.R., Quio, L.E.C., Novatchkova, M., Guo, Y., Cairns, B.R., and Pauli, A. (2021). Reciprocal zebrafish-medaka hybrids reveal maternal control of zygotic genome activation timing. bioRxiv, 2021.2011.2003.467109. 10.1101/2021.11.03.467109.

123. Lee, M.T., Bonneau, A.R., Takacs, C.M., Bazzini, A.A., DiVito, K.R., Fleming, E.S., and Giraldez, A.J. (2013). Nanog, Pou5f1 and SoxB1 activate zygotic gene expression during the maternal-to-zygotic transition. Nature *503*, 360-364. 10.1038/nature12632.

124. Pálfy, M., Joseph, S.R., and Vastenhouw, N.L. (2017). The timing of zygotic genome activation. Current Opinion in Genetics & Development *43*, 53-60. https://doi.org/10.1016/j.gde.2016.12.001.

125. Jevtić, P., and Levy, D.L. (2015). Nuclear size scaling during Xenopus early development contributes to midblastula transition timing. Curr Biol *25*, 45-52. 10.1016/j.cub.2014.10.051.

126. Jevtić, P., and Levy, D.L. (2017). Both Nuclear Size and DNA Amount Contribute to Midblastula Transition Timing in Xenopus laevis. Scientific Reports *7*, 7908. 10.1038/s41598-017-08243-z.

127. Jukam, D., Kapoor, R.R., Straight, A.F., and Skotheim, J.M. (2021). The DNA-to-cytoplasm ratio broadly activates zygotic gene expression in Xenopus. Current Biology *31*, 4269-4281.e4268. 10.1016/j.cub.2021.07.035.

128. Pritchard, D.K., and Schubiger, G. (1996). Activation of transcription in Drosophila embryos is a gradual process mediated by the nucleocytoplasmic ratio. Genes & Development *10*, 1131-1142. 10.1101/gad.10.9.1131.

129. Syed, S., Wilky, H., Raimundo, J., Lim, B., and Amodeo, A.A. (2021). The nuclear to cytoplasmic ratio directly regulates zygotic transcription in Drosophila through multiple modalities. Proc Natl Acad Sci U S A *118*, e2010210118. 10.1073/pnas.2010210118.

130. Blythe, Shelby A., and Wieschaus, Eric F. (2015). Zygotic Genome Activation Triggers the DNA Replication Checkpoint at the Midblastula Transition. Cell *160*, 1169-1181. https://doi.org/10.1016/j.cell.2015.01.050.

131. Djabrayan, N.J.V., Smits, C.M., Krajnc, M., Stern, T., Yamada, S., Lemon, W.C., Keller, P.J., Rushlow, C.A., and Shvartsman, S.Y. (2019). Metabolic Regulation of Developmental Cell Cycles and Zygotic Transcription. Current Biology *29*, 1193-1198.e1195. https://doi.org/10.1016/j.cub.2019.02.028.

132. Liu, B., Winkler, F., Herde, M., Witte, C.-P., and Großhans, J. (2019). A link between deoxyribonucleotide metabolites and embryonic cell-cycle control. Current Biology *29*, 1187-1192. e1183.

133. Shindo, Y., and Amodeo, A.A. (2021). Excess histone H3 is a competitive Chk1 inhibitor that controls cell-cycle remodeling in the early Drosophila embryo. Current Biology *31*, 2633-2642.e2636. 10.1016/j.cub.2021.03.035.

134. Blankenship, J.T., and Wieschaus, E. (2001). Two new roles for the Drosophila AP patterning system in early morphogenesis. Development *128*, 5129-5138. 10.1242/dev.128.24.5129.

135. Gilbert, S.F. (2000). Developmental biology (Sinauer Associates).

136. Dernburg, A.F., Daily, D.R., Yook, K.J., Corbin, J.A., Sedat, J.W., and Sullivan, W. (1996). Selective loss of sperm bearing a compound chromosome in the Drosophila female. Genetics *143*, 1629-1642. 10.1093/genetics/143.4.1629.

137. Di Talia, S., She, R., Blythe, Shelby A., Lu, X., Zhang, Qi F., and Wieschaus, Eric F. (2013). Posttranslational Control of Cdc25 Degradation Terminates Drosophila's Early Cell-Cycle Program. Current Biology *23*, 127-132. https://doi.org/10.1016/j.cub.2012.11.029.

138. Hubaud, A., Regev, I., Mahadevan, L., and Pourquié, O. (2017). Excitable Dynamics and Yap-Dependent Mechanical Cues Drive the Segmentation Clock. Cell *171*, 668-682.e611. https://doi.org/10.1016/j.cell.2017.08.043.

139. Anderson, G.A., Gelens, L., Baker, J.C., and Ferrell, J.E., Jr. (2017). Desynchronizing Embryonic Cell Division Waves Reveals the Robustness of Xenopus laevis Development. Cell reports *21*, 37-46. 10.1016/j.celrep.2017.09.017.

Biography

Luke Hayden attended Indiana Wesleyan University where he majored in biochemistry, mathematics, and honors humanities. During summer internships, he contributed to a publication describing the competence circuit of *Bascillus subtilis* and a publication on potyviral interactions with host factors in cassava. In 2017, he graduated and began attending Duke University in the Computational Biology and Bioinformatics program, joining the lab of Stefano Di Talia in 2018. During his graduate studies he begin investigating how chemical waves coordinate cellular signals in zebrafish scales and *Drosophila* embryos. In doing so he contributed to a publication on the discovery of Erk activity waves in zebrafish scale regeneration and authored a follow-up paper entitled "Mathematical modeling of Erk activity waves in regenerating zebrafish scales." He then published a paper entitled "Cullin-5 mutants reveal collective sensing of the nucleocytoplasmic ratio in Drosophila embryogenesis."